

LOCAL MODELING OF THE IONOSPHERIC VERTICAL TOTAL ELECTRON CONTENT
(VTEC) USING
PARTICLE FILTER

A THESIS SUBMITTED TO
THE GRADUATE SCHOOL OF NATURAL AND APPLIED SCIENCES
OF
MIDDLE EAST TECHNICAL UNIVERSITY

BY

ARMIN AGHAKARIMI

IN PARTIAL FULFILLMENT OF THE REQUIREMENTS
FOR
THE DEGREE OF MASTER OF SCIENCE
IN
GEODETIC AND GEOGRAPHIC INFORMATION TECHNOLOGIES

SEPTEMBER 2012

Approval of the thesis:

**LOCAL MODELING OF THE IONOSPHERIC VERTICAL TOTAL ELECTRON CONTENT
(VTEC) USING
PARTICLE FILTER**

submitted by **ARMIN AGHAKARIMI** in partial fulfillment of the requirements for the degree of **Master of Science in Geodetic and Geographic Information Technologies Department, Middle East Technical University** by,

Prof. Dr. Canan Özgen _____
Dean, **Graduate School of Natural and Applied Sciences**

Assoc.Prof.Dr. Ahmet Çoşar _____
Head of Department, **Geodetic and Geographic Information Technologies**

Prof. Dr. Mahmut Onur Karslıoğlu _____
Supervisor, **Civil Engineering Department**

Examining Committee Members:

Prof. Dr. Gülbin Dural _____
Electrical and Electronics Engineering Department, METU

Prof. Dr. Mahmut Onur Karslıoğlu _____
Civil Engineering Department, METU

Assoc. Prof. Dr. Zuhale Akyürek _____
Civil Engineering Department, METU

Assoc.Prof.Dr. Utku Kanoğlu _____
Engineering Sciences Department, METU

Assoc.Prof.Dr. Ali Kılıçoğlu _____
General Command of Mapping - Retired

Date: 21/09/2012

I hereby declare that all information in this document has been obtained and presented in accordance with academic rules and ethical conduct. I also declare that, as required by these rules and conduct, I have fully cited and referenced all material and results that are not original to this work.

Name, Last name : ARMIN AGHAKARIMI

Signature :

ABSTRACT

LOCAL MODELING OF THE IONOSPHERIC VERTICAL TOTAL ELECTRON CONTENT (VTEC) USING PARTICLE FILTER

Aghakarimi, Armin

M.Sc., Department of Geodetic and Geographic Information Technologies

Supervisor: Prof. Dr. Mahmut Onur Karslıoğlu

September 2012, 98 pages

Ionosphere modeling is an important field of current studies because of its influences on the propagation of the electromagnetic signals. Among the various methods of obtaining ionospheric information, Global Positioning System (GPS) is the most prominent one because of extensive stations distributed all over the world. There are several studies in the literature related to the modeling of the ionosphere in terms of Total Electron Content (TEC). However, most of these studies investigate the ionosphere in the global and regional scales. On the other hand, complex dynamic of the ionosphere requires further studies in the local structure of the TEC distribution. In this work, Particle filter has been used for the investigation of local character of the ionosphere VTEC. Besides, standard Kalman filter as an effective method for optimal state estimation is applied to the same data sets to compare the corresponding results with results of Particle filter. The comparison shows that Particle filter indicates better performance than the standard Kalman filter especially

during the geomagnetic storm. MATLAB[®] R2011 software has been used for programming all processes and algorithms of the study.

Keywords: Ionosphere Modeling, GPS, Particle filter, Kalman Filter

ÖZ

İYONOSFERİK DİKTOPLAM ELEKTRON İÇERİĞİNİN (VTEC) PARTİKL FİLTRE KULLANARAK YEREL MODELLENMESİ

Aghakarimi, Armin

Yüksek Lisans, Jeodezi ve Coğrafi Bilgi Teknolojileri Bölümü

Tez Yöneticisi : Prof. Dr. Mahmut Onur Karslıoğlu

Eylül 2012, 98 Sayfa

İyonosfer modellemesi, elektromanyetik sinyalin yayılımına yaptığı etki nedeniyle günümüzdeki önemli çalışma alanlarından bir tanesidir. İyonosfere yönelik bilgilerin edinilmesiyle ilgili yöntemler arasında Global Konumlama Sistemi (GPS) önemli bir yer tutmaktadır. GPS istasyonlarının tüm yeryüzünde dağılmış olması bu durumu güçlendirmektedir. İyonosferik Toplam Elektron İçeriği (TEC) konusunda literatürde çeşitli çalışmalar mevcuttur. Ancak, bu çalışmalar global ve bölgesel ölçeklerdeki İyonosfer modellemesini içermektedir. Öte yandan, İyonosferin değişken dinamiği, TEC dağılımının yapısının araştırılabilmesi için daha fazla çalışmalara gereksinim duyulduğunu ortaya koymuştur. Bu çalışmada ise, VTEC dağılımının yerel karakterinin belirlenmesi için Partikel (Parçacık) filtresi kullanılmıştır. Ayrıca, optimal durum kestiriminde etkin bir metod olan standard Kalman filtresi, özellikle jeomanyetik aktivite döneminde, Parçacık filtresi sonuçlarına karşılaştırmak için aynı veri setine uygulanmıştır. Karşılaştırma sonucunda, Parçacık filtresi Kalman filtresinden daha iyi

bir performans sergilemiştir. Tüm işlem ve algoritmaların programlanmasında MATLAB[®] R2011 yazılımı kullanılmıştır.

Anahtar Kelimeler: iyonosfer modelleme, GPS, Parçacık filtresi, Kalman Filtresi

To my family

ACKNOWLEDGMENTS

I am deeply grateful to Prof. Dr. Mahmut Onur Karslıođlu for his supervision, wisdom advices, great guidance and encouragement not only during this work but also in the whole period of my graduate study.

I also thank to examining committee members Assoc. Prof. Dr. Zuhall Akyürek, Prof. Dr. Gülbin Dural, Assoc. Prof. Dr. Ali Kılıçođlu and Assoc. Prof. Dr. Utku Kanođlu for their valuable comments and contributions.

I would like to convey my deepest thanks to my family whom I dedicated this work for their support and encouragement.

I am also grateful to my friends and colleagues in METU for their suggestions and contributions.

TABLE OF CONTENTS

ABSTRACT	iv
ÖZ.....	vi
ACKNOWLEDGMENTS	ix
TABLE OF CONTENTS	x
LIST OF TABLES	xiii
TABLES	xiii
LIST OF FIGURES	xiv
1. Introduction.....	1
1.1 Background	1
1.2 Motivation and Objectives.....	4
1.3 Thesis Outline	5
2. Ionosphere and the Global Positioning System	6
2.1 Ionosphere.....	6
2.1.1 Ionosphere index of refraction.....	9
2.2 The Global Positioning System	13
2.2.1 GPS Observables.....	14
2.2.2 GPS observables Error Sources.....	17
2.3 Ionospheric Impacts on GPS signal.....	21

2.4 Extracting Ionosphere Information from GPS observations	23
2.4.1 The Geometry-Free linear combination of GPS observations	23
2.4.2 Adjustment of the GPS observations	24
2.4.3 Differential Code Biases	26
2.4.4 Cycle Slip Detection	27
2.4.5 Single Layer Model of Ionosphere.....	28
3. Optimal State Estimation; Kalman Filtering and Particle Filtering.....	32
3.1 Recursive Parameter Estimation	34
3.2 Recursive Bayesian Estimation	35
3.3 Kalman Filter.....	37
3.4 Particle Filter.....	41
3.4.1 Sequential Importance Sampling	42
3.4.2 Resampling	45
3.4.3 Generic Particle Filter	47
3.4.3 Regularized Particle Filter.....	48
4. Implementation and Application.....	55
4.1 Data Set	55
4.2 Preprocessing	56
4.3 Ionosphere Modeling	58
4.3.1 Filters Application.....	59
4.4 Results and Evaluations.....	60
5. Conclusion and Future Work.....	91

5.1 Conclusion	91
5.2 Future Work.....	92
REFERENCES.....	94

LIST OF TABLES

TABLES

Table 1 the wavelengths of GPS signals and noise codes	14
Table 2 GPS receiver types based on the type of provided code measurements	26
Table 3 the Kalman filter algorithm.....	40
Table 4 the resampling algorithm	47
Table 5 Generic Particle filter	49
Table 6 Regularized Particle filter.....	54
Table 7 Stations	55
Table 8 RMSE of the results in each station	61

LIST OF FIGURES

FIGURES

Figure 1 the ionization process.....	7
Figure 2 the vertical electron density profile of the ionosphere	8
Figure 3 multipath and direct signals	20
Figure 4 the electron density irregularities in the ionosphere	22
Figure 5 the single layer model for ionosphere	29
Figure 6 Spherical triangle formed by receiver, North Pole and IPP.....	30
Figure 7 Sampling difference between Kalman filter (a) and Particle filter (b)	42
Figure 8 resampling step	46
Figure 9 Schematic illustration of generic Particle filter	48
Figure 10 Stations used in this study are the blue ones.....	56
Figure 11 the preprocessing steps.....	57
Figure 12 axpv station results.....	62
Figure 13 badh station results.....	63
Figure 14 bpdI station results	64
Figure 15 bute station results.....	65
Figure 16 bydg station results.	66
Figure 17 clib station results.....	67
Figure 18 cpar station results.	68
Figure 19 crak station results.	69
Figure 20 crei station results	70
Figure 21 ctab station results	71
Figure 22 delf station results.....	72
Figure 23 dent station results.....	73
Figure 24 eijs station results.....	74

Figure 25 eusk station results.....	75
Figure 26 gwwl station results.....	76
Figure 27 hobu station results.....	77
Figure 28 hoe2 station results.....	78
Figure 29 igeo station results	79
Figure 30 lodz station results	80
Figure 31 man2 station results.....	81
Figure 32 mlvl station results	82
Figure 33 redz station results.....	83
Figure 34 smne station results	84
Figure 35 swki station results.....	85
Figure 36 ters station results.....	86
Figure 37 tlmf station results.....	87
Figure 38 vfch station results	88
Figure 39 ware station results.....	89
Figure 40 zywi station results.....	90

CHAPTER 1

Introduction

1.1 Background

The ionosphere is a region in the upper atmosphere where existence of the free electrons influences propagation of the radio waves (Langery, 2000; Pulinets & Boyarchuk, 2004). Many scientific disciplines concern with the ionosphere because of its effect on propagated electromagnetic waves from the satellites to the ground based receivers (Liu & Gao, 2004).

Single frequency altimetry observations are affected by path delay due to the ionosphere. The path delay error must be removed for the accurate sea surface height computation. Magnitude of the path delay reaches 20 cm during solar maximum or solar storm the (Komjathy, B., & Bilitza, 1998). The ionosphere also causes perturbations in the propagation path of the signals in the Synthetic Aperture Radar (SAR) receivers which result in phase changes distorting the SAR images (Liu & Kuga, 2003). The ionosphere is a prominent error source for the Global Navigation Satellite Systems (GNSS) such as Global Positioning Systems (GPS). After Selective Availability turned off on May 2000 the ionosphere is the most significant error source for the GPS signals (Kunches & Klobuchar, 2001). The ionosphere imposes phase advance and pseudorange group delay for the GPS signals that lead to

inaccuracies in calculated positions. In the dual frequency GPS receivers, the ionospheric effect can be removed from the signal by making use of the dispersive characteristic of the ionosphere. In single frequency receivers, however, there should be a model for compensating this error source (Komjathy A. , 1997).

Because of reasons mentioned, the ionosphere modeling became an important research area in the field of Earth and atmospheric sciences from 1970s. Since that time many theoretical, semi-empirical or empirical models have been introduced. Ionospheric Bent, Parameterized Ionospheric model (PIM) and International Reference Ionosphere (IRI) are just few examples of these models (Nohutcu, 2009). Most of these models are in global scale and provide ionospheric information in various temporal and spatial epochs. They use monthly or daily averages of input data for modeling. These models are suitable for geomagnetically quiet conditions. However, the nature of ionosphere is highly dynamic particularly when geomagnetic storms happen (Doherty, et al 1999; Langery,2000).

The ionosphere modeling can be investigated in 3 main categories; global, regional and local modeling. Here, some of the models for these categories have been described briefly.

- Global modeling

The Center for Orbit Determination in Europe (CODE) (one of the Analysis Centers of the International GPS Service for Geodynamics (IGS)) produces Global Ionosphere Maps (GIM) since 1996. It is the most stable and continuous Vertical Total Electron Content (VTEC) model and provides global maps with a resolution of 2 hour, 5°, and 2.5° respectively in time, longitude and latitude (Hernández-Pajares, et al., 2009). The mathematical model used for generating maps is spherical harmonic expansions up to degree 8 in a single layer with respect to

sun-fixed frame. Everyday a set of TEC coefficients are calculated for representing the average distribution of VTEC in a global scale (Schaer, Beutler, & Rothacher,1996).

IRI is a joint project of URSI¹ and COSPAR². It uses an empirical model for determination of ionospheric parameters such as electron density, electron temperature, and ion composition. It uses wide range of ground and space data for calculation of monthly averages of these parameters (Bilitza, 2001).

- Regional modeling

B-Spline modeling of the Vertical Total Electron Content (VTEC) that uses GPS ground based stations is an example of regional ionosphere modeling. It is presented in both 2D, sun-fixed reference frame, and 3D, Earth-fixed reference frame in arbitrary time intervals. Based on the localizing property of B-Spline model, it offers a better spatial resolution than global models (Nohutcu, Karslioglu, & Schmidt,2010).

B-MARS Modeling of VTEC is another example of this category. Multivariate Adaptive Regression B-Splines (B-MARS) Model is used for modeling the VTEC information of GPS stations through a region. It gives more acceptable results in the cases of geomagnetic storms than the traditional spherical harmonics (Karslioglu & Durmaz, 2012).

- Local modeling

WinTec is a Kalman filter-based algorithm for monitoring and modeling near real time ionosphere data derived from dual frequency GPS observations. Although it

¹ International Union for Radio Science

² Committee on Space Research

can be used for several GPS stations for estimating TEC and works as a regional model, it is more appropriate for station based tasks. The dynamic model within the Kalman filter is based on random walk process (Anghel, Astilean, Letia, & Komjathy, 2008).

Regularized estimation of TEC from GPS is another approach for local modeling of ionosphere. In this method a two steps regularization algorithm is applied to the GPS signals from various satellites and gives smoother VTEC values for any given station in any given time (Arikan, Arikan, & Erol, 2007).

1.2 Motivation and Objectives

As mentioned in the previous section, ionosphere modeling is one of the important concerns of the scientists and researchers in the field of geoscience and atmospheric science. GPS observations are valuable sources for constructing ionospheric models. Many sophisticated models have been developed in global, regional and local scale based on the GPS data. According to the high dynamic nature of the ionosphere especially during geomagnetic storm, more investigations on the modeling of the ionospheric VTEC signal must be taken on. Particle filter can be an appropriate algorithm for modeling and monitoring the VTEC signal especially in unusual conditions, e.g. during geomagnetic storm.

Particle filter is an effective algorithm for estimation of nonlinear and non-Gaussian systems. It is based on Sequential Monte Carlo method and filters the state variables by recursively creating sets of weighted samples (Ristic, Arulampalam, & Gordon,

2004). Implementation of Particle filter for VTEC modeling and comparison of its results with standard Kalman filter is the main objective of this study.

1.3 Thesis Outline

Thesis background and objectives has been illustrated in the previous sections of this chapter. Essential theoretical and fundamental information will be provided through the chapter 2 and the chapter 3. In the chapter 2, at first the ionosphere and the GPS will be briefly explained. Then, the effect of ionosphere on the GPS signal and extraction of TEC form GPS signal will be demonstrated. In Chapter 3 the recursive Bayesian estimation as a prerequisite for Kalman and Particle filters will be illustrated in summary. In this chapter, also, the algorithms of the mentioned filters will be represented. Application process of the filters over data and their results will be investigated in chapter 4. In the last chapter the conclusion and the potential future works will be described.

CHAPTER 2

Ionosphere and the Global Positioning System

2.1 Ionosphere

Ionosphere is the upper section of atmosphere that starts from the height of approximately 50 km to 1000 km. The Earth magnetic field has a significant effect on the formation of the ionosphere. Ionized gases are the main component of the ionosphere. The X and ultraviolet radiations excites the molecules especially Oxygen in this region and this interaction ends up in the production of free electrons and ions (Figure 1). Density of the electrons is highly related to the solar radiation. Many factors (e.g. time, location, height and etc.) are important in the intensity of the solar radiation and this makes the ionosphere extremely complex. During the daytime, strong solar radiations cause increment in the amount of free electrons. Electron density summits at about 2 p.m. of local time. Also seasonal effects can be detected in the density of electrons because of the revolution of the Earth around the sun and variation in solar radiation angel (Pulinets & Boyarchuk, 2004; Kasha, 1969).

From the spatial point of view, the ionosphere variations highly depend on geographic latitude. The Earth can be separated into 3 geographical regions that have completely different characteristics in the ionospheric variation; equatorial latitude region, mid-latitude region and high-latitude region. Equatorial latitude

region is the interval between -30° and $+30^\circ$ in geomagnetic latitude. The highest electron contents and large gradients occur in this region. Mid-latitude region is the region from $\pm 30^\circ$ to $\pm 60^\circ$ of the geomagnetic latitude. Ionosphere has the most regular behavior in mid-latitude region though during the ionospheric storm, there can be some variations up to 20% in the total electron content of this region. The high-latitude region has the most complex ionosphere structure because of the dominant geomagnetic field in this region (Brunini, Meza, Azpilicueta, Van Zele, Gende, & Diaz, 2004).



Figure 1 the ionization process

Above mentioned factors are mostly the known ones that influences the ionosphere where as there are many other parameters that cause irregularities in the ionosphere. One of these irregularities is the ionospheric storm that coincides with significant disturbances in the magnetic field of the Earth and strong solar eruption. The ionospheric storms may take several hours or several days and can occur in a region or globally. Traveling Ionosphere Disturbance (TID) is another irregularity that is not completely known. However, it can be related to the perturbations of the neutral atmosphere. Irregularities in the ionosphere can lead to the scintillation especially in the polar and the equatorial regions and this causes sudden changes in TEC concentrations (Gwal & Jain, 2011; Garcia Fenrnandez, 2004).

Generally vertical structure of the ionosphere is separated into four layers. First layer is layer D which is in the altitude of 50 to 90 km from the earth surface. This layer mainly generated by X and Lyman α rays of the solar radiation and disappears at night because of recombination of ions and electrons. It absorbs signals with frequency lower than 7MHz. Layer E expands from the altitude of 90 km up to 150 km and is produced by soft X rays. This layer has complicated structure in high latitudes.

The F1 region is between the altitudes of 150 km and 210 km. it, also, disappears at night time like D layer. From the altitude of 210 km to 1000 km is the F2 layer. F1 and F2 layers are generated by the ultra violet solar radiation. F2 region has the highest electron density. The maximum electron density in this layer is formed between the altitude of 250 km and 400 km (Langery, 2000) (Figure 2).

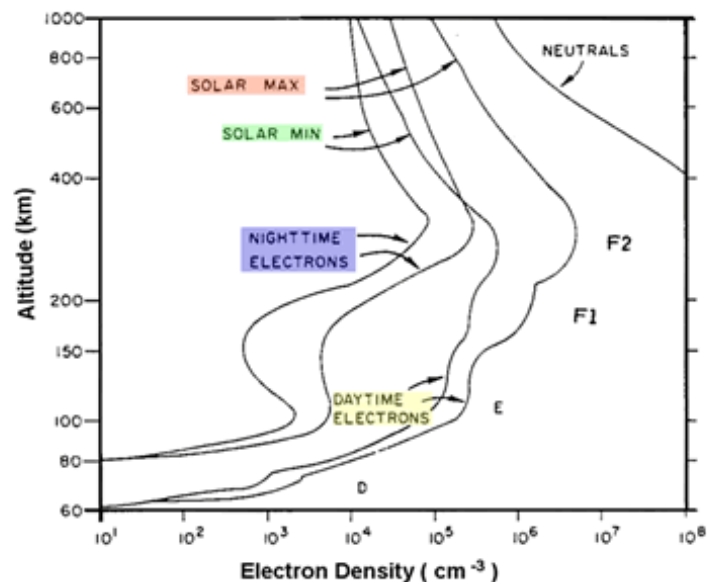


Figure 2 the vertical electron density profile of the ionosphere

2.1.1 Ionospheric index of refraction

During the transmission of electromagnetic wave through the ionosphere, its path and speed are changed. The speed of electromagnetic signal in the vacuum is equal to the speed of light. While it passes through another medium the character of the signal forms by the refractive index of that medium. Index of refraction in a medium, n , can be expressed by:

$$n = \frac{c}{v} \quad (2.1)$$

where

c : Speed of the light

v : Velocity of the wave in the medium

On the basis of the dispersive property of the ionosphere, the propagation velocities of the signals in the ionosphere are related to their frequency. The refraction index of the ionosphere for a signal depends on the location. It has been formulated by Appleton and Hartree (Rishbeth & Garriot, 1969) as follow

$$n^2 = \frac{X}{1 - iZ - \frac{Y_T^2}{2(1 - X - iZ)} \pm \left[\frac{Y_T^4}{4(1 - X - iZ)^2} + Y_L^2 \right]^{1/2}} \quad (2.2)$$

where

$$X = N_e e^2 / \epsilon_0 m \omega^2 = f_n^2 / f^2,$$

$$Y_L = eB_L / m\omega = f_H \cos \theta / f,$$

$$Y_T = eB_T / m\omega = f_H \sin \theta / f,$$

$$Z = \nu / \omega,$$

$$\omega = 2\pi f,$$

with

f = the radio-wave frequency,

f_H = the electron gyro frequency,

f_n = the electron plasma frequency,

N = Electron density (el/m³),

e = electron charge = -1.602×10^{-19} Coulomb,

ϵ_0 = permittivity of free space = 8.854×10^{-12} Farads/m,

θ = the angle between the wave direction and the Earth's magnetic field,

m = the mass of a electron = 9.107×10^{-31} kg,

ν = the electron neutral collision frequency, and

B = ambient magnetic field.

An accuracy of better than 1% can be reached by simplifying the equation 2.2 and ignoring higher order terms. So, by putting the values of the constants (e.g. e , m , and ϵ_0) and approximating it to the first order, the refractive index for carrier phase of signal is expressed as follow

$$n_p = 1 - 40.3 \frac{N_e}{f^2}. \quad (2.3)$$

The refractive index for code propagation (phase delay) is similar to the carrier phase but with the positive sign instead of negative in equation 2.3 which is given by

$$n_g = 1 + 40.3 \frac{N_e}{f^2}. \quad (2.4)$$

For extracting the range error the strategy defined below can be followed(Langery, 2000). The range, S , between transmitter and receiver can be measured by integrating the refractive index through the signal path

$$S = \int_{Tr}^{Rc} n.ds. \quad (2.5)$$

The geometrical range, S_0 , can be defined similar to the equation 2.5 by substituting n by 1

$$S_0 = \int_{Tr}^{Rc} ds_0. \quad (2.6)$$

The Ionospheric refraction (ΔS^{ION}) defined by the path length difference between measured and geometric range, can be obtained by

$$\Delta S^{ION} = S - S_0 = \int_{Tr}^{Rc} n.ds - \int_{Tr}^{Rc} ds_0. \quad (2.7)$$

By replacing refractive index as in the equation 2.3, the phase delay (ΔS_p^{ION}) can be given as

$$\Delta S_p^{ION} = \int_{Tr}^{Rc} \left(1 - 40.3 \frac{N_e}{f^2}\right) ds - \int_{Tr}^{Rc} ds_0, \quad (2.8)$$

Similarly by replacing refractive index as in equation 2.4, the group delay can be given by

$$\Delta S_g^{ION} = \int_{Tr}^{Rc} (1 + 40.3 \frac{N_e}{f^2}) ds - \int_{Tr}^{Rc} ds_0. \quad (2.9)$$

Based on the small amount of delay, it can be assumed $ds = ds_0$. Then the equations 2.8 and 2.9 simplified as

$$\Delta S_p^{ION} = \frac{-40.3}{f^2} \int_{Tr}^{Rc} N_e ds_0, \quad (2.10)$$

and

$$\Delta S_g^{ION} = \frac{40.3}{f^2} \int_{Tr}^{Rc} N_e ds_0. \quad (2.11)$$

Total Electron Content (TEC) is defined as the integration of electrons through the signal path

$$TEC = \int_{Tr}^{Rc} N_e ds_0. \quad (2.12)$$

Therefore,

$$\begin{aligned} \Delta S_p^{ION} &= -I = \frac{-40.3}{f^2} TEC, \\ \Delta S_g^{ION} &= I = \frac{40.3}{f^2} TEC, \end{aligned} \quad (2.13)$$

the unit of measured TEC is 10^{16} electrons per m^2 .

2.2 The Global Positioning System

NAVSTAR³ GPS is a satellite based navigation and positioning system that started to develop from 1973 in United State of America mainly for military purposes. It attained the fully operational capability in 1994 and started to give two navigation services, the Standard Positioning Service (SPS) and Precise Positioning Service (PPS). The first one is for civil services and the second one is for military purposes. During 1990s, the accuracy of SPS has been decreased intentionally with a technique called Selective Availability (SA) (Groves, 2008). SA turned off on May 2000.

GPS has three segments; space, control and user. In space segment, GPS is constellation of nominally 24 and maximum 36 satellites. Although all operational satellites provide full service, few new satellites stay on standby mode in order to bring to the operation in the case of failure of any old one. These satellites arranged in six orbital planes. Each of orbital planes has inclination of 55° with respect to the equator and separated by about 60° in longitude. The heights of orbits are about 20200 km above the Earth surface and have the periods of 11 hours and 58 minutes. Each orbit has at least 4 satellites (Groves, 2008).

GPS provides 10 navigation signals propagated through three bands; L1, L2 and L5. Up to now L5 is just open for PPS. The carrier frequency for L1 and L2 are 1575.42 MHz and 1227.60 MHz respectively. The L1 signal is modulated by 2 pseudorandom noise codes; Coarse/Acquisition code (C/A code) and Precise code (P-code) with chipping rate of 1.023 MHz and 10.23 MHz, respectively. However, L2 signal is modulated by just P-code. The corresponding wave length of the signals and noise codes can be found in Table 1.

³ NAVigation Satellite Timing And Ranging

Table 1 the wavelengths of GPS signals and noise codes

	L1	L2	C/A code	P-code
wavelength	19 cm	24.4 cm	300 m	30 m

Additionally the navigation message that includes information about the satellite orbit, satellite clock, ionospheric corrections and satellite performance status is send to the receivers by the modulating signals (Mohinder, Lawrence, & Angus, 2007).

The control segment of GPS, which consists of master control station, monitoring stations and ground antennas, is responsible for monitoring and controlling the satellites. This segment has to provide information about the orbits and the clocks of the satellites. The provided information is uploaded to the satellites periodically. The antennas and receivers comprise the user segment and are used for acquisition of the GPS transmitter signals (Hofmann-Wellenhof, Lichtenegger, & Wasle, 2008).

2.2.1 GPS Observables

Pseudorange P , carrier phase Φ , and the Doppler are the observables of GPS. Doppler is the difference between the nominal and received frequency due to the Doppler Effect over the GPS signal. As the Doppler is not essential for the ionospheric applications of GPS signals in this study, it will not be described in the rest of the text. Since 1989, a common data format has been introduced for GPS observations because of the various internal formats of receivers. This format is Receiver Independent Exchange Format (RINEX).

Pseudorange is the range measured from satellite to receiver calculated by the C/A and P-codes. For pseudorange determination the code generated by the satellite is replicated in the receiver. Then the elapsed time for the signal propagation is computed by correlating the original code and the replica. Next, the pseudorange

can be easily calculated by multiplying the computed time span by the speed of light. The measured range called pseudorange because of disagreement in the clocks of transmitter and receiver (Mohinder, Lawrence, & Angus, 2007). In addition to clock bias, there are some other errors in the pseudorange that is briefly investigated below. The observation equation of the pseudorange is expressed as follow

$$P1 = \rho + c(dt - dT) + c(\tau_{P1}^S + \tau_{P1}^R) + I_1 + d_{trop} + \varepsilon_{P1}, \quad (2.14)$$

$$P2 = \rho + c(dt - dT) + c(\tau_{P2}^S + \tau_{P2}^R) + I_2 + d_{trop} + \varepsilon_{P2}, \quad (2.15)$$

where

$P1$ = measured pseudorange using P-code on L1

$P2$ = measured pseudorange using P-code on L2

ρ = geometric range between the satellite and receiver antenna in meter,

c = the speed of light (m/s),

dt = satellite clock error in seconds,

dT = receiver clock error in seconds,

I_1 = ionospheric delay error on L1 in meters,

I_2 = ionospheric delay error on L2 in meters,

τ^S = frequency dependent bias due to satellite hardware

τ^R = frequency dependent bias due to receiver hardware

d_{trop} = tropospheric delay error in meters,

ε_{p1} = effect of multipath and measurement noise on L1

ε_{p2} = effect of multipath and measurement noise on L2.

Similarly, the observation equation for C/A code can be given as

$$C1 = \rho + c(dt - dT) + c(\tau_{C1}^S + \tau_{C1}^R) + I_1 + d_{trop} + \varepsilon_{C1}, \quad (2.16)$$

It is easily seen that the multipath and noise term (ε_{C1}), and hardware delays (τ^S, τ^R) are not the same for P and C/A code. Also it should be noted that C/A code only modulated on L1 signal (Hofmann-Wellenhof, Lichtenegger, & Wasle, 2008).

The carrier phase observable is made in the frequency domain by getting the difference of the received phase and the receiver generated phase. However, as the carrier does not contain any information about its transmission time, the receiver can only detect the variation in the phase and there would be an ambiguity in the number of complete carrier cycles. By solving the ambiguity in the cycles, carrier phase can provide more accurate position information than pseudorange.

The carrier phase observation equations for L1 and L2 can be expressed in distance units as follow;

$$\Phi1 = \rho + c(dt - dT) + c(T_1^S + T_1^R) + \lambda_1 N_1 - I_1 + d_{trop} + \varepsilon_{L1}, \quad (2.17)$$

$$\Phi2 = \rho + c(dt - dT) + c(T_2^S + T_2^R) + \lambda_2 N_2 - I_2 + d_{trop} + \varepsilon_{L2}, \quad (2.18)$$

where

λ = carrier wavelength in meters,

N = integer ambiguity in cycles,

ε_L =carrier phase multipath error in meters,

T = frequency dependent bias due to satellite and receiver hardware.

It should be noted that although the effect of the ionosphere on the carrier phase and code have the same amount, they adopt opposite signs as it can be seen from the related observation equations (Langerly, 1998).

2.2.2 GPS observables Error Sources

GPS observation errors can be categorized in three groups; satellite related errors, receiver related errors and signal propagation errors. The satellite related errors include satellite clock error, orbital error, and errors due to satellites' hardware. The receiver related errors are receiver clock error and errors for the hardware of receiver. The third category consists of ionospheric, tropospheric delays and multipath error.

Orbital error

GPS satellite orbits can be determined in two ways; broadcast ephemerides and precise ephemerides. In the first method, the Keplerian and perturbation parameters are transmitted in the navigation message and the satellite coordinates are calculated from the broadcasted ephemerides. In the second method, the satellite coordinates is computed by the precise ephemerides provided by IGS⁴. Precise ephemerides data can be categorized in three classes based on the accuracy that they can offer. The first class is final orbit that is available after 2 weeks. The second one, rapid orbit, is ready to use after 17 hours. The ultra-rapid orbits, third form, are available after 3 hours. The accuracy of broadcast ephemerides is approximately 1 m

⁴ International GPS Service

and the accuracy of precise ephemerides is at the level of 5cm or better (Hofmann-Wellenhof, Lichtenegger, & Wasle, 2008).

Clock Errors

The GPS operates with its own time scale, called GPS time. It is a time system that uses atomic time scale and it is referenced to Universal Time Coordinates (UTC). Drifts in the oscillator of either satellite or receiver are the reason for the clock error in the GPS observations. The GPS satellites are equipped with the atomic clocks that are very accurate and stable. However, the error rises from the offset between the GPS time and the satellite clock which is usually less than 1 millisecond. This error is monitored and the correction of it is broadcasted as a part of navigation message by the control segment (Mohinder, Lawrence, & Angus, 2007).

The clocks used in the receivers are less accurate than the satellites' clock and because of that they impose larger errors to the GPS observations. Receiver clock errors can be estimated as a parameter in the observation equation or can be eliminated by the differencing approaches.

Hardware Delay

Frequency dependent biases in pseudorange and carrier phase observations originate from the delay in hardware of satellite and receiver. Generally they are modeled in the observation equation with clock error. However, they should be considered in combinations of measurements such as geometry linear combination for ionosphere modeling (Datch, Hugentobler, Fridez, & Meindle, 2007).

Tropospheric Delay

The transmitted GPS signals travel through the troposphere before it reaches to the receiver. Troposphere is the lower part of the atmosphere which starts from the Earth surface up to 50km. It is not a dispersive medium for GPS signals which means that it

has equal effects on the code and pseudorange observables of L1 and L2 signals. Tropospheric delay causes attenuation, delay and short term variations in the GPS signals. It forms by two components namely dry and wet troposphere. Dry component, which mainly depends on the atmospheric pressure and temperature, contains the 90% of the total tropospheric error. The dry component has a low temporal variation and its magnitude is about 2.3 meters in the zenith direction. In contrast, the wet component has high spatial and temporal variations and its amount changes between 1 and 80cm in vertical direction. Apparently, wet component depends mostly on water vapor (Spilker, 1996). The tropospheric delay mathematically can be expressed as follows;

$$d_{trop} = d_{dry} \cdot m_{dry} + d_{wet} \cdot m_{wet} \quad (2.19)$$

where

d_{trop} = total tropospheric delay,

d_{dry} and d_{wet} = dry delay and wet delay respectively at zenith, and

m_{dry} and m_{wet} = the corresponding mapping factors to map the zenith delay to the slant direction of satellite-receiver line-of-sight.

Multipath Error

The multipath error occurs when the directly received signal is degraded by an indirectly received signal. The indirect signal reaches the receiver by reflecting from the various surrounding objects such as buildings (Figure 3). The observations come from low elevation angle are more sensitive for multipath effect. The amount of multipath error in the code observations is much greater than in the carrier phase observations. In an extreme situation multipath error can reach 15m for the code

measurements while this amount is about 5-6 cm in the carrier phase observations (Ray, 2000). Selecting clear antenna location which is not close to any reflective object can reduce or eliminate the multipath error. It can also be mitigated using some receiver processing software.

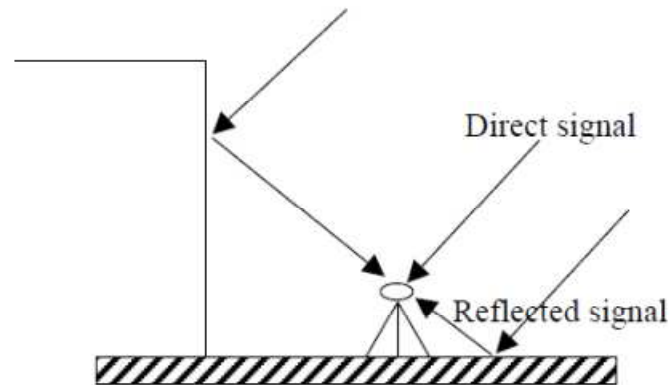


Figure 3 multipath and direct signals

Ionospheric Delay

The ionosphere is the main region in upper atmosphere which has the largest impact on the GPS signal among other error sources. Because of its dispersive characteristics, it shows different delay errors in L1 and L2 signals. On the basis of this feature, the ionospheric effect can be computed in dual frequency GPS receivers. The magnitude of the ionospheric delay can change between few meters and tens of meters in vertical direction. These amounts can be 3 times larger in range observations which are near the horizon. The effect of ionosphere over the GPS signals will be discussed in detail in section 3.3 of this chapter.

2.3 Ionospheric Impacts on GPS signal

The ionosphere has 3 effects on the GPS signal. These effects are group delay and phase advance, Doppler shift, and scintillation. As it is mentioned previously Doppler shift will not be considered in this study.

The ionosphere causes range errors in the GPS observations. However it has completely opposite effect on code and carrier phase observables. The code pseudorange measurements are observed longer than geometric range and carrier phase measurements are observed shorter because of the ionosphere. The error for the first one is named group delay and for the second one called carrier phase advance. It is because of various propagation speeds of signals with different frequencies in the ionosphere. These points have been illustrated in mathematical forms in section 2.2.1 of this chapter.

Electron density irregularities, along the GPS signal in the ionosphere cause rapid random variations in phase and amplitude of the signal. These irregularities are known as scintillation. The period of scintillation is related to the amount of electron density irregularities in the ionosphere (Figure 4). These irregularities can move inside the ionosphere. It also can cause rapid variations in the refractive index of the medium which can lead to diffraction of the signal.

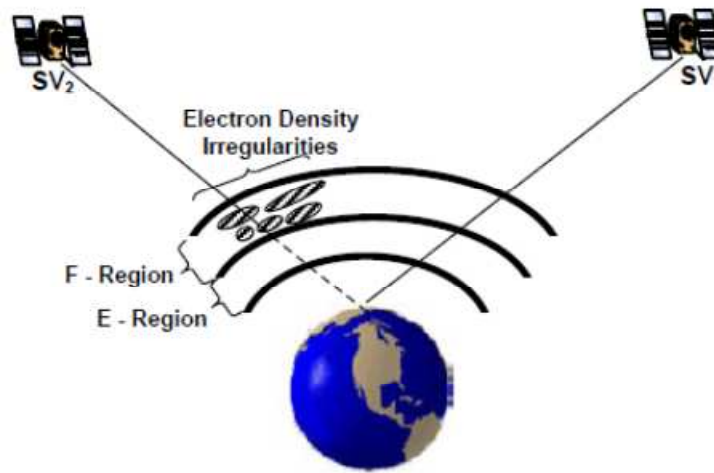


Figure 4 the electron density irregularities in the ionosphere

Amplitude scintillation can cause reduced signal power in the receiver which can end up in signal fading. Severe fading in signals cause major decrement in signal to noise ratio (SNR) in a way that SNR value falls below the receiver tracking threshold. Phase scintillation increases the dynamic stress on the phase lock loop (PLL). If the phase changes produced by the scintillation is faster than the receiver carrier tracking bandwidth then receiver loses phase lock.

Ionospheric scintillation is a serious problem for GPS users during the periods of high solar activity. Scintillation also depends on the user's location. Whereas it is a severe concern for GPS users in polar and equatorial regions, users in mid-latitude region do not encounter a major problem due to the scintillation (El Gizawy, 2003).

2.4 Extracting Ionospheric Information from GPS observations

2.4.1 The Geometry-Free linear combination of GPS observations

The geometry-free linear combination of GPS observations is computed by subtracting simultaneous pseudorange (P1-P2 or C1-P2) or carrier phase observations ($\Phi_1 - \Phi_2$) of L1 and L2 signals. This method is usually used for the ionospheric investigations because all frequency independent biases and geometric range are eliminated (Ciraolo, Azpilicueta, Brunini, Meza, & radicella, 2007). In mathematical terms, the geometry-free linear combination of the pseudorange measurements can be computed using equations 2.14 and 2.15 as follows

$$P_4 = P_1 - P_2 = I_1 - I_2 + c(\tau_{p1}^R - \tau_{p2}^R) + c(\tau_{p1}^S - \tau_{p2}^S) + \varepsilon_p, \quad (2.20)$$

The $c(\tau_{p1}^R + \tau_{p2}^R)$ and $c(\tau_{p1}^S + \tau_{p2}^S)$ are known as inter-frequency biases (IFBs) and caused by receiver and satellite hardware. By replacing them as “*br*” and “*bs*” respectively and substituting the ionospheric delay (equation 2.13) in the equation 2.20, geometry-free linear combination of the pseudorange measurements can be obtained by

$$P_4 = 40.3STE C \left(\frac{f_2^2 - f_1^2}{f_1 f_2} \right) + br + bs + \varepsilon_p. \quad (2.21)$$

In equation 2.21 the Slant Total Electron Content (STEC) is the number of free electrons in a column of 1 m^2 which extends along the ray-path of the signal. By

using equations 2.17 and 2.18 the geometry-free linear combination for the carrier phase observations can be expressed as follow

$$\Phi_4 = \Phi_1 - \Phi_2 = I_2 - I_1 + \lambda_1 N_1 - \lambda_2 N_2 + c(T_1^R - T_2^R) + c(T_1^S - T_2^S) + \varepsilon_L, \quad (2.22)$$

Similarly by replacing the IFBs in term of “Br” and “Bs” in the equation 2.22 the geometry-free linear combination for the carrier phase observations can be re-written as

$$\Phi_4 = -40.3 STEC \left(\frac{f_2^2 - f_1^2}{f_1 f_2} \right) + \lambda_1 N_1 - \lambda_2 N_2 + Br + Bs + \varepsilon_L, \quad (2.23)$$

2.4.2 Adjustment of the GPS observations

According to the previous section the STEC can be extracted from both pseudorange and carrier phase geometry-free linear combinations. However, the accuracy of the carrier phase observations is much better than the pseudorange ones. On the other hand, there is an ambiguity term in the carrier phase observations. The pseudorange measurements can be smoothed by the carrier phase observations, for taking the advantages of the unambiguous pseudorange measurements and precise carrier phase observations. There are several methods for this purpose. The method used in this work is “*carrier to code leveling processing*” with some modifications (Ciraolo,2007; Nohutcu, 2009).

By summing the equations 2.20 and 2.22 the following equation can be reached

$$P_4 + \Phi_4 = \lambda_1 N_1 - \lambda_2 N_2 + Br + Bs + br + bs + \varepsilon_p \quad (2.24)$$

As the noise and multipath effect of carrier phase, ε_L , is very smaller than the one for pseudorange, ε_P , it has been neglected in the equation 2.24. In each continuous arc the ambiguity terms are constant. Arc is a group of sequential carrier phase observations without any discontinuities. Also the IFB terms can be assumed as constant terms for an arc. So, an average value of the equation 2.24 for a continuous arc can be determined as follow

$$\begin{aligned}\langle P_4 + \Phi_4 \rangle_{arc} &= \frac{1}{n} \sum_{i=1}^n (P_4 + \Phi_4)_i, \\ &= \langle \lambda_1 N_1 - \lambda_2 N_2 \rangle_{arc} + Br + Bs + br + bs + \langle \varepsilon_P \rangle_{arc}\end{aligned}\quad (2.25)$$

Where n is the number of observations in the arc. The ambiguity terms can be removed by subtracting the equation 2.22 from 2.25

$$\tilde{P}_4 = \langle P_4 + \Phi_4 \rangle_{arc} - \Phi_4 \approx I_1 - I_2 + br + bs + \langle \varepsilon_P \rangle_{arc} + \varepsilon_L \quad (2.26)$$

Where \tilde{P}_4 is the smoothed pseudorange ionospheric observable. Substituting equation 2.13 in the equation 2.26, STEC can be computed

$$\tilde{P}_4 = 40.3 STEC \left(\frac{f_2^2 - f_1^2}{f_1^2 f_2^2} \right) + br + bs + \langle \varepsilon_P \rangle_{arc} - \varepsilon_L, \quad (2.27)$$

or

$$STEC = \left(\tilde{P}_4 - br - bs - \langle \varepsilon_P \rangle + \varepsilon_L \right) \frac{f_1^2 f_2^2}{40.3(f_2^2 - f_1^2)} \quad (2.28)$$

The unit of STEC is TECU and 1 TECU is equal to 10^6 electron/m².

2.4.3 Differential Code Biases

The IFBs for pseudorange measurements are usually known as the Differential Code Biases (DCB). Together with phase measurements, dual frequency receivers offer C/A code measurements. Also they can provide a subset of P1, P2 and X2 code observations which depend on the type of the receiver. The X2, offered by the cross-correlation receivers, is equal to $C1+(P2-P1)$. Based on the provided code observations, GPS receivers can be divided to 3 groups (Table 2).

Table 2 GPS receiver types based on the type of provided code measurements

Receiver Type	Provided code observables
P1/P2	C1, P1, P2
C1/P2	C1, P2
C1/X2	C1, $C1+(P2-P1)$

The C1 code is eliminated in the P1/P2 receiver measurements because it has a lower accuracy compared to the P1 code observations. Frequency dependent biases cannot be determined in absolute manner. On the other hand, their differential forms (DCB) are crucial for ionosphere modeling. Although DCBs vary by time, they can be assumed consistent for periods of day to months.

DCB values between P1 and P2 (DCB_{P1P2}) can be found in geometry free linear combination of P1 and P2 or P1 and X2. However, in C1/P2 type of receivers, another differential bias term between P1 and C1 (DCB_{P1C1}) must be taken into the account. Furthermore, in the STEC calculation of this type of receivers, DCB parameters for the receivers and the satellites, br and bs , must be improved with DCB_{P1C1} as follows

$$br = DCB_{P1P2}^R - DCB_{C1P2}^R, \quad (2.29)$$

$$bs = DCB_{P1P2}^S - DCB_{C1P2}^S. \quad (2.30)$$

IGS analysis center provides DCB values for satellites with high accuracy level through internet whereas receiver DCBs should be estimated as a parameter in ionosphere modeling (Nohutcu,2009).

2.4.4 Cycle Slip Detection

As the connection between the receiver and satellite is taken place (receiver locked to a satellite) and signal acquisition starts, an integer counter for the number of carrier wave cycles between the satellite and receiver is initialized. As long as the signal lock continues, the integer number remains constant. It has been mentioned in prior sections that the integer number, so called ambiguity term, is unknown. If an interruption occurs in phase lock then the integer counter is restarted which can results in a jump in carrier phase measurement. This phenomenon called cycle slip. Failure in the receiver, signal obstruction, high SNR, and low signal strength can be a source for cycle slip (Seeber, 2003).

Cycle slip in the phase measurements can be detected from continues arcs of carrier phase observations because the ambiguity terms are constant. It is explained in the adjusting the GPS observations part. There are several methods for cycle slip detection. In this work the same approach has been used as it is installed in TECmapper which is an ionosphere modeling software prepared in the Geomatics laboratory of Middle East Technical University (Nohutcu, 2009). It is based on the processing observation files individually and uses the combination of phase and code ranges for cycle slip detection. In this method two following testing quantities are used for cycle slip detection:

$$\Phi_1 - P_1 = \lambda_1 N_1 - 2I_1 + c(T_1^S + T_1^R - \tau_{P1}^S - \tau_{P1}^R) + \varepsilon_{P1}, \quad (2.31)$$

$$\Phi_2 - P_2 = \lambda_2 N_2 - 2I_2 + c(T_2^S + T_2^R - \tau_{P2}^S - \tau_{P2}^R) + \varepsilon_{P2}. \quad (2.32)$$

ε_{L1} and ε_{L2} has been neglected because of their smaller amount in comparison with ε_{P1} and ε_{P2} . The ambiguity terms are constant and IFBs are invariant for days to months and the variation in ionospheric effect is too small for epochs with small intervals. Irregular variations of testing quantities can be an indicator for cycle slip. The main drawback of this method is the noise terms because small cycle slips can be ignored due to the noise level of pseudorange observations. As the measurement resolutions of the receivers in CORS⁵ stations are improved continuously, this method can be a proper one for cycle slip detection (Hofmann-Wellenhof, Lichtenegger, & Wasle, 2008).

2.4.5 Single Layer Model of Ionosphere

Based on the fact that the STEC provides the ionospheric information along the signal ray and not in a tomographic profile, usually a single layer model is used for ionosphere modeling in terms of TEC. Single layer model is a shell with infinitesimal thickness and it is assumed that all of the electrons concentrated in this shell. Vertical Total Electron Content (VTEC) is frequently used for the formation of single layer model. The height of this layer depends on the altitude of the maximum electron density and it is usually between 350 km and 450 km from the Earth surface (Figure 5) (Schaer,1999)

⁵ Continuously Operating Reference Station

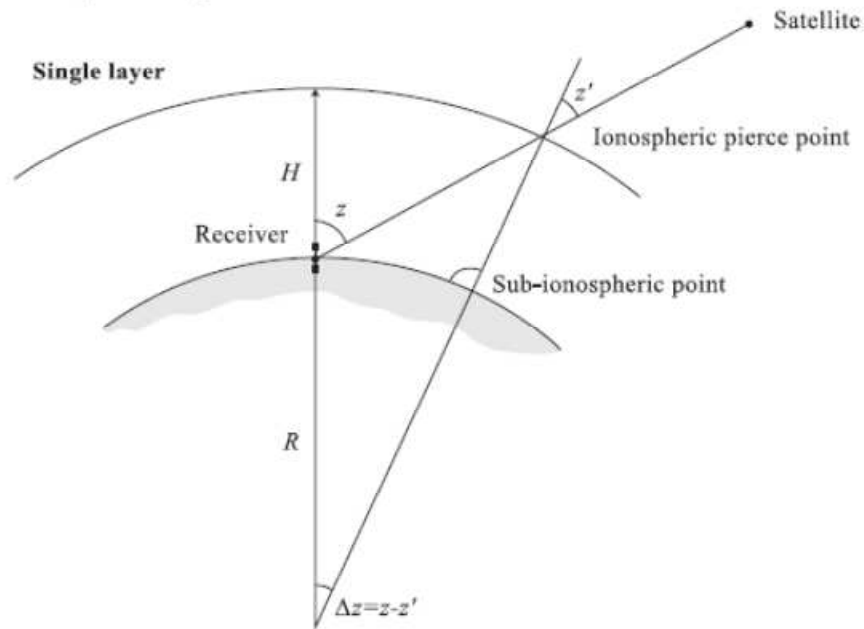


Figure 5 the single layer model for ionosphere (Schaer,1999)

In Figure 5;

- Ionospheric point or ionospheric pierce point (IPP) is the intersection of receiver to satellite line of sight with single layer,
- R is the Earth mean radius,
- H is the single layer height,
- z is the zenith angel of the satellite at receiver location,
- z' is the zenith angel of the satellite at IPP.

It was mentioned that VTEC is used for single layer model. VTEC can be obtained by multiplying mapping function with STEC. The mapping function, $F(Z)$, used in this work is expressed below.

$$F(Z) = \frac{STEC}{VTEC} = \frac{1}{\cos z_{IPP}}, \quad (2.33)$$

also,

$$\sin z_{IPP} = \frac{R}{R+H} \sin z \quad (2.34)$$

If STEC in equation 2.27 is replaced by equation 2.33 the following formulas are obtained

$$\tilde{P}_4 = VTEC \frac{F(z)}{\gamma} + br + bs + \varepsilon, \quad (2.35)$$

$$\gamma = \frac{f_1^2 f_2^2}{40.3(f_2^2 - f_1^2)}. \quad (2.36)$$

The law of sines and cosines for spherical triangles is used for computing coordinates of ionospheric point or IPP. In this case, spherical triangle is formed by the North Pole, receiver and ionospheric point (Figure 6).

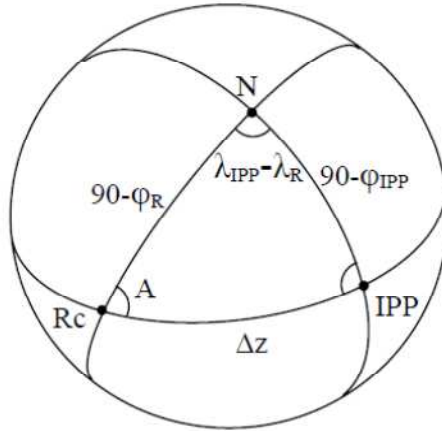


Figure 6 Spherical triangle formed by receiver, North Pole and IPP (Nohutcu, 2009)

In figure 6;

- A : azimuth angel of the satellite observed at receiver location
- λ_{Rc} : geographic longitude of the receiver
- λ_{IPP} : geographic longitude of the IPP
- φ_{Rc} : geographic latitude of the receiver
- φ_{IPP} : geographic latitude of the IPP

$$\cos(90 - \varphi_{IPP}) = \cos(90 - \varphi_{Rc}) \cos(\Delta z) + \sin(90 - \varphi_{Rc}) \sin(\Delta z) \cos(A), \quad (2.37)$$

$$\frac{\sin(A)}{\sin(90 - \varphi_{IPP})} = \frac{\sin(\lambda_{IPP} - \lambda_{Rc})}{\sin(\Delta z)}. \quad (2.38)$$

Using equations 2.37 and 2.38, geographic coordinates of IPP can be computed as follows

$$\varphi_{IPP} = \sin^{-1}(\sin(\varphi_{Rc}) \cos(\Delta z) + \cos(\varphi_{Rc}) \sin(\Delta z) \cos(A)), \quad (2.39)$$

$$\lambda_{IPP} = \lambda_R + \sin^{-1}\left(\frac{\sin(A) \sin(\Delta z)}{\cos(\varphi_{IPP})}\right). \quad (2.40)$$

CHAPTER 3

Optimal State Estimation; Kalman Filtering and Particle Filtering

The measurements that have been observed in the real world are subjected to errors. Elimination of all error sources is impossible and some of them can only be reduced. On the other hand, there are some unknowns or parameters that should be estimated based on these measurements. Reduction or elimination of measurement errors and estimating the parameters is one of the main parts in many engineering or scientific work.

Measurements can relate to the parameters through a function which results in a deterministic model. The functional model has a direct impact on the error propagation and mathematically can be defined as

$$y = f(\beta) \quad (3.1)$$

For making the model consistent, the error term should be added to the measurements. Also a stochastic part is needed. The equations are given below.

$$\mathbf{y}_{n \times 1} + \mathbf{e}_{n \times 1} = \mathbf{X}_{n \times u} \boldsymbol{\beta}_{u \times 1}, \quad (3.2)$$

$$D(\mathbf{y}) = D(\mathbf{e}) = \sigma^2 \mathbf{P}^{-1}. \quad (3.3)$$

Where

\mathbf{y} : measurement vector,

\mathbf{e} : random measurement error,

\mathbf{X} : configuration matrix,

$\boldsymbol{\beta}$: parameter vector,

n : number of measurements,

u : number of parameters,

$D(\mathbf{y})$: variance covariance matrix of observations

σ : apriori variance factor of observations,

\mathbf{P}^{-1} : weight matrix

The equations 3.2 and 3.3 together are called Gauss-Markov Model. The equation 3.2 is functional part known as observation equation. The equation 3.3 is the stochastic part. There are several methods for estimating the parameters. One of them is the Least Squares method which is based on the minimization of the sum of residuals. Detailed information about this method can be found in *Koch, 1997*. Here, the estimated parameters and relevant covariance matrix are provided

$$\hat{\boldsymbol{\beta}} = (\mathbf{X}'\mathbf{P}\mathbf{X})^{-1} \mathbf{X}'\mathbf{P}\mathbf{y}, \quad (3.4)$$

$$D(\hat{\boldsymbol{\beta}}) = \hat{\sigma}^2 (\mathbf{X}'\mathbf{P}\mathbf{X})^{-1}. \quad (3.5)$$

3.1 Recursive Parameter Estimation

The observations may be collected in different time epochs. So, they can be separated in two uncorrelated vectors, \mathbf{y}_{m-1} and \mathbf{y}_m with $m \in \{2, \dots, l\}$. The parameters can be estimated in each epoch. So, the Gauss-Markov model can be expressed as follows

$$\mathbf{X} = \begin{vmatrix} \mathbf{X}_{m-1} \\ \mathbf{X}_m \end{vmatrix}, \mathbf{y} = \begin{vmatrix} \mathbf{y}_{m-1} \\ \mathbf{y}_m \end{vmatrix} \quad \text{and} \quad D(\mathbf{y}) = \sigma^2 \begin{vmatrix} \mathbf{P}_{m-1}^{-1} & \mathbf{0} \\ \mathbf{0} & \mathbf{P}_{m-1}^{-1} \end{vmatrix}.$$

Then the estimated parameters can be computed using equation 3.4 in this way

$$\hat{\boldsymbol{\beta}} = (\mathbf{X}'_{m-1} \mathbf{P}_{m-1} \mathbf{X}_{m-1} + \mathbf{X}'_m \mathbf{P}_m \mathbf{X}_m)^{-1} (\mathbf{X}'_{m-1} \mathbf{P}_{m-1} \mathbf{y}_{m-1} + \mathbf{X}'_m \mathbf{P}_m \mathbf{y}_m). \quad (3.6)$$

It is assumed that the $\hat{\boldsymbol{\beta}}_{m-1}$ is the estimated parameters with \mathbf{y}_{m-1} and its corresponding covariance matrix, $D(\hat{\boldsymbol{\beta}}_{m-1}) = \sigma^2 \boldsymbol{\Sigma}_{m-1}$. If $\hat{\boldsymbol{\beta}} = \hat{\boldsymbol{\beta}}_m$, where $\hat{\boldsymbol{\beta}}_m$ is the estimated parameters based on added observation \mathbf{y}_m , using equation 3.4 instead of 3.6, it can be expressed that

$$\hat{\boldsymbol{\beta}}_m = (\boldsymbol{\Sigma}_{m-1}^{-1} + \mathbf{X}'_m \mathbf{P}_m \mathbf{X}_m)^{-1} (\boldsymbol{\Sigma}_{m-1}^{-1} \hat{\boldsymbol{\beta}}_{m-1} + \mathbf{X}'_m \mathbf{P}_m \mathbf{y}_m), \quad (3.7)$$

where $D(\hat{\boldsymbol{\beta}}_m) = \sigma^2 \boldsymbol{\Sigma}_m$. Based on the 3.4, $\boldsymbol{\Sigma}_m$ is equal to the inverse of normal equations in 3.7 and can be obtained by

$$\boldsymbol{\Sigma}_m = \boldsymbol{\Sigma}_{m-1} - \mathbf{F}_m \mathbf{X}_m \boldsymbol{\Sigma}_{m-1}, \quad (3.8)$$

with

$$\mathbf{F}_m = \boldsymbol{\Sigma}_{m-1} \mathbf{X}'_m (\mathbf{P}_m^{-1} + \mathbf{X}_m \boldsymbol{\Sigma}_{m-1} \mathbf{X}'_m)^{-1}. \quad (3.9)$$

By combining equation 3.9 with 3.7, the following equation is obtained

$$\hat{\boldsymbol{\beta}}_m = \hat{\boldsymbol{\beta}}_{m-1} + \mathbf{F}_m (\mathbf{y}_m - \mathbf{X}_m \mathbf{P}_m \hat{\boldsymbol{\beta}}_{m-1}). \quad (3.10)$$

If the parameters are the state variables of a dynamic system transformed from t_{m-1} to t_m , the equations from 3.8 and 3.10 are the correction step of the Kalman filtering (Koch, 1997). Kalman filter will be explained briefly in section 3.3.

3.2 Recursive Bayesian Estimation

In Bayesian method, the posterior distribution, $p(\mathbf{x}_k | \mathbf{Y}_k)$, of the parameter vector, \mathbf{x}_k , conditioned on observation matrix, $\mathbf{Y}_k = \{\mathbf{y}_1, \mathbf{y}_2, \dots, \mathbf{y}_k\}$, is calculated for estimating the state vector, \mathbf{x}_k , with measurements \mathbf{Y}_k . The posterior distribution keeps all information about state vector and prior distribution. In the case of known posterior distribution, the optimal estimation of the state can be calculated in this way

$$\hat{\mathbf{x}}_k = E(\mathbf{x}_k | \mathbf{Y}_k) = \int \mathbf{x}_k p(\mathbf{x}_k | \mathbf{Y}_k) d\mathbf{x}_k. \quad (3.11)$$

The *Bayes theorem* is used for calculating the posterior density of the state vector. Based on the *Bayes theorem*, the posterior density for x given y is proportional to the prior density of x , $p(x)$, multiplied by likelihood of y , $p(y|x)$, or in mathematical terms

$$p(x|y) \propto p(x)p(y|x). \quad (3.12)$$

One of the complexities of the calculating posterior distribution is the computational load because of high dimensional integration. This problem can be solved by changing it to the sequential terms. It is obvious that

$$p(\mathbf{x}_1, \dots, \mathbf{x}_k | \mathbf{Y}_k) \propto p(\mathbf{x}_1, \dots, \mathbf{x}_k | \mathbf{Y}_{k-1}) p(\mathbf{y}_k | \mathbf{x}_k). \quad (3.13)$$

Marginally integrating \mathbf{x}_1 to \mathbf{x}_{k-1} results in

$$p(\mathbf{x}_k | \mathbf{Y}_k) \propto p(\mathbf{x}_k | \mathbf{Y}_{k-1})p(\mathbf{y}_k | \mathbf{x}_k). \quad (3.14)$$

Using Markov structure of the system equation gives

$$p(\mathbf{x}_k, \mathbf{x}_{k-1} | \mathbf{Y}_{k-1}) = p(\mathbf{x}_{k-1} | \mathbf{Y}_{k-1})p(\mathbf{x}_k | \mathbf{x}_{k-1}). \quad (3.15)$$

Thus the PDFs can be updated recursively. By using the previous equations, the prediction and update equations can be obtained. The probability prediction (Chapman-Kolmogorov) equation can be given as

$$p(\mathbf{x}_k | \mathbf{Y}_{k-1}) = \int p(\mathbf{x}_k | \mathbf{x}_{k-1})p(\mathbf{x}_{k-1} | \mathbf{Y}_{k-1})d\mathbf{x}_{k-1}. \quad (3.16)$$

The update equation can be calculated by adding the new measurements as the observation likelihood

$$p(\mathbf{x}_k | \mathbf{Y}_k) = c_k p(\mathbf{y}_k | \mathbf{x}_k)p(\mathbf{x}_k | \mathbf{Y}_{k-1}), \quad (3.17)$$

where c_k is the normalizing factor

$$c_k = \left(\int p(\mathbf{y}_k | \mathbf{x}_k)p(\mathbf{x}_k | \mathbf{Y}_{k-1})d\mathbf{x}_k \right)^{-1}. \quad (3.18)$$

The update equation can be written in the following form

$$p(\mathbf{x}_k | \mathbf{Y}_k) = \frac{p(\mathbf{y}_k | \mathbf{x}_k)p(\mathbf{x}_k | \mathbf{Y}_{k-1})}{p(\mathbf{y}_k | \mathbf{Y}_{k-1})}. \quad (3.19)$$

The prediction and update equations form the recursive Bayesian estimation algorithm (Figure 3.1) (Lee, 2005).

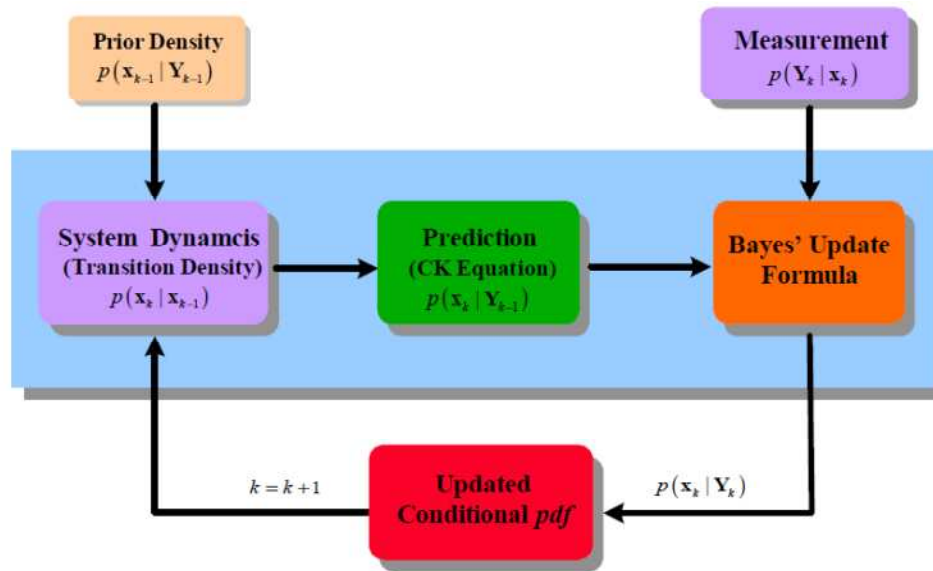


Figure 3.1 recursive Bayesian estimation (Lee, 2005)

3.3 Kalman Filter

In this section Kalman filter is explained based on the recursive Bayesian approach.

For describing Kalman filter the following system of equations must be considered

$$\mathbf{x}_k = \mathbf{F}\mathbf{x}_{k-1} + \mathbf{w}_{k-1}, \quad (3.20)$$

$$\mathbf{y}_k = \mathbf{H}\mathbf{x}_k + \mathbf{v}_k, \quad (3.21)$$

where

F: Dynamical model

x: State vector

w: Process noise

y: Observation vector

H: Measurement sensitivity matrix or observation matrix

v: Measurement noise

The equations 3.11 and 3.12 are known as system model and observation model, respectively. The measurement noise and process noise are assumed to be white and uncorrelated which means that they both have a Gaussian distribution with zero mean (Mohinder, Lawrence, & Angus, 2007). In other words

$$p(\mathbf{w}_k) = N(0, \mathbf{Q}_k), p(\mathbf{v}_k) = N(0, \mathbf{R}_k). \quad (3.22)$$

\mathbf{Q}_k is the covariance of dynamic disturbance or process noise and \mathbf{R}_k is the covariance of the sensor noise. Also, it is assumed that the initial state has a known PDF, $p(x_0)$. A similar structure of recursive Bayesian approach will be traced in Kalman filter algorithm. Dynamic and measurement models participates in computing the state transition probability and measurement likelihood function, respectively, as it will be described in the rest of this section (Lee, 2005). The state transition probability can be determined by

$$p(\mathbf{x}_{k+1} | \mathbf{x}_k) = N(\mathbf{x}_{k+1}; \hat{\mathbf{x}}_{k+1}, \mathbf{Q}_k), \quad (3.23)$$

and the likelihood function can be obtained by

$$p(\mathbf{y}_k | \mathbf{x}_k) = N(\mathbf{y}_k; \hat{\mathbf{y}}_k, \mathbf{R}_k), \quad (3.24)$$

The recursive relationships in equations 3.16 and 3.17 can be given by

$$p(\mathbf{x}_k | \mathbf{x}_k) = N(\mathbf{x}_k; \hat{\mathbf{x}}_k, \mathbf{P}_k), \quad (3.25)$$

$$p(\mathbf{x}_{k+1} | \mathbf{x}_k) = N(\mathbf{x}_{k+1}; \hat{\mathbf{x}}_k^-, \mathbf{P}_k^-), \quad (3.26)$$

$$p(\mathbf{x}_{k+1} | \mathbf{y}_{k+1}) = N(\mathbf{x}_{k+1}; \hat{\mathbf{x}}_{k+1}, \mathbf{P}_{k+1}), \quad (3.27)$$

where $N(\mathbf{x}; \mathbf{m}, \mathbf{P})$ represents a Gaussian density with variable \mathbf{x} , mean \mathbf{m} , and covariance \mathbf{P} that can be shown mathematically as

$$N(\mathbf{x}; \mathbf{m}, \mathbf{P}) = |2\pi\mathbf{P}|^{-1/2} \exp\left\{-\frac{1}{2}(\mathbf{x} - \mathbf{m})\mathbf{P}^{-1}(\mathbf{x} - \mathbf{m})^T\right\}. \quad (3.28)$$

For simplification, the Bayesian recursion can be represented in terms of conditional mean and conditional covariance.

$$\hat{\mathbf{x}}_k^- = E\left\{\mathbf{F}\mathbf{x}_{k-1} + \mathbf{w}_{k-1} \mid \mathbf{Y}^{k-1}\right\} = \mathbf{F}\hat{\mathbf{x}}_{k-1}, \quad (3.29)$$

$$\hat{\mathbf{y}}_k^- = E\left\{\mathbf{H}\hat{\mathbf{x}}_k^- + \mathbf{v}_k \mid \mathbf{Y}^{k-1}\right\}, \quad (3.30)$$

where $\hat{\mathbf{x}}_k^-$ is the model prediction and its corrected version ($\hat{\mathbf{x}}_k^+$) is determined by bringing the observations \mathbf{y}_k into account. This is obtained by

$$\hat{\mathbf{x}}_k^+ = \hat{\mathbf{x}}_k^- + \mathbf{K}_k \mathbf{v}_k, \quad (3.31)$$

\mathbf{K}_k is the Kalman gain and \mathbf{v}_k is the innovation vector.

$$\mathbf{v}_k \equiv \mathbf{y}_k - \hat{\mathbf{y}}_k^- = \mathbf{y}_k - \mathbf{H}\hat{\mathbf{x}}_k^- \quad (3.32)$$

The predicted and updated equations of state covariance are determined by

$$\mathbf{P}_k^- = \mathbf{F}\mathbf{P}_{k-1}\mathbf{F}^T + \mathbf{Q}_{k-1}, \quad (3.33)$$

$$\mathbf{P}_k^+ = \mathbf{P}_k^- - \mathbf{K}_k \mathbf{S}_k \mathbf{K}_k^T. \quad (3.34)$$

\mathbf{S}_k is the covariance of innovation vector and computed as follows

$$\mathbf{S}_k = \mathbf{H}\mathbf{P}_k^-\mathbf{H}^T + \mathbf{R}_k. \quad (3.35)$$

Kalman gain is calculated as follows

$$\mathbf{K}_k = \mathbf{P}_k^-\mathbf{H}^T\mathbf{S}_k^{-1}. \quad (3.36)$$

Ultimately, the Kalman filter algorithm can be found in the Table 3.

Table 3 the Kalman filter algorithm (Lee, 2005)

- Initialization:
 - $\hat{\mathbf{x}}_0 = E[\mathbf{x}_0]$
 - $\mathbf{P}_0 = E[(\mathbf{x}_0 - \hat{\mathbf{x}}_0)(\mathbf{x}_0 - \hat{\mathbf{x}}_0)^T]$
- State propagation:
 - $\hat{\mathbf{x}}_k^- = \mathbf{F}_{k-1}\hat{\mathbf{x}}_{k-1}$
 - $\mathbf{P}_k^- = \mathbf{F}_{k-1}\mathbf{P}_{k-1}\mathbf{F}_{k-1}^T + \mathbf{Q}_{k-1}$
- Observation propagation:
 - $\hat{\mathbf{y}}_k^- = \mathbf{H}_k\hat{\mathbf{x}}_k^-$
 - $\mathbf{S}_k = \mathbf{H}\mathbf{P}_k^-\mathbf{H}^T + \mathbf{R}_k$
- Update:
 - $\mathbf{K}_k = \mathbf{P}_k^-\mathbf{H}^T\mathbf{S}_k^{-1}$
 - $\mathbf{P}_k^+ = \mathbf{P}_k^- - \mathbf{K}_k\mathbf{S}_k\mathbf{K}_k^T$
 - $\hat{\mathbf{x}}_k^+ = \hat{\mathbf{x}}_k^- + \mathbf{K}_k\mathbf{v}_k$

Where (-) shows propagated values and (+) indicates updated values.

3.4 Particle Filter

Many of the dynamical systems are nonlinear and estimation of these systems from sequential observation is a considerable concern for scientists and engineers. There is not a comprehensive method for coping with nonlinear and non-Gaussian systems. Kalman filter and its derivations (Extended Kalman, Unscented Kalman, etc.) and some other similar algorithms are based on the local linearization and working over Gaussian systems. Because of this reason, nowadays, a new class of filtering techniques based on Sequential Monte Carlo (SMC) approach is used for estimating non-linear and non-Gaussian systems. In SMC for solving online estimation problem, a set of Monte Carlo simulation scheme is used. In other words, it is based on the recursively generating sets of weighted samples for state variables. Sequential Importance Sampling (SIS) forms the principal of the SMC filters. Ultimately, SMC uses samples to represent a complicated probability distribution and utilizes importance sampling and weighted resampling to perform the filtering. The SMC method is also known as Particle Filter. This filter has a flexible nature which can be more adaptive to some characteristics of the high dynamic systems. Conceptually, the difference between the Kalman filter and Particle filter is depicted in Figure 7.

As it is mentioned above, the Particle filter is implemented by recursively generating a set of weighted samples of the state variables. Each sampled particle gain a weight based on how well it agrees with the measurements. In terms of Recursive Bayesian Estimation, the samples and their weights are combined for determination of the posterior distributions. If the samples move away from the real state, their corresponding weights will tend to zero. In that case the samples with smaller weights eliminate and the ones with large weights multiply. So, the Particle filter can be executed in three steps; 1) Particle generation 2) weight computation 3)

resampling. The first two steps are the SIS parts. Because of that, first of all SIS is illustrated.

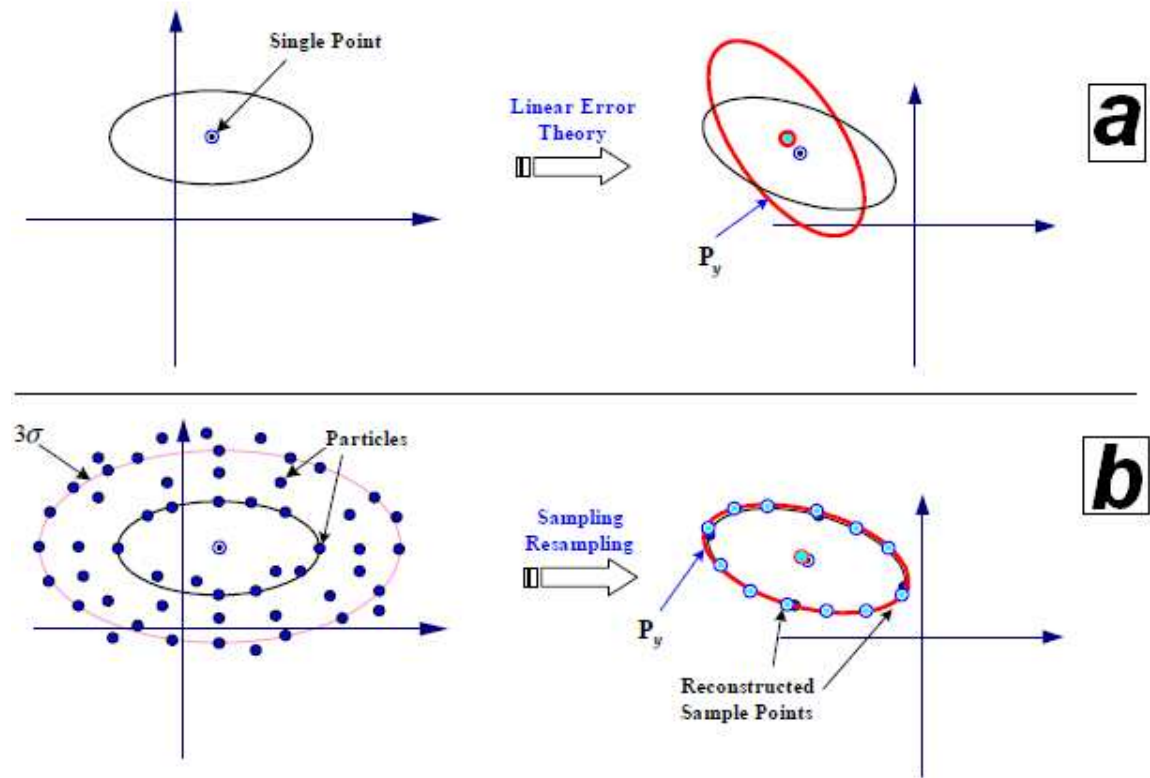


Figure 7 Sampling difference between Kalman filter (a) and Particle filter (b)(Lee, 2005)

3.4.1 Sequential Importance Sampling

Consider the discrete time dynamic and observation models as

$$\mathbf{x}_k = \mathbf{f}(\mathbf{x}_{k-1}, k-1) + \mathbf{w}_{k-1}, \quad (3.37)$$

$$\mathbf{y}_k = \mathbf{h}(\mathbf{x}_k, k) + \mathbf{v}_k. \quad (3.38)$$

It is assumed that the process and measurement noises are independent with unknown densities. The particle filter estimates the density function using samples. The estimation of the posterior can be obtained as follow

$$\hat{p}(\mathbf{X}_k | \mathbf{Y}_k) = \frac{1}{N} \sum_{i=1}^N \delta(\mathbf{X}_k - \mathbf{X}_k^{(i)}), \quad (3.39)$$

where,

$\{\mathbf{X}_k^{(i)}\}_i^N$: samples drawn from the posterior

$\delta(\mathbf{X}_k)$: Dirac delta function.

The samples are equally correct because they are drawn from the posterior itself. So, their sum of weights should be equal to one.

The equation 3.39 can be used for calculation of different moments of the posterior, for instance the expectation and the covariance

$$\hat{\mathbf{x}} = E\{\mathbf{x}\} = \int \mathbf{x} p(\mathbf{x}) d\mathbf{x} = \int \frac{1}{N} \sum_{i=1}^N \delta(\mathbf{x} - \mathbf{x}^{(i)}) \mathbf{x} d\mathbf{x} = \frac{1}{N} \sum_{i=1}^N \mathbf{x}^{(i)}, \quad (3.40)$$

$$\mathbf{P} \approx \int \frac{1}{N} \sum_{i=1}^N \delta(\mathbf{x} - \mathbf{x}^{(i)}) (\mathbf{x} - \hat{\mathbf{x}})(\mathbf{x} - \hat{\mathbf{x}})^T d\mathbf{x} = \frac{1}{N} \sum_{i=1}^N (\mathbf{x}^{(i)} - \hat{\mathbf{x}})(\mathbf{x}^{(i)} - \hat{\mathbf{x}})^T. \quad (3.41)$$

Posterior is unknown so the samples cannot be drawn from it. As an alternative way, they are drawn from a known probability density function ($q(\mathbf{X}_k | \mathbf{Y}_k)$). According to the Bayes theorem

$$q(\mathbf{X}_k | \mathbf{Y}_k) = q(\mathbf{x}_k | \mathbf{X}_{k-1}, \mathbf{Y}_k) q(\mathbf{X}_{k-1} | \mathbf{Y}_k), \quad (3.42)$$

$$q(\mathbf{X}_k | \mathbf{Y}_k) = q(\mathbf{x}_k | \mathbf{X}_{k-1}, \mathbf{Y}_k) q(\mathbf{X}_{k-1} | \mathbf{Y}_{k-1}), \quad (3.43)$$

The importance weight can be obtained as follows

$$w_k^{(i)} = \frac{p(\mathbf{X}_k^i | \mathbf{Y}_k)}{q(\mathbf{X}_k^i | \mathbf{Y}_k)} = c_k \frac{p(\mathbf{y}_k | \mathbf{x}_k^{(i)})p(\mathbf{x}_k^{(i)} | \mathbf{x}_{k-1}^{(i)})}{q(\mathbf{x}_k^{(i)} | \mathbf{X}_{k-1}^i, \mathbf{Y}_k)} w_{k-1}^{(i)}, \quad (3.44)$$

Where,

$$c_k = p(\mathbf{Y}_{k-1})/p(\mathbf{Y}_k).$$

c_k can be neglected because the relative relationship between the weights is important. As a result of this assumption

$$w_k^{(i)} = w_{k-1}^{(i)} \frac{p(\mathbf{y}_k | \mathbf{x}_k^{(i)})p(\mathbf{x}_k^{(i)} | \mathbf{x}_{k-1}^{(i)})}{q(\mathbf{x}_k^{(i)} | \mathbf{X}_{k-1}^i, \mathbf{Y}_k)}. \quad (3.45)$$

A simple but efficient way can be the drawing from the propagations density and this means

$$q(\mathbf{x}_k^{(i)} | \mathbf{X}_{k-1}^i, \mathbf{Y}_k) = q(\mathbf{x}_k | \mathbf{x}_{k-1}). \quad (3.46)$$

Then the equation 3.45 can be re-written in this form

$$w_k^{(i)} = w_{k-1}^{(i)} p(\mathbf{y}_k | \mathbf{x}_k^{(i)}). \quad (3.47)$$

Using the above equations the new estimate of the posterior can be obtained by

$$p(\mathbf{X}_k | \mathbf{Y}_k^{(i)}) = \sum_{i=1}^N \bar{w}_k^{(i)} \delta(\mathbf{X}_k - \mathbf{X}_k^{(i)}) \quad (3.48)$$

where

$$\bar{w}_k^{(i)} = \frac{w_k^{(i)}}{\sum_{j=1}^N w_k^{(j)}}. \quad (3.49)$$

At the end, the estimated mean value and covariance matrix can be determined in terms of current state and importance weights as follow

$$\hat{\mathbf{x}}_k^+ = E\{\mathbf{x}_k\} = \sum_{i=1}^N \bar{w}_k^{(i)} \mathbf{x}_k^{(i)}, \quad (3.50)$$

$$\mathbf{P}_k^+ = E\{[\mathbf{x}_k - E\{\mathbf{x}_k\}][\mathbf{x}_k - E\{\mathbf{x}_k\}]^T\} \approx \sum_{i=1}^N \bar{w}_k^{(i)} (\mathbf{x}_k^{(i)} - \hat{\mathbf{x}}_k^+)(\mathbf{x}_k^{(i)} - \hat{\mathbf{x}}_k^+)^T. \quad (3.51)$$

3.4.2 Resampling

The samples tend to distribute and weights will be almost zero for most of the samples by the evolution of time. This means that they will not have a significant contribution in posterior estimation. This problem is known as degeneracy problem in SIS. Effective sample size is a parameter for measuring the concentration of the samples in the interested region. It can be shown that the effective sample size can be determined by

$$\hat{N}_{eff} = \frac{1}{\sum_i (\bar{w}_k^{(i)})^2}. \quad (3.52)$$

Effective sample size will be N if the all weights are equal. Usually a lower threshold is used for making decision whether samples have a good distribution. Decrement in the weights of samples will result in the smaller effective sample size which eventually passes the threshold. For preventing this problem, N new samples extract with replacement. As the new samples are drawn from the estimate of posterior, all the weights should be set to $1/N$. By using this procedure, samples with high weights will be reproduced (Figure 8). There are various resampling algorithms such as simple random resampling, residual resampling and systematic resampling. The

resampling method used in this study is systematic resampling that is illustrated below.

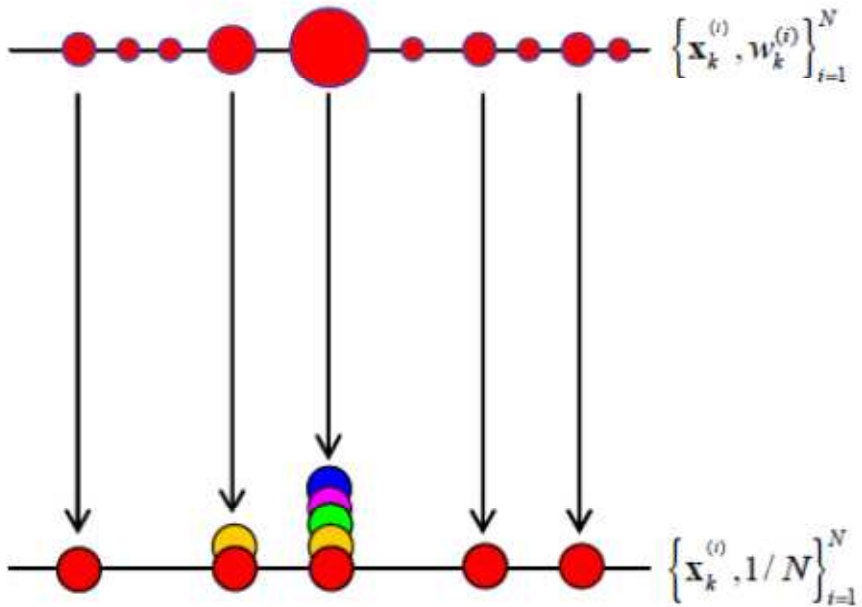


Figure 8 resampling step(Lee, 2005)

Systematic resampling is an efficient resampling scheme that uses a minimum variance method in which the uniform distribution is utilized. Each value is independently drawn from uniform distribution using following scheme

$$u_1 \sim U[0,1/N], \tag{3.53}$$

$$u_i = u_1 + \frac{i}{N}. \tag{3.54}$$

Systematic resampling algorithm can be found in the Table 4.

Table 4 the resampling algorithm (Lee, 2005)

<ol style="list-style-type: none">1. Initialization at $i = 1$<ul style="list-style-type: none">- Set $c_1 = 0$2. For $i = 2, \dots, N$<ul style="list-style-type: none">- Construct $c_i = c_{i-1} + w_k^i$3. Set $i = 1$4. Draw a starting point<ul style="list-style-type: none">- $u_1 \sim U[0, 1/N]$5. For $j = 1, \dots, N$<ul style="list-style-type: none">- Construct $u_j = u_1 + (j - 1)/N$- While $u_j > c_i$<ul style="list-style-type: none">• $i = i + 1$- Otherwise<ul style="list-style-type: none">• Assign sample: $\mathbf{x}_k^j = \mathbf{x}_k^i$• Assign weight: $w_k^j = 1/N$
--

3.4.3 Generic Particle Filter

All the background that is provided in this section can be considered as steps of particle filter implementation. The generic particle filter algorithm can be found in Table 5 and it is illustrated schematically in Figure 9. It should be noted that the selection of the importance distribution is the most important issue.

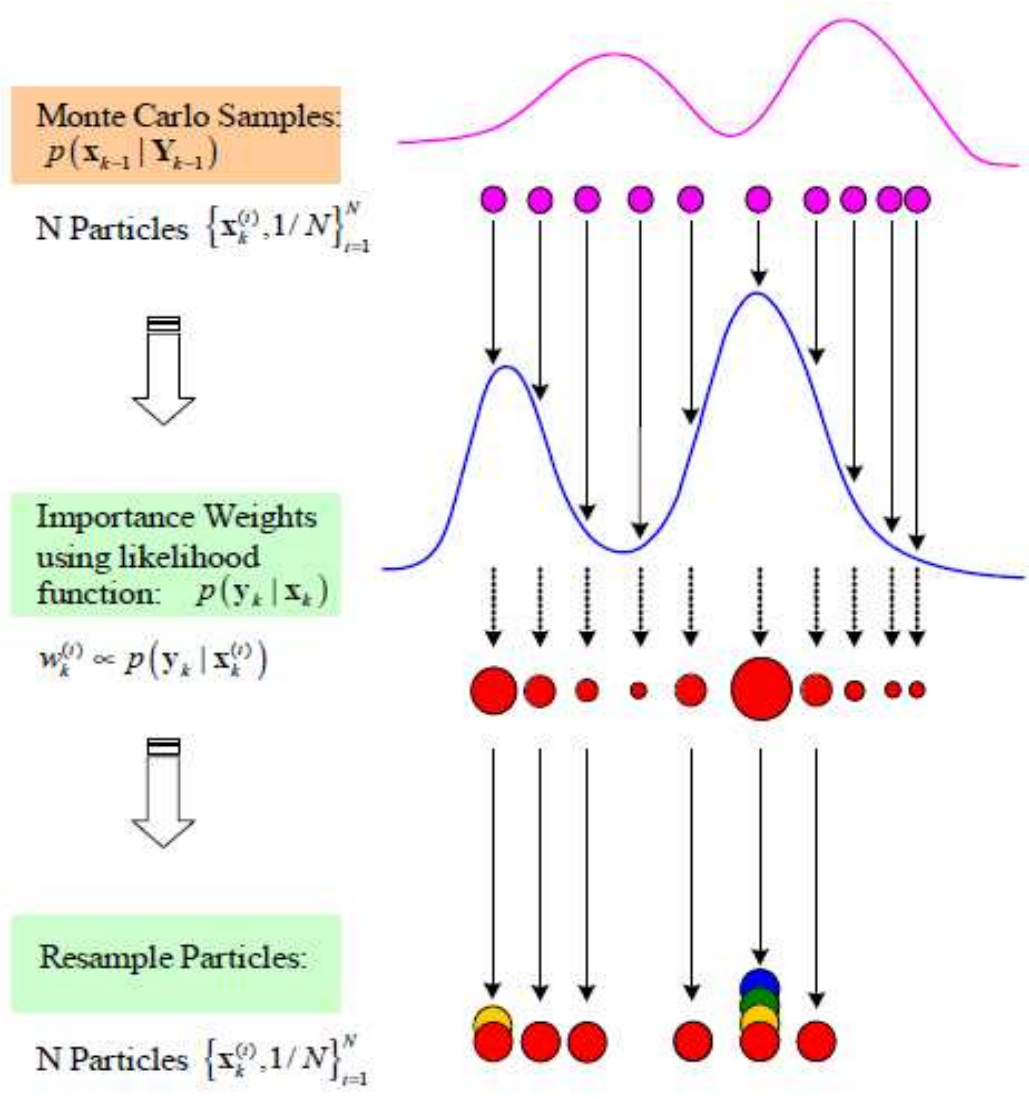


Figure 9 Schematic illustration of generic Particle filter(Lee, 2005)

3.4.3 Regularized Particle Filter

Although resampling reduces the impact of degeneracy phenomena, it causes another problem known as sample impoverishment. It originates from the fact that diversity among particles is lost as a result of the resampling in which samples with

Table 5 Generic Particle filter (Lee, 2005)

<p>➤ Initialization: at time $k=0$</p> <ol style="list-style-type: none"> 1. For $i = 1, \dots, N$ <ul style="list-style-type: none"> - Sampling from the prior $\mathbf{x}_0^{(i)} \sim p(\mathbf{x}_0)$ 2. For $i = 1, \dots, N$ <ul style="list-style-type: none"> - Calculate $w_0^{(i)} = p(\mathbf{y}_0 \mathbf{x}_0^{(i)})$ - Calculate the total weight $w_T = \sum_i^N w_0^{(i)}$ - Normalize $w_0^{(i)} = w_T^{-1} w_0^{(i)}$ <p>➤ Prediction and Update : for each time $k \geq 1$</p> <ol style="list-style-type: none"> 1. For $i = 1, \dots, N$ <ul style="list-style-type: none"> - Sample $\mathbf{x}_k^{(i)} \sim q(\mathbf{x}_k \mathbf{X}_{k-1}^{(i)}, \mathbf{Y}_k)$ - Calculate the importance weights $w_k^{(i)} = w_{k-1}^{(i)} \frac{p(\mathbf{y}_k \mathbf{x}_k^{(i)}) p(\mathbf{x}_k^{(i)} \mathbf{x}_{k-1}^{(i)})}{q(\mathbf{x}_k^{(i)} \mathbf{X}_{k-1}^{(i)}, \mathbf{Y}_k)}$. 2. Calculate the total weight $w_T = \sum_i^N w_k^{(i)}$ 3. For $i = 1, \dots, N$ <ul style="list-style-type: none"> - Normalize $w_k^{(i)} = w_T^{-1} w_k^{(i)}$ 4. If $(N_{eff} < N_{th})$ apply resampling
--

high weights are repeated many times. There modified algorithms of particle filter is used to handle this problem. One of these algorithms is Regularized Particle Filter (RPF)(Lee, 2005). In the RPF the resampling process is performed on the basis of density estimation.

In the resampling step, a new set of samples is generated form an approximate discrete representation of $p(\mathbf{x}_k | \mathbf{y}_{1:k})$. However, it is better to resample from a functional distribution by estimating the underlying density function. Generally,

density estimation methods are categorized in two classes; parametric and non-parametric. In parametric estimation methods, it is assumed that the distribution is a specific type of distribution such as Normal distribution. Non-parametric density estimation methods are used in situations that the distribution family is not known. For a scalar the general non-parametric density estimator is

$$\hat{p}(x) = \frac{1}{N} \sum_{i=1}^N w(x, x^i), \quad (3.55)$$

Where $w(x, x^i)$ is a weight function or kernel and x^i is the sample support value. Kernel is a weight function described in a closed functional form. The weight function generates a probability in the neighborhood of the support value. A rectangular box is the simple form of weight function

$$\hat{p}(x) = \frac{1}{Nh} \sum_{i=1}^N w\left(\frac{x - x^i}{h}\right), \quad (3.56)$$

and

$$w(\chi) = \begin{cases} 1/2 & \|\chi\| < 1 \\ 0 & \text{otherwise} \end{cases} \quad (3.57)$$

where h is the half of rectangle width. h determine the smoothing degree of the data. In all forms of kernel density estimation there is a tradeoff between resolution and smoothness.

It should be noted that it is better to select a smooth weight function for kernel estimation. The kernel density is a symmetric density function that must satisfy the conditions below

$$\int K(x)dx =, \int xK(x)dx = 0, \int \|x\|^2 K(x)dx < \infty \quad (3.58)$$

where $K(x)$ is candidate kernel. The candidate kernel is usually a Gaussian density which can be expressed as

$$\hat{p}(x) = \frac{1}{N\sigma} \sum K_G\left(\frac{x-x^i}{\sigma}\right), \quad (3.59)$$

and

$$K_G = \frac{1}{\sqrt{2\pi}} \exp\left\{-\frac{x^2}{2}\right\}, \quad (3.60)$$

where σ is the variance of Gaussian density function. The best kernel is the one that minimizes the integrated mean square errors. Because of that reason, the paraboloid or Epanechnikov kernel is the optimal one

$$K_E = \begin{cases} \frac{3}{4\sqrt{5}} \left(1 - \frac{x^2}{5}\right) & \|x\| \leq \sqrt{5} \\ 0 & otherwise \end{cases} \quad (3.61)$$

The other important factor in the kernel estimation is the selection of bandwidth which measures a level of smoothness. For the Gaussian kernel a good choice is

$$\sigma_{opt} = \frac{1}{N^{1/5}} \sqrt{\Sigma}, \quad (3.62)$$

where Σ is the variance of the sample data.

The convolution calculation is needed for density estimation by using kernel method. It makes the method difficult and an acceptable approximation technique is

required. One of the potential solutions is demonstrating the data with a set of data support value $\{x^i\}_{i=1}^N$ and by introducing a new set of support values $\{\chi^j\}_{j=1}^M$ for the underlying density estimate. So, the kernel is assessed for all pairwise combinations of the data sets and estimate support values

$$\hat{p}(\chi^j) = \frac{1}{N} \sum_{i=1}^N K(\chi^j, x^i), \quad j=1, \dots, M \quad (3.63)$$

The RPF perform resampling based on the continuous approximation of the probability density $p(\mathbf{x}_k | \mathbf{y}_{1:k})$. It is obtained through the kernel density estimation method.

$$p(\mathbf{x}_k | \mathbf{y}_{1:k}) \approx \hat{p}(\mathbf{x}_k | \mathbf{y}_{1:k}) = \sum_{i=1}^N w_k^i K_h(\mathbf{x}_k - \mathbf{x}_k^i), \quad (3.64)$$

and

$$K_h(\mathbf{x}) = \frac{1}{h^{n_x}} K\left(\frac{\mathbf{x}}{h}\right) \quad (3.65)$$

Where

K_h : rescaled Kernel density,

$h > 0$: kernel bandwidth,

n_x : dimension of the state vector,

w_k^i : normalized weight.

The multivariate Gaussian Kernel is expressed as

$$K(\mathbf{x}) = \frac{1}{(2\pi)^{n_x/2}} \exp\left\{-\frac{1}{2} \mathbf{x}^T \mathbf{x}\right\} \quad (3.66)$$

As it is mentioned above, the kernel and band width are chosen in a way that minimizes the Mean Integrated Square Error (MISE) between the posterior density and the corresponding estimated density that can be written in the form of

$$MISE = \left\{ \int [\hat{p}(\mathbf{x}_k | \mathbf{y}_{1:k}) - p(\mathbf{x}_k | \mathbf{y}_{1:k})]^2 d\mathbf{x}_k \right\} \quad (3.67)$$

The associated Epanechnikov Kernel as the optimal kernel is expressed as follow

$$K_E = \begin{cases} \frac{n_x + 2}{C_{n_x}} (1 - \mathbf{x}^T \mathbf{x}) & \|\mathbf{x}\| < 1 \\ 0 & otherwise \end{cases} \quad (3.68)$$

where C_{n_x} is the volume of the unit n_x -dimensional sphere. Before smoothing with a symmetric kernel, the data should be prewhitened by transforming it to have unit variance. Density estimate in the form of equation 3.69 is used for this purpose.

$$\hat{p}(\mathbf{x}) = \frac{1}{Nh^{n_x} |\mathbf{S}|^{-1/2}} \sum_{i=1}^N \left(\frac{[\mathbf{x} - \mathbf{x}^i]^T \mathbf{S}^{-1} [\mathbf{x} - \mathbf{x}^i]}{h^2} \right) \quad (3.69)$$

where the \mathbf{S} is empirical covariance matrix. The optimal bandwidth for multivariate Gaussian Kernel is given by

$$h_{opt} = \left[\frac{4}{N(2n_x + 1)} \right]^{1/(n_x + 4)} \quad (3.70)$$

The optimal bandwidth for the Epanechnikov Kernel is obtained as follow

$$h_{opt} = \left[\frac{8n_x(n_x + 2)(n_x + 4)(2\sqrt{\pi})^{n_x}}{N(2n_x + 1)c_{n_x}} \right]^{1/(n_x + 4)} \quad (3.71)$$

The algorithm of the RPF is described in table 6.

Table 6 Regularized Particle filter (Lee, 2005)

<p>➤ Initialization : At time $k = 0$</p> <ul style="list-style-type: none"> - For $i = 1, \dots, N$ - Sampling from the prior $\mathbf{x}_0^{(i)} \sim p(\mathbf{x}_0)$ - For $i = 1, \dots, N$ - Calculate $w_0^{(i)} = p(\mathbf{y}_0 \mathbf{x}_0^{(i)})$ - Calculate the total weight $w_T = \sum_i^N w_0^{(i)}$ - Normalize $w_0^{(i)} = w_T^{-1} w_0^{(i)}$ <p>➤ Prediction and Update : for each time $k \geq 1$ same as generic PF (Table 5)</p> <ol style="list-style-type: none"> 1. Calculate the effective sample size 2. If ($N_{eff} < N_{th}$) <ul style="list-style-type: none"> - Calculate the empirical covariance \mathbf{S}_k of $\{\mathbf{x}_k^i, w_k^i\}_{i=1}^N$ - Compute \mathbf{D}_k such in way $\mathbf{D}_k \mathbf{D}_k^T = \mathbf{S}_k$ - Apply resampling algorithm - For $i = 1, \dots, N$ <ul style="list-style-type: none"> • Draw $\xi^i \sim K$ from the Epanechnikov kernel • $\mathbf{x}_k^i = \mathbf{x}_k^i + h_{opt} \mathbf{D}_k \xi^i$
--

CHAPTER 4

Implementation and Application

4.1 Data Set

The GPS data of 29 ground based GPS stations, belonging to IGS⁶ and EUREF⁷, for Europe have been used in this study. The data acquisition time is 18 February 2011 and the data is affected by the 15 February geomagnetic storm. The storm is started to show its impact from 3:00 am of the 18 February and peaked at 12:00 am. Then, eventually it decreases its effect at the rest of the day (Kane, 2011). The data is provided in RINEX format and with 30 second intervals. The GPS stations that have been used in this work are specified in Figure 10 by blue color points and their name as a list is provided in Table 7.

Table 7 Stations

axpv	badh	bpdl	bute	bydg	clib	cpar	crei	crak	ctab
delf	dent	eijs	eusk	gwwl	hobu	hoe2	igeo	lodz	man2
mlvl	redz	smne	swki	Ters	tlmf	vfch	ware	zywi	

⁶ International GNSS Service

⁷ Reference Frame Sub-commission for Europe

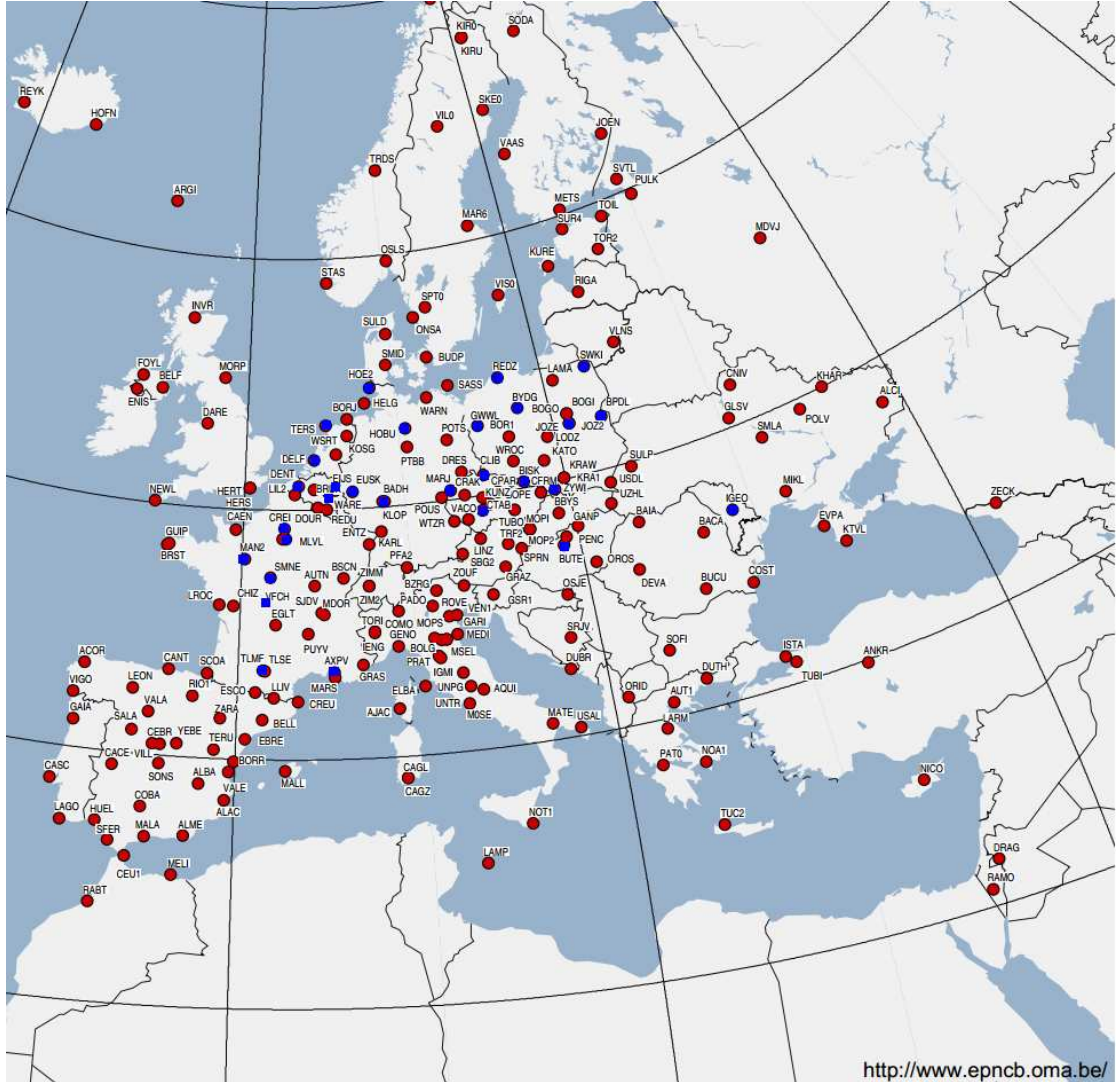


Figure 10 Stations used in this study are the blue ones

4.2 Preprocessing

The TECmapper Software has been used for preprocessing step. The observation files and related precise orbit and DCB files has been downloaded from the IGS website (<http://igsceb.jpl.nasa.gov/>). Then they were imported to the software for executing preprocessing tasks.

The procedure in the software can be described as follow (Figure 11). At first, the receiver type, approximate position of the receiver, types of available observables and time for the initial observation are read form the header. After that, all pseudorange and carrier phase observations are extracted and grouped based on the satellite number. Next the satellite coordinates for each epoch are determined using precise orbit file and Lagrange’s formula. Azimuth and zenith angel of the satellites are obtained by the satellite and receiver coordinates. Then the observations of each satellite are examined for any possible cycle slip and continuous observation arcs are formed. After that, geometry-free linear combinations of the observables are calculated for each continuous arc. Pseudorange observations smoothed with the carrier to code leveling method. Then, pseudorange ionospheric observables are corrected with satellite DCBs. These observations and other information such as azimuth and zenith angels are saved in the output file.

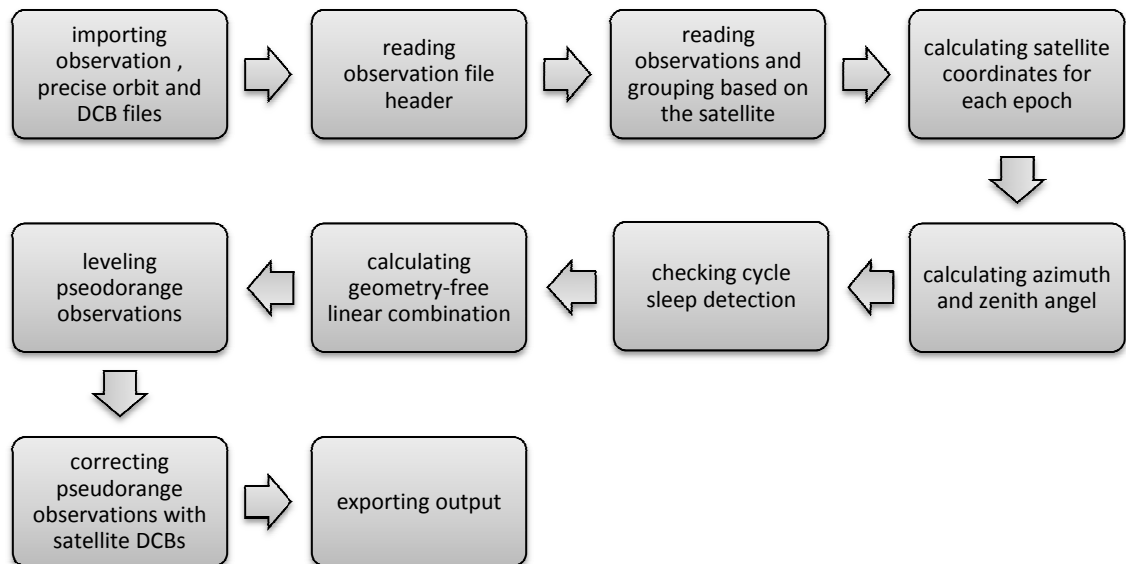


Figure 11 the preprocessing steps

4.3 Ionosphere Modeling

The quantity that has been modeled in this work is VTEC and it can be derived from the methodology described in the section 2.3. For both filters the observation model is equation 2.35 that can be re-written in the following form

$$(\tilde{P}_4 - bs) \frac{\gamma}{F(z)} = VTEC + br \frac{\gamma}{F(z)} + \varepsilon. \quad (4.1)$$

The left hand side of the equation contains the observations; carrier phase smoothed pseudorange and satellite bias. The parameters that should be estimated are at the left side of the equation; VTEC and receiver bias.

The parameters are assumed to vary stochastically in time so the first order Gauss-Markov process is adopted as the dynamical model.

$$\mathbf{x}_{k+1} = e^{-\beta(\Delta t)} \mathbf{x}_k + w, \quad (4.2)$$

where

\mathbf{x}_{k+1} : parameter vector containing VTEC and receiver bias

$\frac{1}{\beta}$: correlation time

w : process noise

Δt : time interval.

In equation 4.2 the temporal correlation of the parameters is illustrated with the normalized autocorrelation function $e^{-\beta(\Delta t)}$ and the remaining uncorrelated part is assumed to be the white noise. The process noise of the white noise can be obtained by

$$q_k = \sigma^2(1 - e^{-2\beta\Delta t}), \quad (4.3)$$

where σ^2 is the spectral density divided by 2β . The correlation time is set 1/30 minute and σ^2 value is set as 0.5 for VTEC and 0.05 for receiver bias (El Gizawy, 2003).

4.3.1 Filters Application

Form the information provided in the previous section, the measurement model can be written as below

$$\mathbf{y}_k = \mathbf{h}(\mathbf{x}_k, k) + \mathbf{v}_k. \quad (4.4)$$

For each epoch

$$\mathbf{y} = \begin{bmatrix} (\tilde{P}_4 - bs)_{sat1} \\ (\tilde{P}_4 - bs)_{sat2} \\ \vdots \\ (\tilde{P}_4 - bs)_{satN} \end{bmatrix}_{N \times 1}, \mathbf{h} = \begin{bmatrix} \frac{F_1(z)}{\gamma} & 1 \\ \gamma & \\ \vdots & \\ \frac{F_N(z)}{\gamma} & 1 \\ \gamma & \end{bmatrix}_{N \times 1}, \mathbf{x} = \begin{bmatrix} VTEC \\ br \end{bmatrix}_{2 \times 1}$$

where N is the number of satellites in the corresponding epoch. For the system model, as it was mentioned in the previous chapter

$$\mathbf{x}_k = \mathbf{f}(\mathbf{x}_{k-1}, k-1) + \mathbf{w}_{k-1}, \quad (4.5)$$

$$\mathbf{x} = \begin{bmatrix} VTEC \\ br \end{bmatrix}, \mathbf{f} = \begin{bmatrix} e^{-\beta(\Delta t)} \\ e^{-\beta(\Delta t)} \end{bmatrix} \quad (4.6)$$

The algorithms of the filters illustrated in the previous chapter. Additionally outlier detection procedure has been performed before the update step. A hard thresholding method has been adopted for detecting outlier observations. The threshold is selected as 3 times standard deviation of the measurements. Also it should be mentioned that the Particle number in the Particle filter is 500 for each epoch.

4.4 Results and Evaluations

The both filters have been used for VTEC estimation in the all 29 stations. It can be easily seen during the time span where geomagnetic storm has not been started, both filters give close results. However, by beginning of the storm, the variations in the VTEC signal amplitude become critical and the Kalman filter cannot show enough adaptation to it. On the other hand, the Particle filter follows this variation better than Kalman filter. The visual and numerical results prove the mentioned judgements.

For accuracy assessment the post-fit residual has been used in this study. Post-fit residual is the difference between the measured and the estimated value. In order to make the comparison feasible the estimated receiver bias has been combined to the ionospheric pseudorange measurements. The results have been provided in figures 12 to 40 for all of the stations. In each figure the first panel depicts the observation VTEC arcs and also the estimated VTEC by both filters. The observation VTEC arcs have been color coded for different satellites. The Kalman filter estimation has been shown by thick dotted black lines and Particle filter results have been presented in thick continuous black lines. The second and third panels depict the post-fit residuals. Smaller post-fit residuals can be an indicator of more accurate results. For comparing the results of filters, the post-fit variance in each epoch has been drawn

for both filters in the fourth panel. The red one is indicator of Particle filter and the blue one shows the Kalman filter. Also for the numeric comparison, the Root Mean Square Error (RMSE) has been computed for each filter in all of the stations and the results can be found in Table 8. It is evident that the Particle filter has a better performance in all stations because of smaller RSME.

Table 8 RMSE of the results in each station

Station	Particle filter RMSE	Kalman Filter RMSE	Station	Particle filter RMSE	Kalman Filter RMSE
axpv	2.2388	2.7181	hobu	3.2644	3.4069
badh	2.9317	3.1960	hoe2	3.4423	3.5422
bpd1	3.0793	3.3000	igeo	2.1126	2.4754
bute	2.491	2.8074	lodz	3.0919	3.3129
bydg	3.2050	3.4500	man2	2.6864	3.0198
clib	2.5300	2.9033	mlvl	2.6658	3.0119
cpar	2.6690	2.9521	redz	3.4115	3.5907
crak	2.5878	2.9095	smne	2.6617	3.0258
crei	2.7010	3.0333	swki	3.1055	3.2818
ctab	2.5899	2.9044	ters	3.3953	3.4963
delf	3.1703	3.3912	tlmf	2.3135	2.7724
dent	3.0205	3.2129	vfch	2.4350	2.9078
eijs	3.1054	3.2914	ware	3.2072	3.3521
eusk	2.9045	3.1928	zywi	2.8266	3.2593
gwwl	3.2779	3.4595			

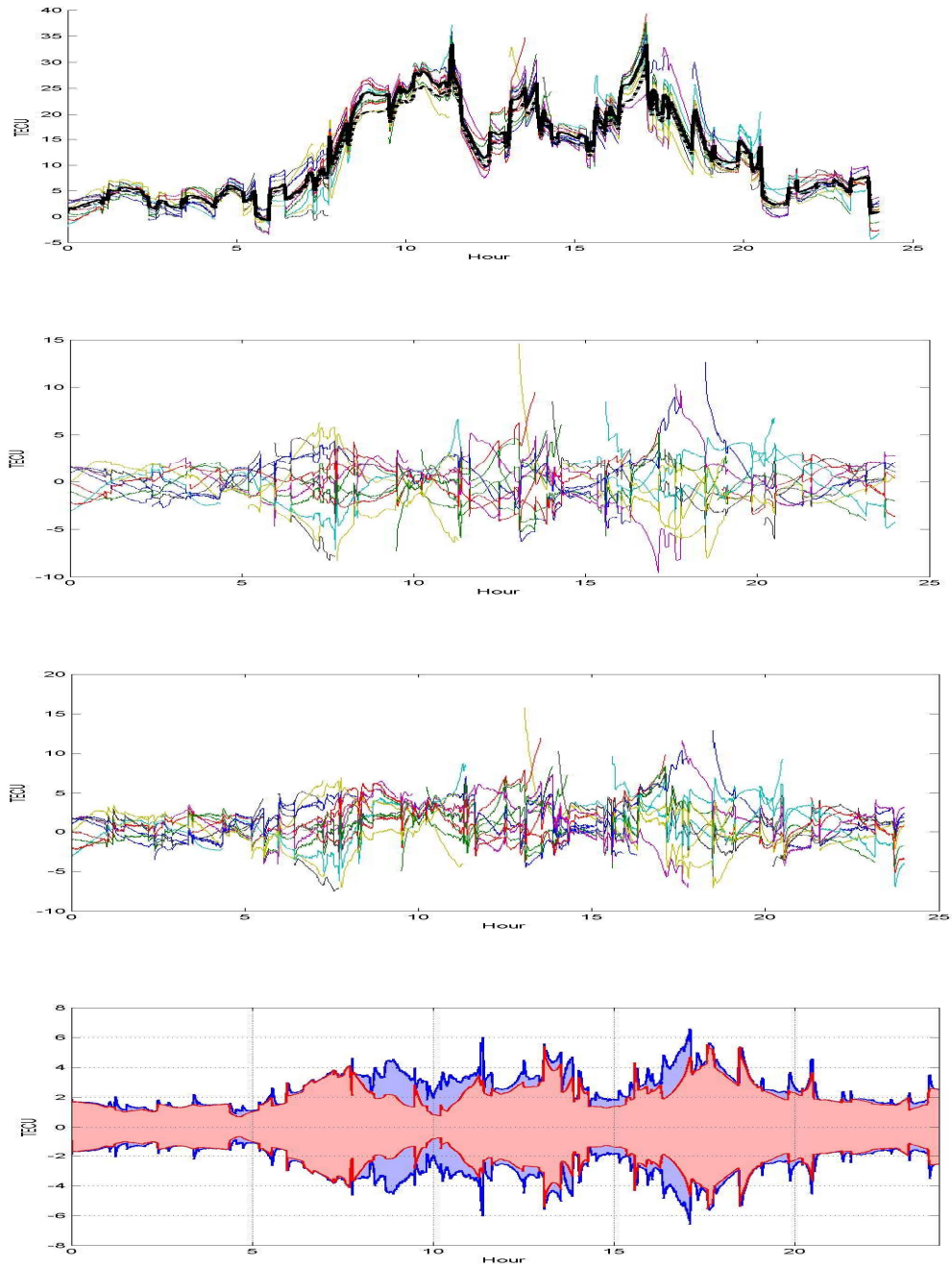


Figure 12 axpv station results. First panel illustrates observations and the performance of the filters for estimating VTEC. Different satellites observations color coded. Solid thick line is for particle filter and dashed thick line is for Kalman filter. The second and third panels show the post fit residuals of the Particle filter and the Kalman filters estimations, respectively. The fourth panel depicts the post fit standard deviation for each epoch in which the blue one is for the Kalman filter and the red one is for the particle.

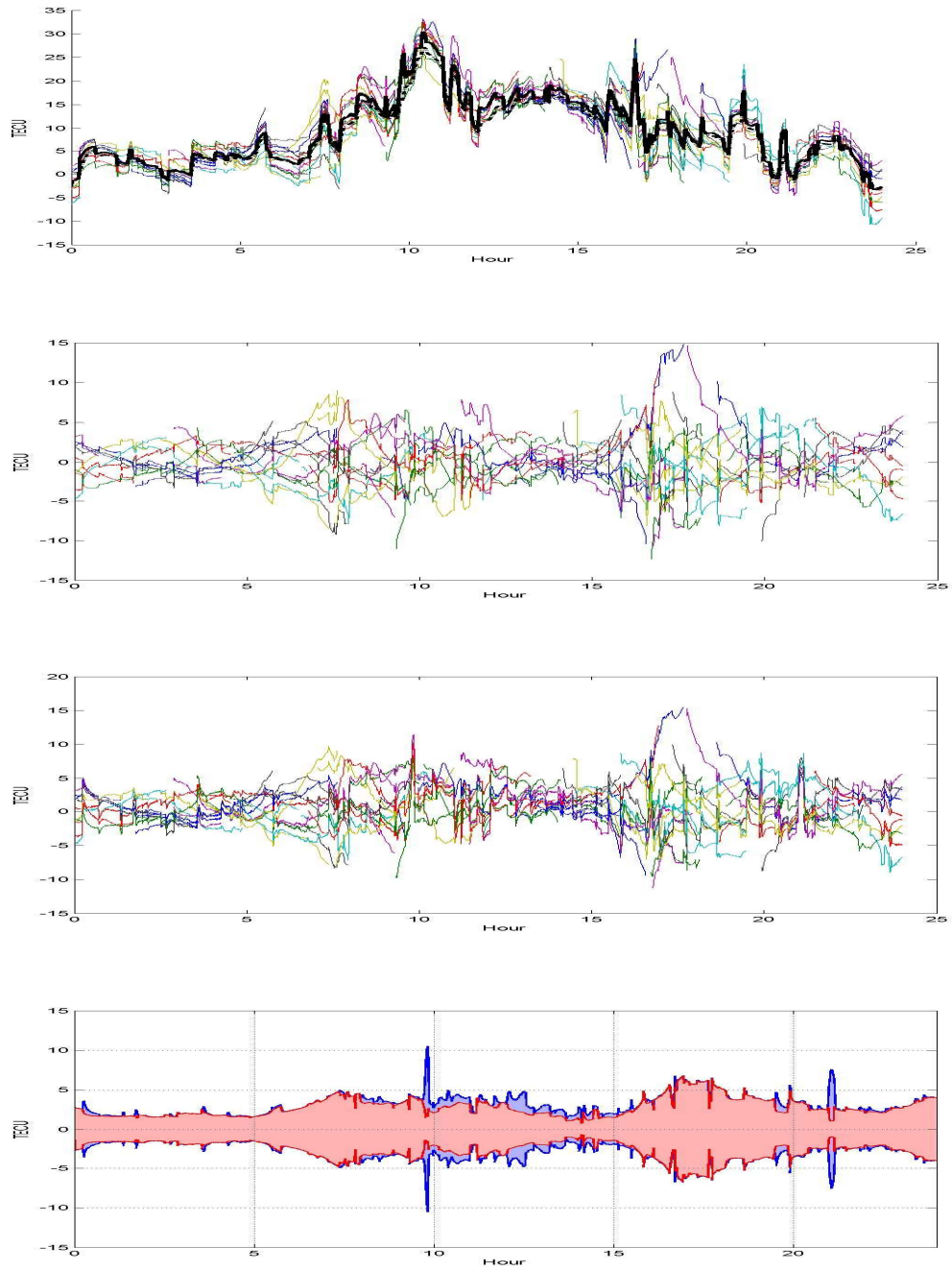


Figure 13 badh station results. First panel illustrates observations and the performance of the filters for estimating VTEC. Different satellites observations color coded. Solid thick line is for particle filter and dashed thick line is for Kalman filter. The second and third panels show the post fit residuals of the Particle filter and the Kalman filters estimations, respectively. The fourth panel depicts the post fit standard deviation for each epoch in which the blue one is for the Kalman filter and the red one is for the particle.

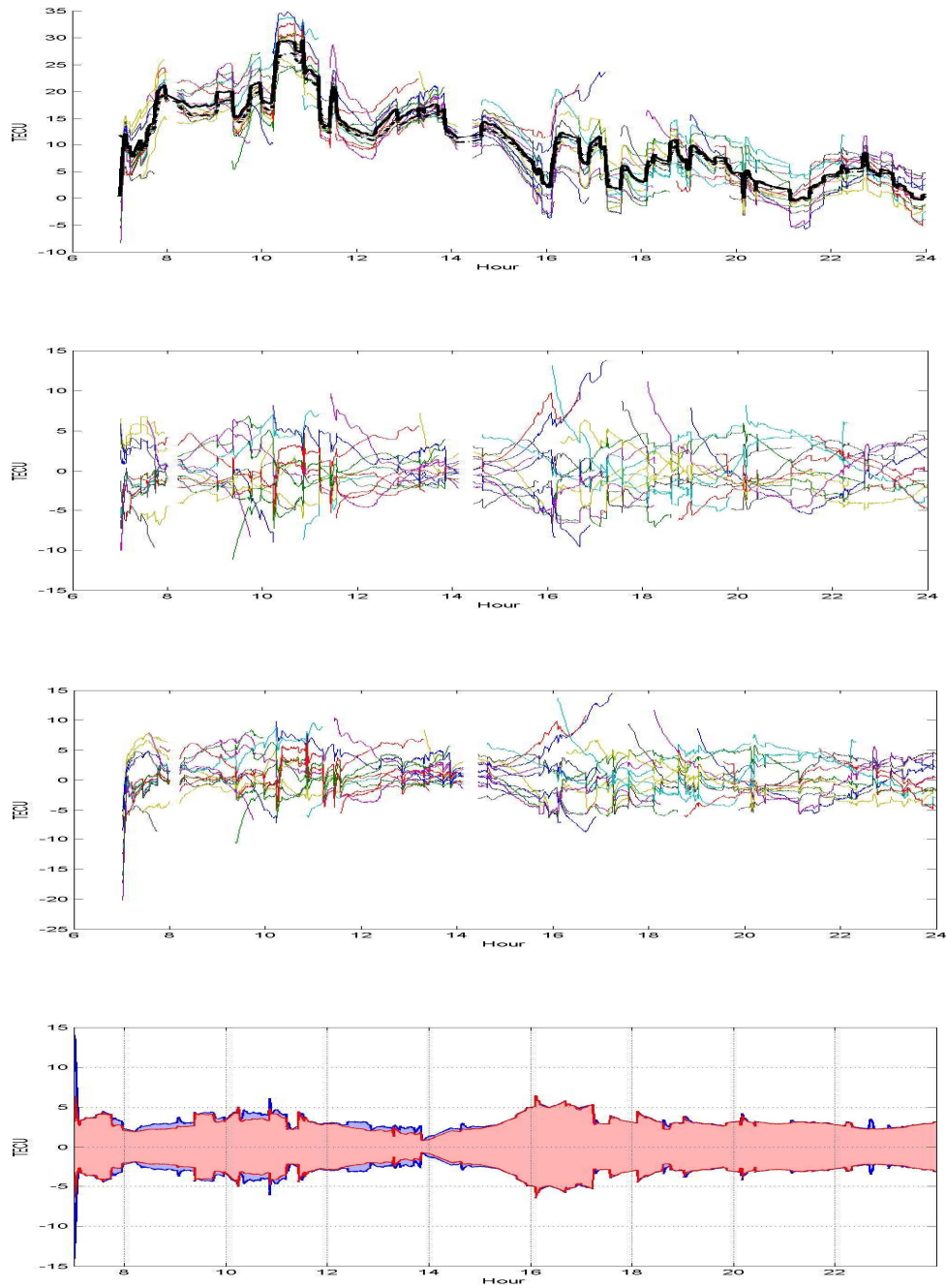


Figure 14 bpd1 station results. First panel illustrates observations and the performance of the filters for estimating VTEC. Different satellites observations color coded. Solid thick line is for particle filter and dashed thick line is for Kalman filter. The second and third panels show the post fit residuals of the Particle filter and the Kalman filters estimations, respectively. The fourth panel depicts the post fit standard deviation for each epoch in which the blue one is for the Kalman filter and the red one is for the particle.

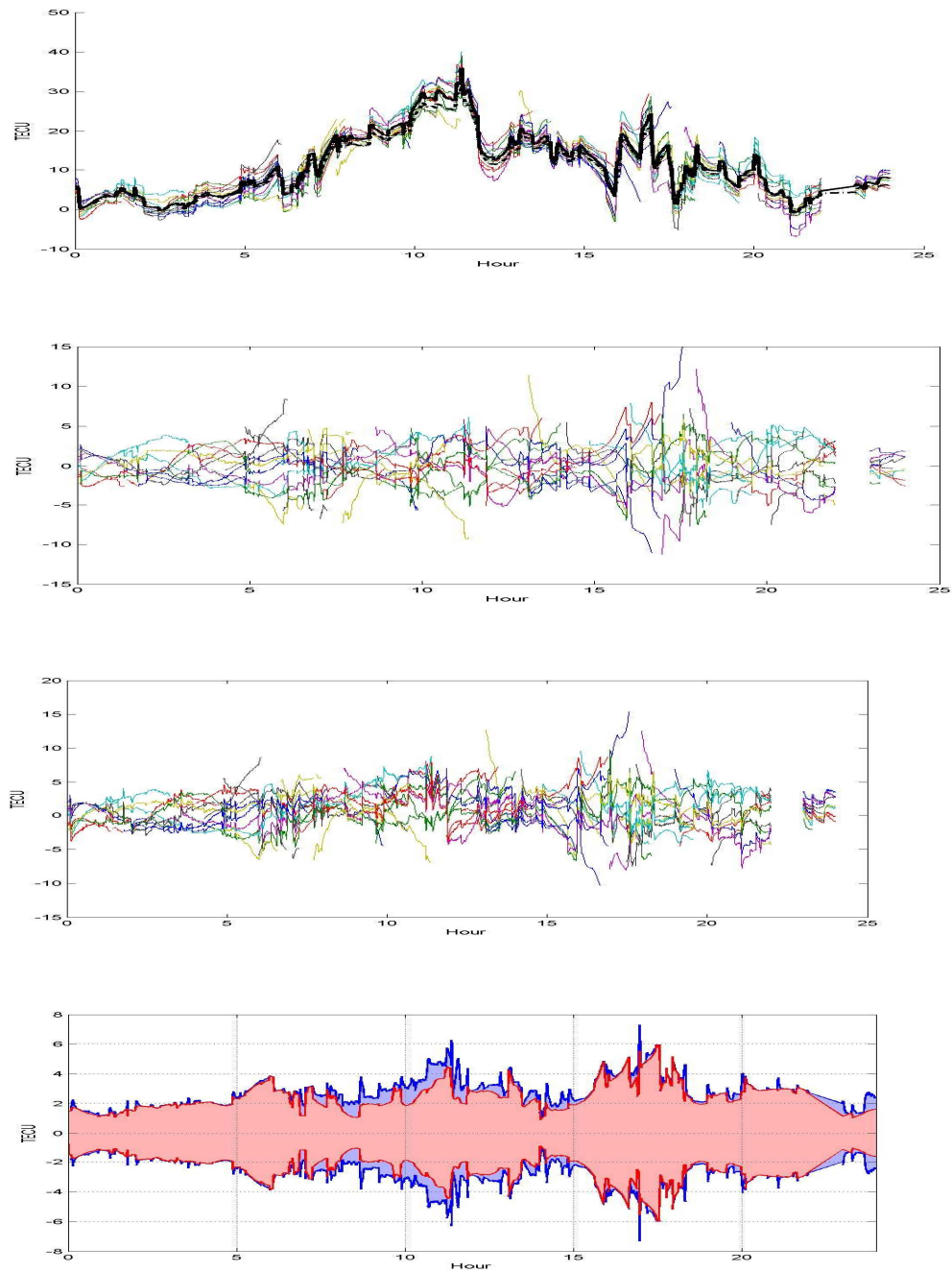


Figure 15 bute station results. First panel illustrates observations and the performance of the filters for estimating VTEC. Different satellites observations color coded. Solid thick line is for particle filter and dashed thick line is for Kalman filter. The second and third panels show the post fit residuals of the Particle filter and the Kalman filters estimations, respectively. The fourth panel depicts the post fit standard deviation for each epoch in which the blue one is for the Kalman filter and the red one is for the particle.

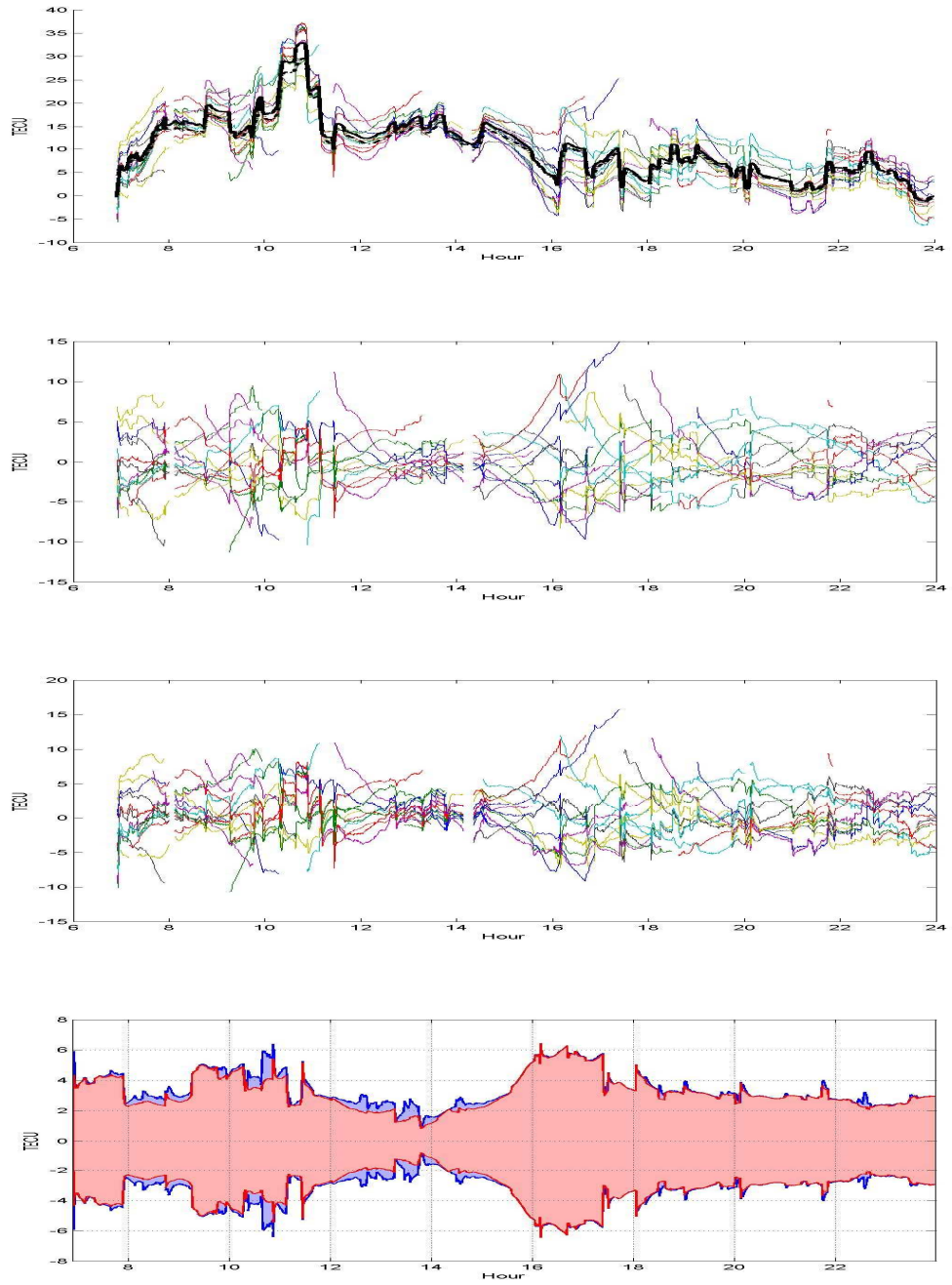


Figure 16 bydg station results. First panel illustrates observations and the performance of the filters for estimating VTEC. Different satellites observations color coded. Solid thick line is for particle filter and dashed thick line is for Kalman filter. The second and third panels show the post fit residuals of the Particle filter and the Kalman filters estimations, respectively. The fourth panel depicts the post fit standard deviation for each epoch in which the blue one is for the Kalman filter and the red one is for the particle.

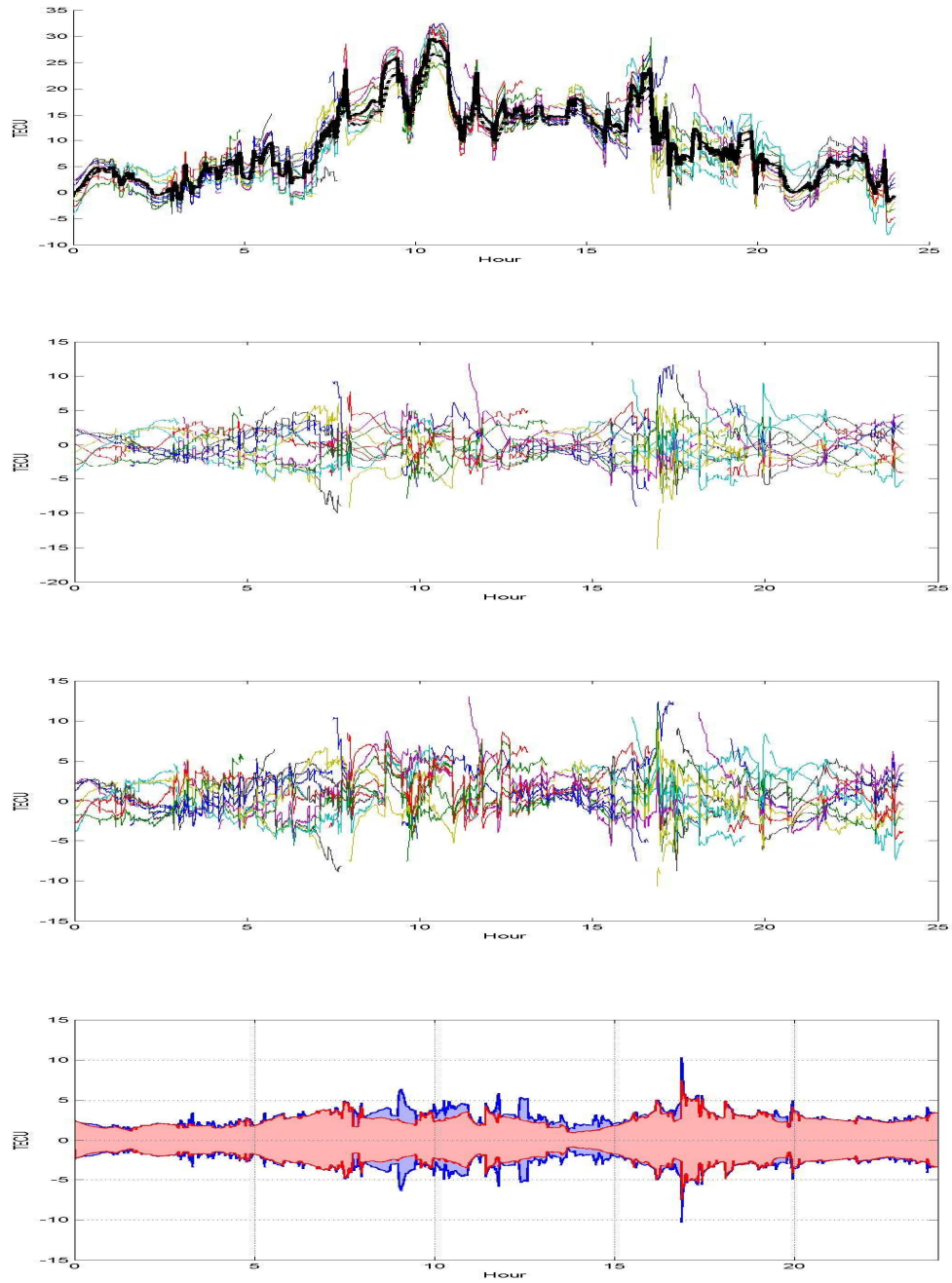


Figure 17 clib station results. First panel illustrates observations and the performance of the filters for estimating VTEC. Different satellites observations color coded. Solid thick line is for particle filter and dashed thick line is for Kalman filter. The second and third panels show the post fit residuals of the Particle filter and the Kalman filters estimations, respectively. The fourth panel depicts the post fit standard deviation for each epoch in which the blue one is for the Kalman filter and the red one is for the particle.

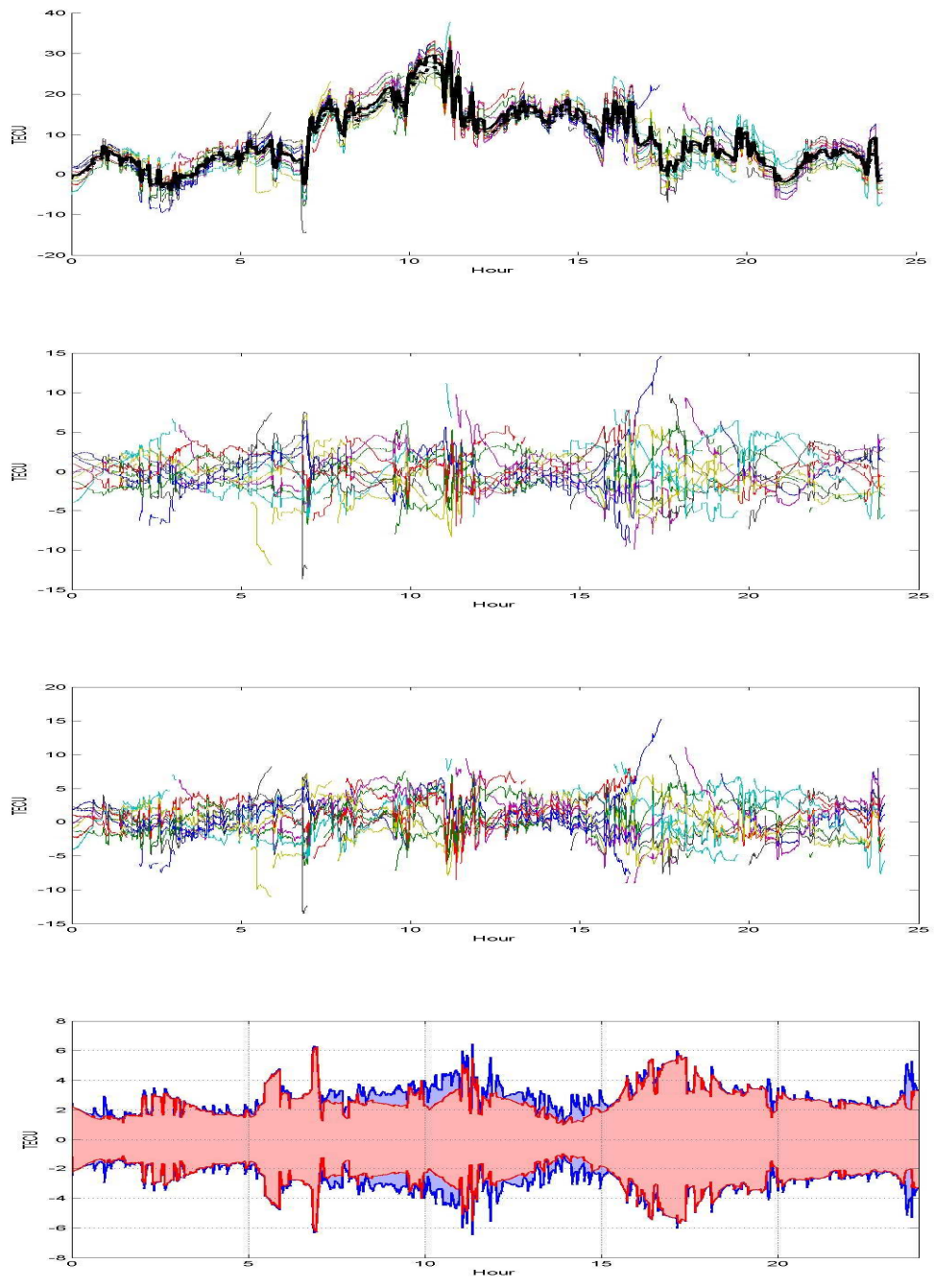


Figure 18 cpar station results. First panel illustrates observations and the performance of the filters for estimating VTEC. Different satellites observations color coded. Solid thick line is for particle filter and dashed thick line is for Kalman filter. The second and third panels show the post fit residuals of the Particle filter and the Kalman filters estimations, respectively. The fourth panel depicts the post fit standard deviation for each epoch in which the blue one is for the Kalman filter and the red one is for the particle.

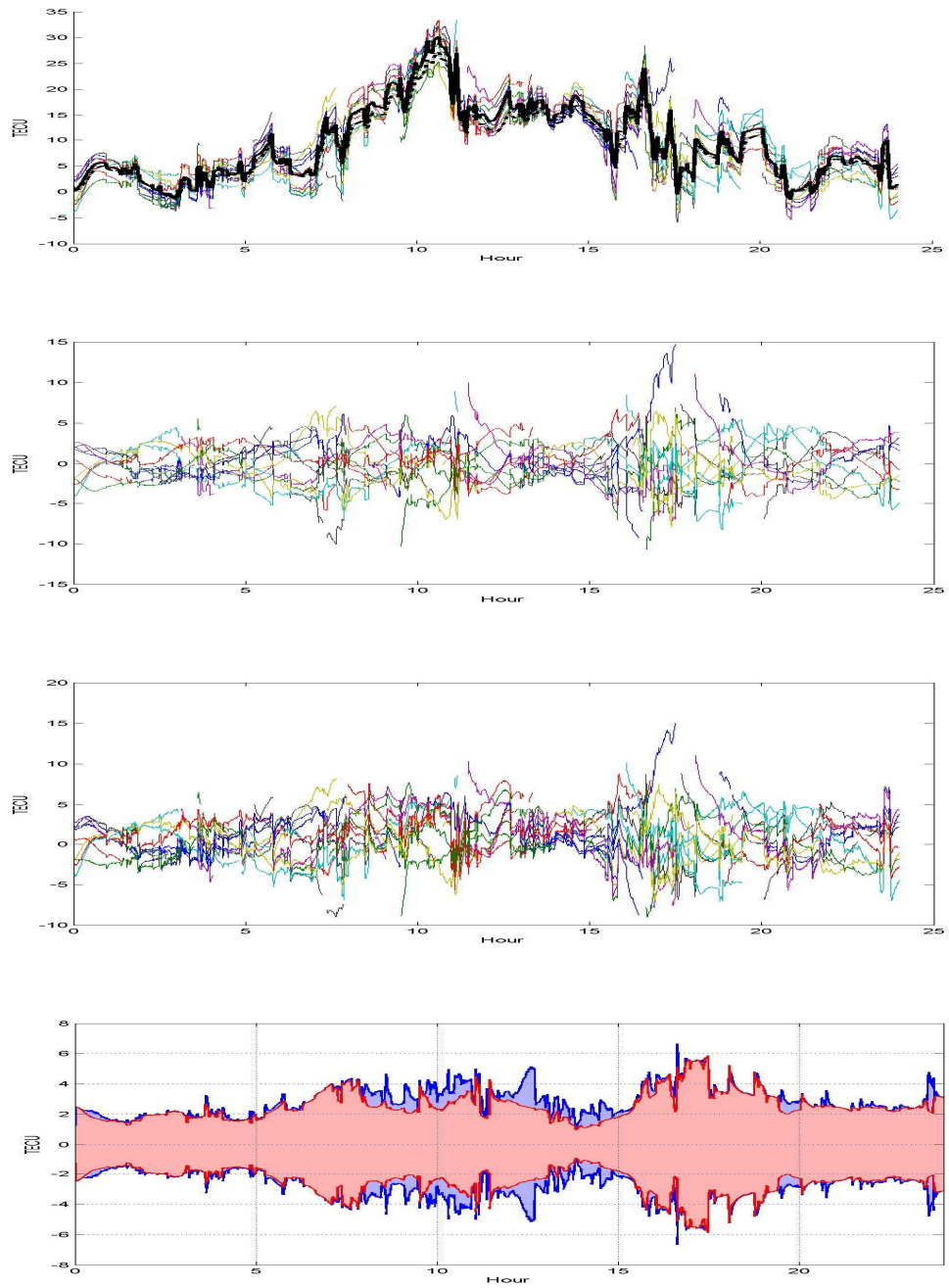


Figure 19 crack station results. First panel illustrates observations and the performance of the filters for estimating VTEC. Different satellites observations color coded. Solid thick line is for particle filter and dashed thick line is for Kalman filter. The second and third panels show the post fit residuals of the Particle filter and the Kalman filters estimations, respectively. The fourth panel depicts the post fit standard deviation for each epoch in which the blue one is for the Kalman filter and the red one is for the particle.

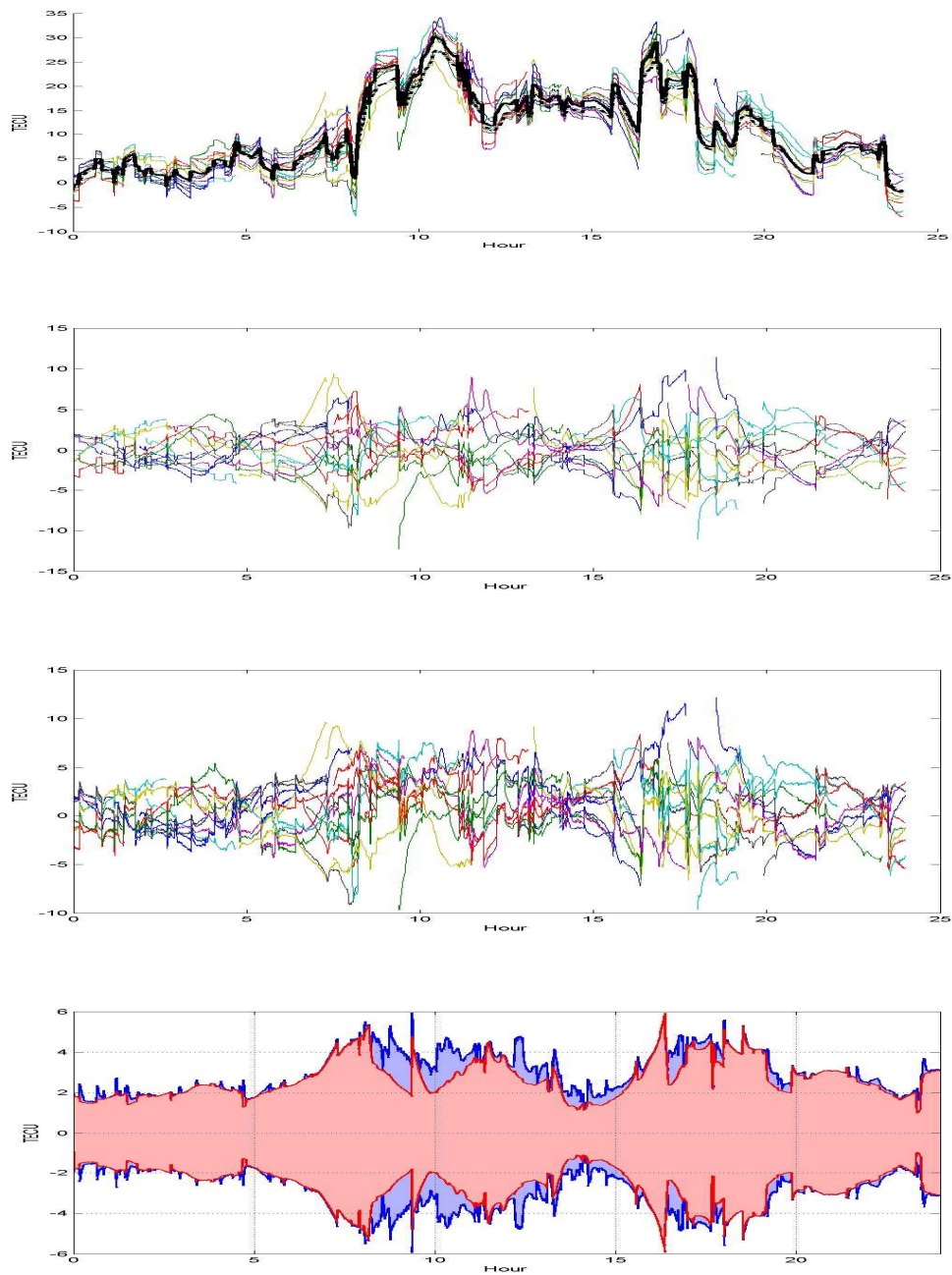


Figure 20 crei station results. First panel illustrates observations and the performance of the filters for estimating VTEC. Different satellites observations color coded. Solid thick line is for particle filter and dashed thick line is for Kalman filter. The second and third panels show the post fit residuals of the Particle filter and the Kalman filters estimations, respectively. The fourth panel depicts the post fit standard deviation for each epoch in which the blue one is for the Kalman filter and the red one is for the particle.

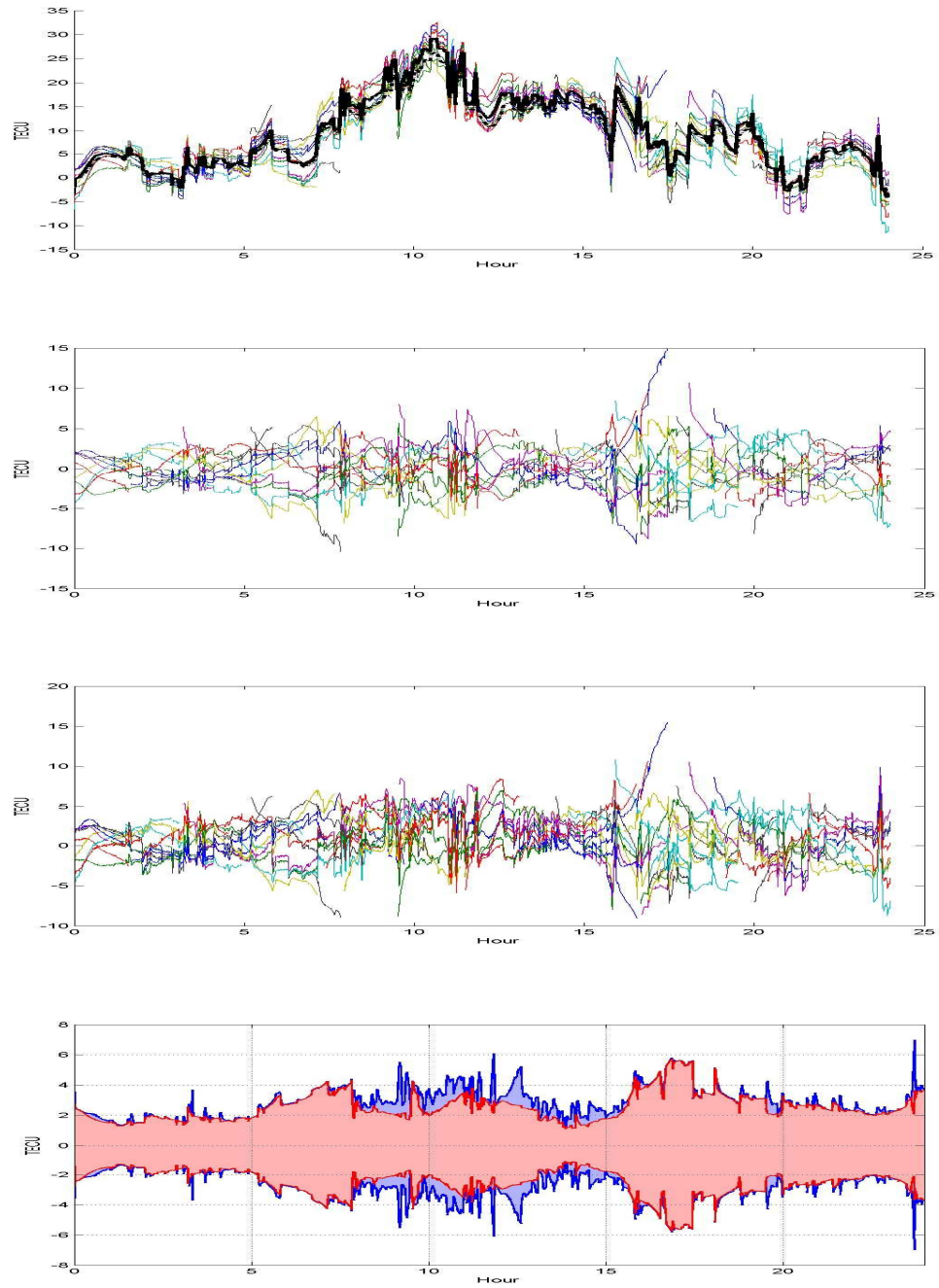


Figure 21 ctav station results. First panel illustrates observations and the performance of the filters for estimating VTEC. Different satellites observations color coded. Solid thick line is for particle filter and dashed thick line is for Kalman filter. The second and third panels show the post fit residuals of the Particle filter and the Kalman filters estimations, respectively. The fourth panel depicts the post fit standard deviation for each epoch in which the blue one is for the Kalman filter and the red one is for the particle.

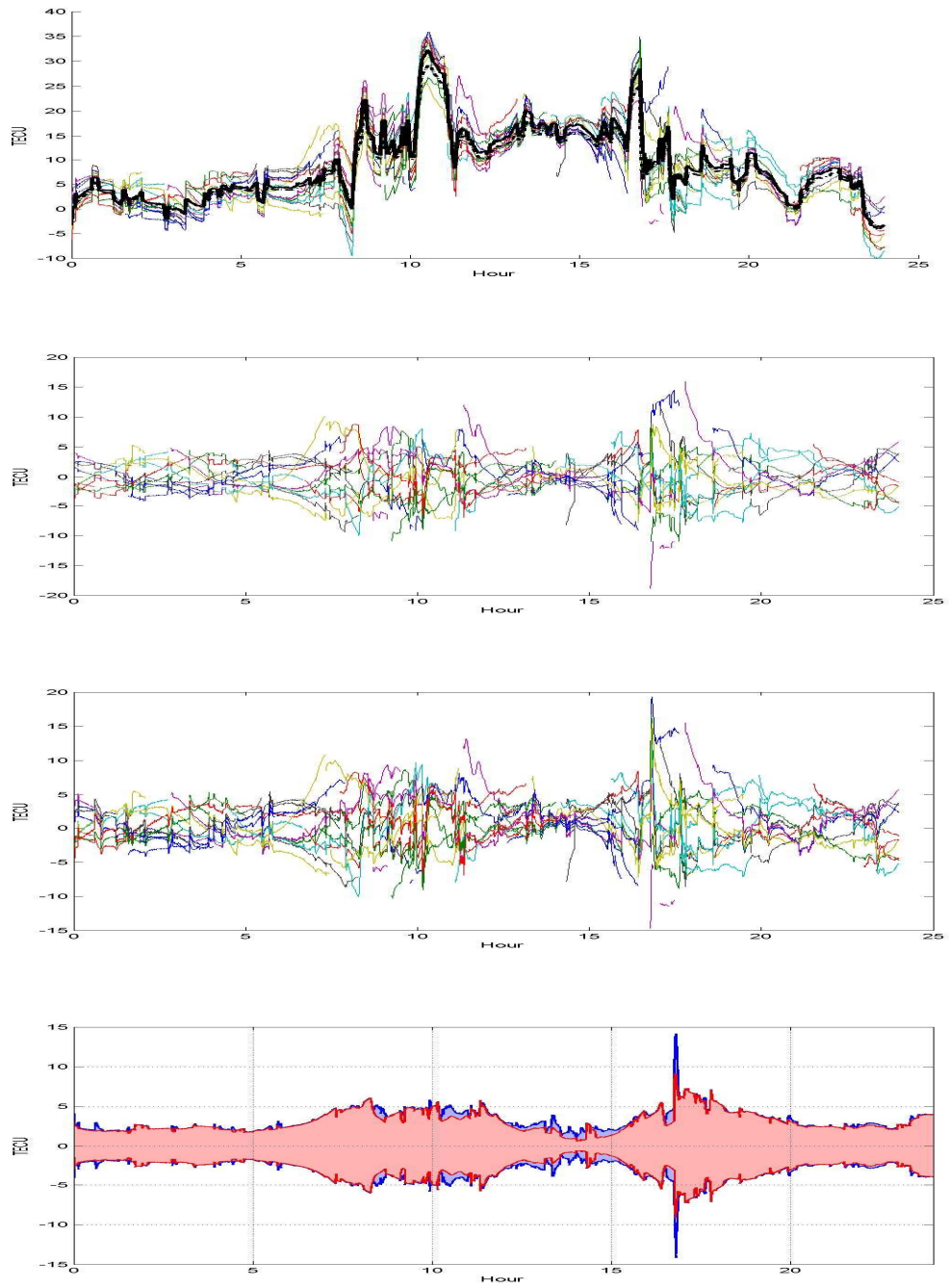


Figure 22 delf station results. First panel illustrates observations and the performance of the filters for estimating VTEC. Different satellites observations color coded. Solid thick line is for particle filter and dashed thick line is for Kalman filter. The second and third panels show the post fit residuals of the Particle filter and the Kalman filters estimations, respectively. The fourth panel depicts the post fit standard deviation for each epoch in which the blue one is for the Kalman filter and the red one is for the particle.

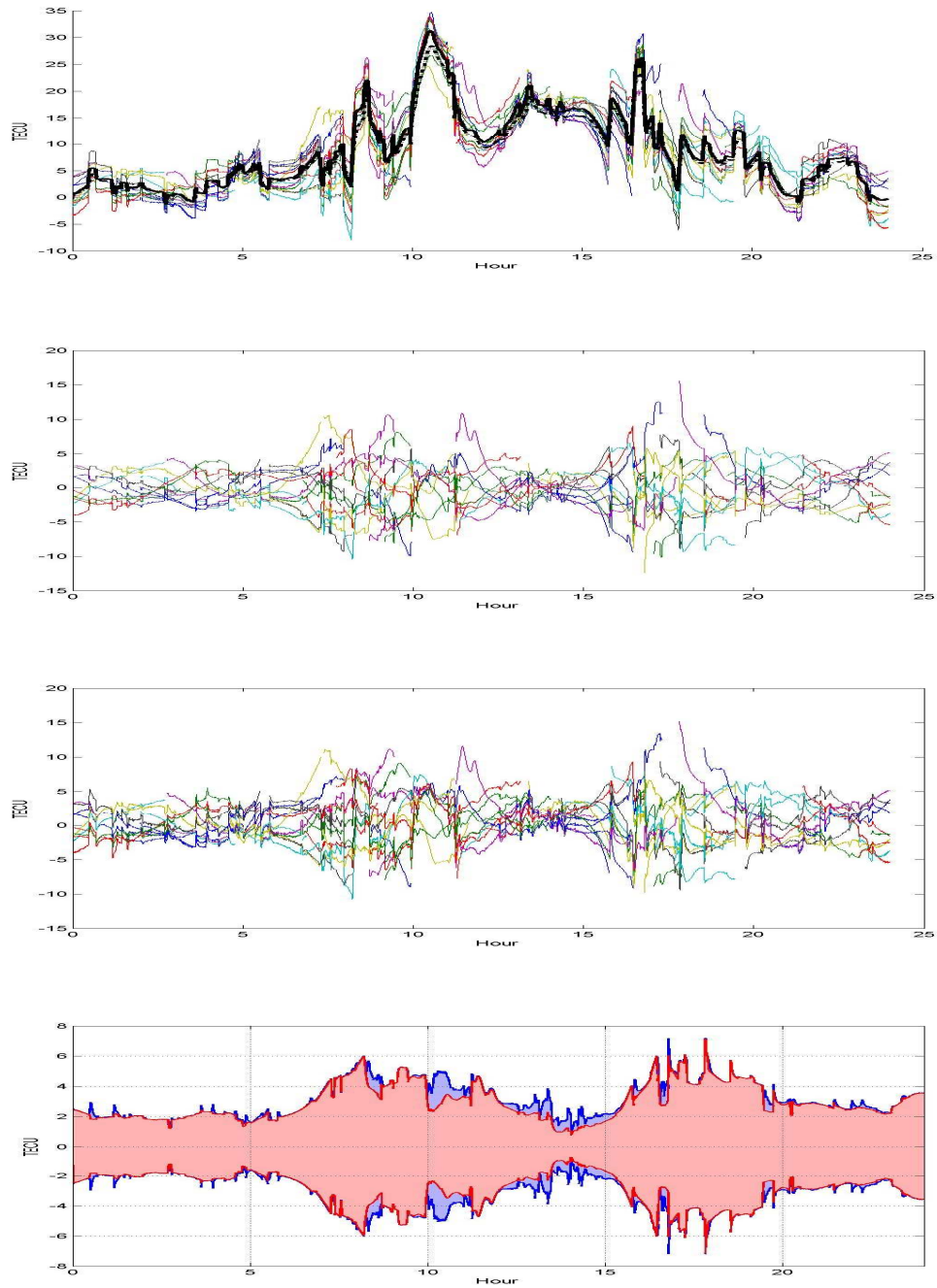


Figure 23 dent station results. First panel illustrates observations and the performance of the filters for estimating VTEC. Different satellites observations color coded. Solid thick line is for particle filter and dashed thick line is for Kalman filter. The second and third panels show the post fit residuals of the Particle filter and the Kalman filters estimations, respectively. The fourth panel depicts the post fit standard deviation for each epoch in which the blue one is for the Kalman filter and the red one is for the particle.

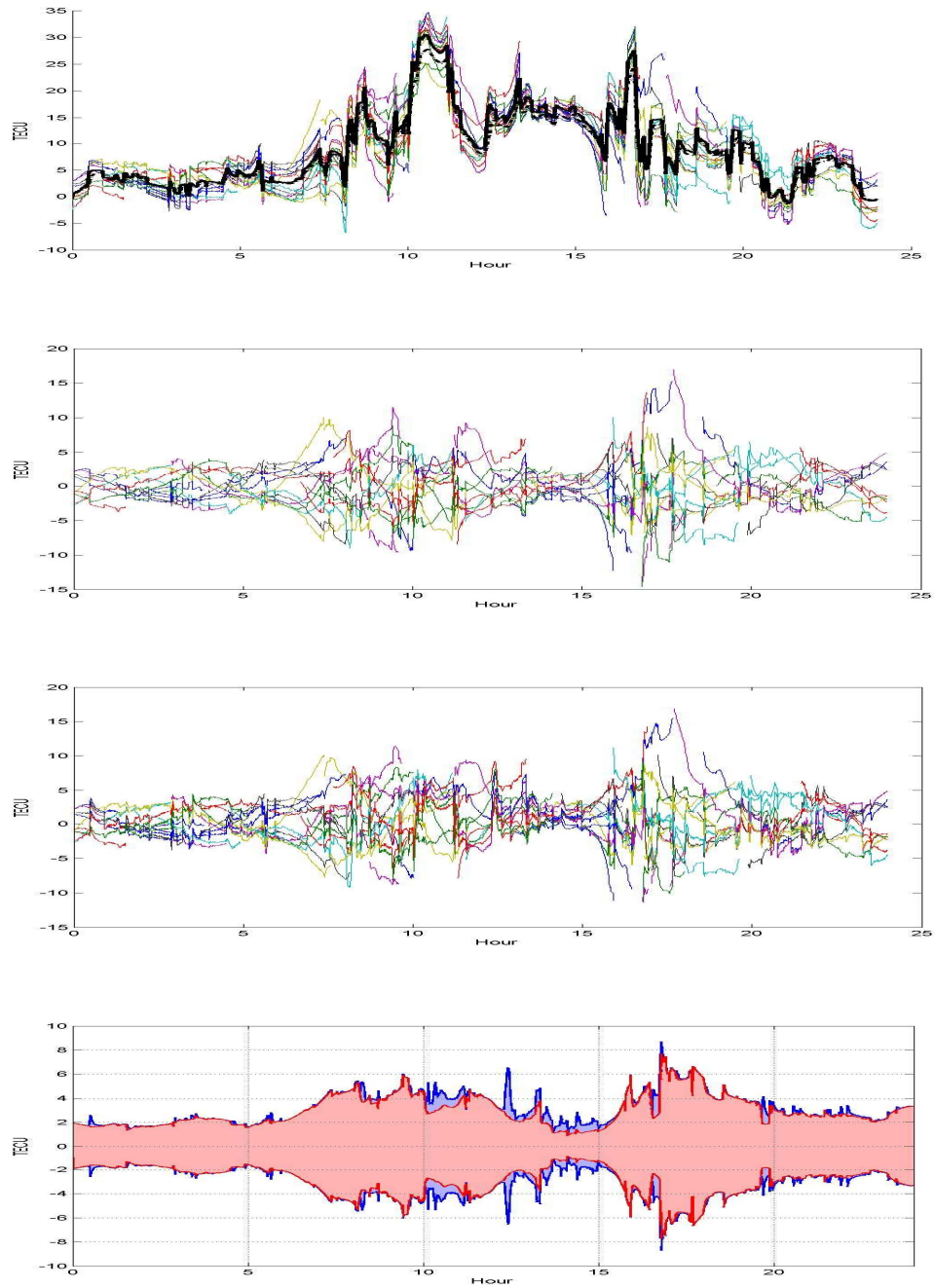


Figure 24 eijs station results. First panel illustrates observations and the performance of the filters for estimating VTEC. Different satellites observations color coded. Solid thick line is for particle filter and dashed thick line is for Kalman filter. The second and third panels show the post fit residuals of the Particle filter and the Kalman filters estimations, respectively. The fourth panel depicts the post fit standard deviation for each epoch in which the blue one is for the Kalman filter and the red one is for the particle.

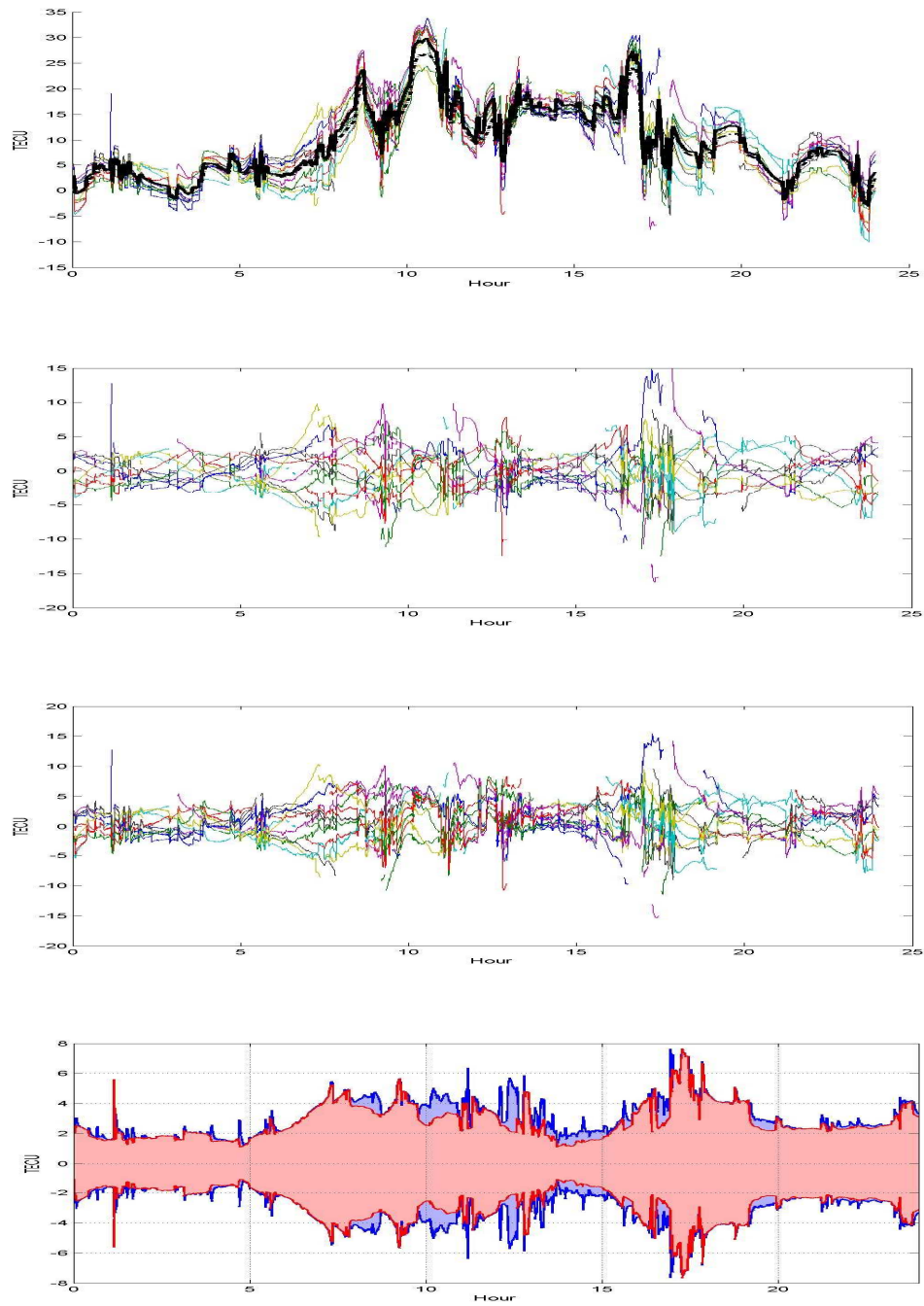


Figure 25 eusk station results. First panel illustrates observations and the performance of the filters for estimating VTEC. Different satellites observations color coded. Solid thick line is for particle filter and dashed thick line is for Kalman filter. The second and third panels show the post fit residuals of the Particle filter and the Kalman filters estimations, respectively. The fourth panel depicts the post fit standard deviation for each epoch in which the blue one is for the Kalman filter and the red one is for the particle.

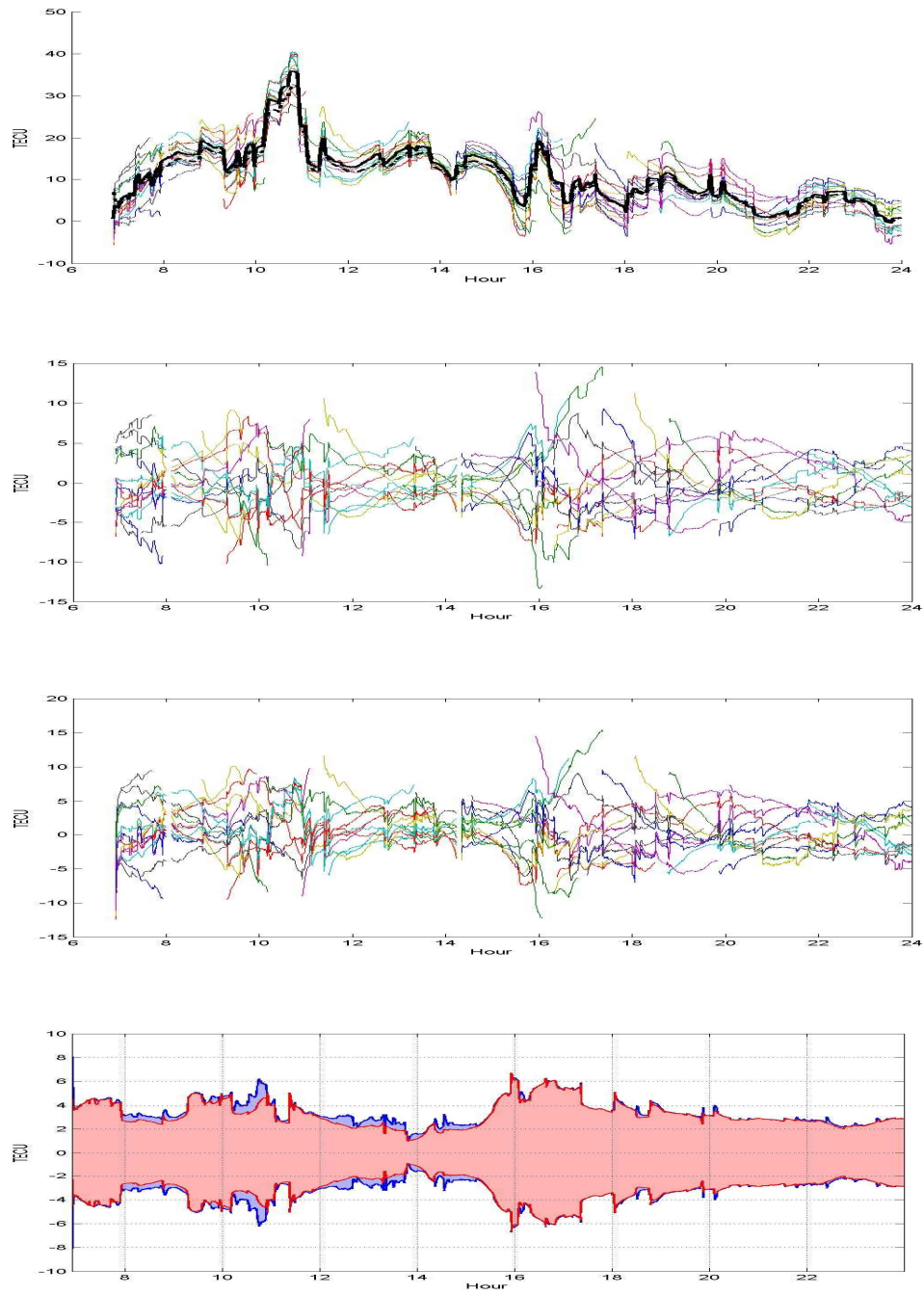


Figure 26 gwvl station results. First panel illustrates observations and the performance of the filters for estimating VTEC. Different satellites observations color coded. Solid thick line is for particle filter and dashed thick line is for Kalman filter. The second and third panels show the post fit residuals of the Particle filter and the Kalman filters estimations, respectively. The fourth panel depicts the post fit standard deviation for each epoch in which the blue one is for the Kalman filter and the red one is for the particle.

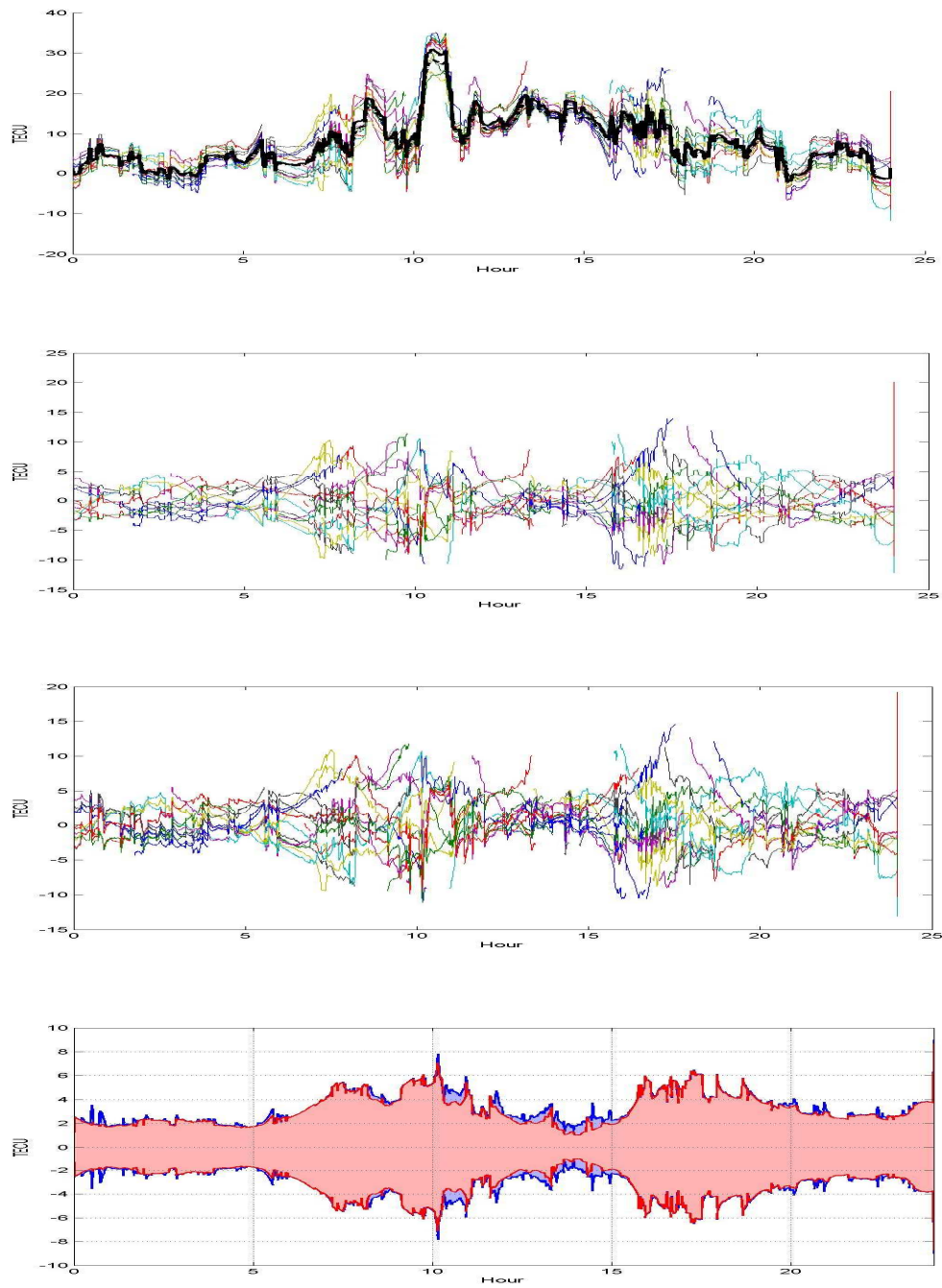


Figure 27 hobo station results. First panel illustrates observations and the performance of the filters for estimating VTEC. Different satellites observations color coded. Solid thick line is for particle filter and dashed thick line is for Kalman filter. The second and third panels show the post fit residuals of the Particle filter and the Kalman filters estimations, respectively. The fourth panel depicts the post fit standard deviation for each epoch in which the blue one is for the Kalman filter and the red one is for the particle.

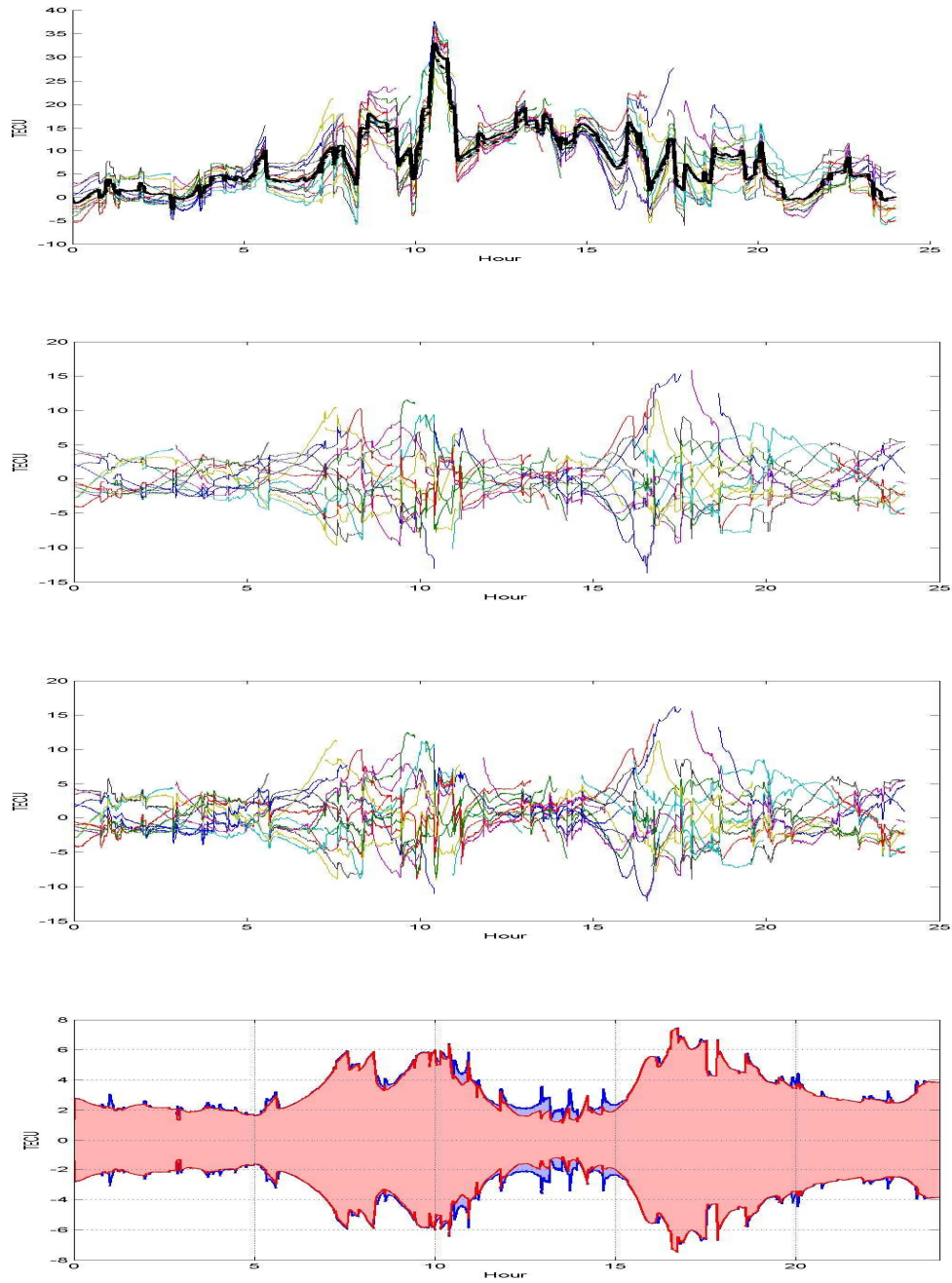


Figure 28 hoe2 station results. First panel illustrates observations and the performance of the filters for estimating VTEC. Different satellites observations color coded. Solid thick line is for particle filter and dashed thick line is for Kalman filter. The second and third panels show the post fit residuals of the Particle filter and the Kalman filters estimations, respectively. The fourth panel depicts the post fit standard deviation for each epoch in which the blue one is for the Kalman filter and the red one is for the particle.

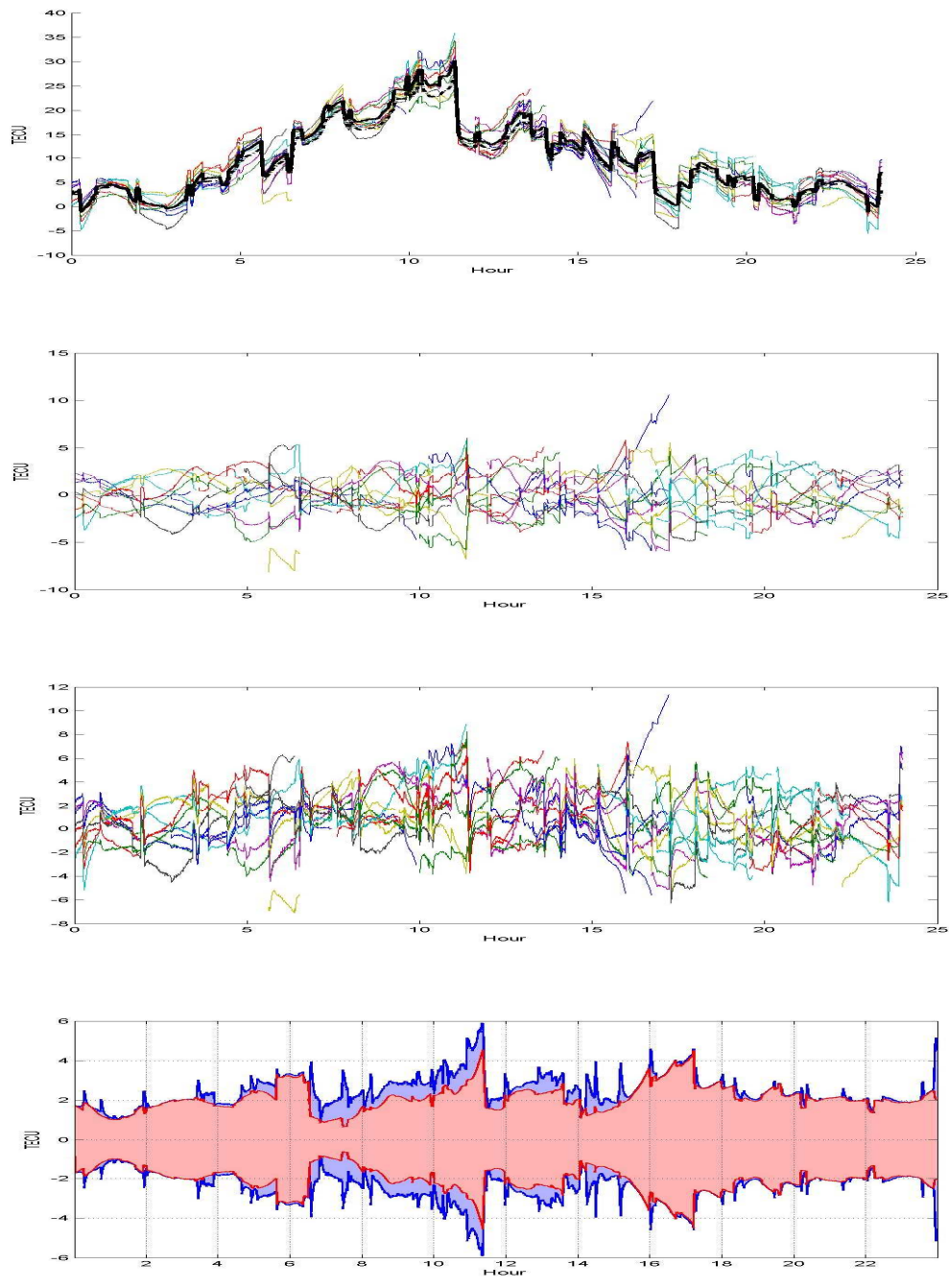


Figure 29 igeo station results. First panel illustrates observations and the performance of the filters for estimating VTEC. Different satellites observations color coded. Solid thick line is for particle filter and dashed thick line is for Kalman filter. The second and third panels show the post fit residuals of the Particle filter and the Kalman filters estimations, respectively. The fourth panel depicts the post fit standard deviation for each epoch in which the blue one is for the Kalman filter and the red one is for the particle.

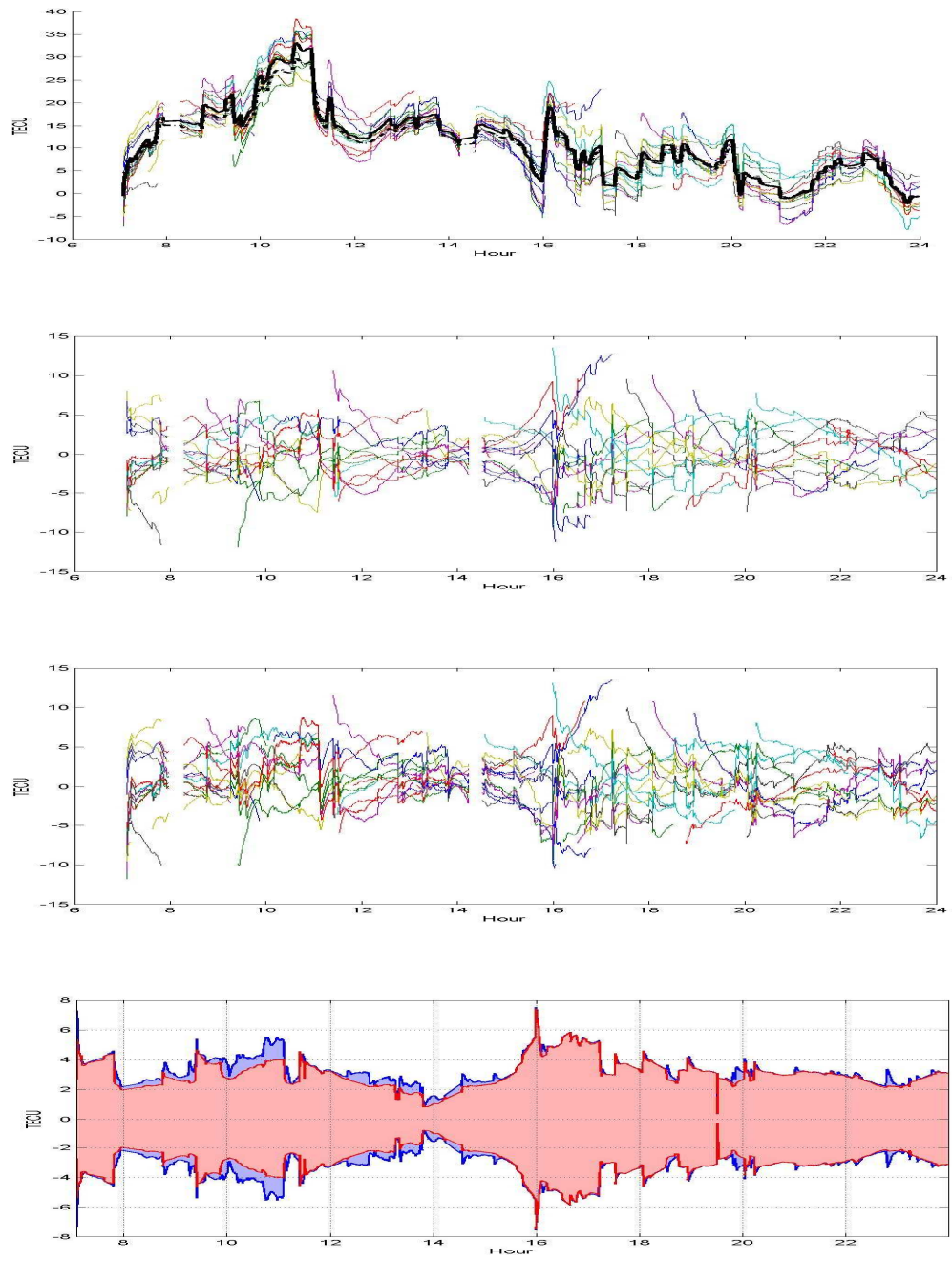


Figure 30 Iodiz station results. First panel illustrates observations and the performance of the filters for estimating VTEC. Different satellites observations color coded. Solid thick line is for particle filter and dashed thick line is for Kalman filter. The second and third panels show the post fit residuals of the Particle filter and the Kalman filters estimations, respectively. The fourth panel depicts the post fit standard deviation for each epoch in which the blue one is for the Kalman filter and the red one is for the particle.

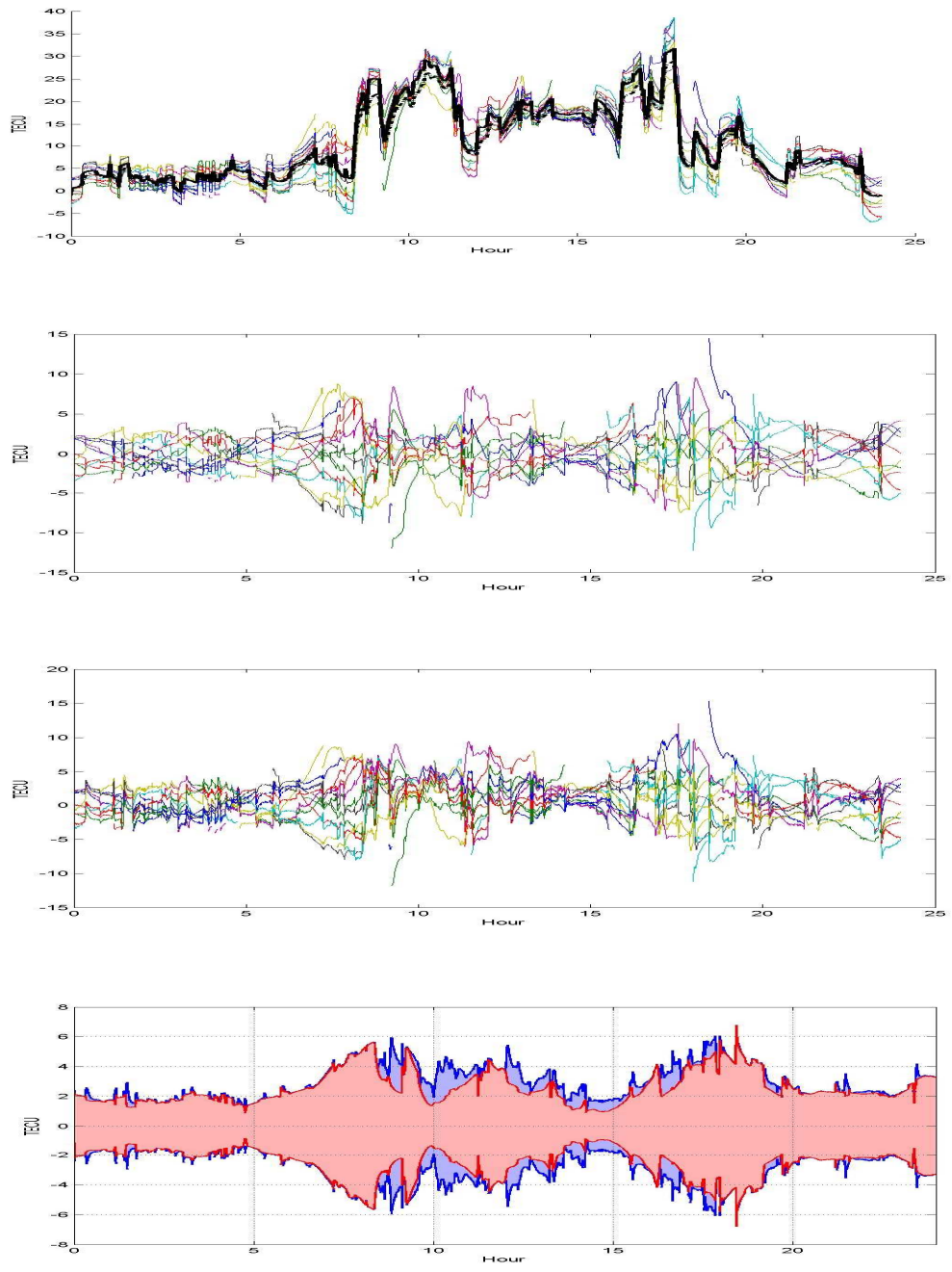


Figure 31 man2 station results. First panel illustrates observations and the performance of the filters for estimating VTEC. Different satellites observations color coded. Solid thick line is for particle filter and dashed thick line is for Kalman filter. The second and third panels show the post fit residuals of the Particle filter and the Kalman filters estimations, respectively. The fourth panel depicts the post fit standard deviation for each epoch in which the blue one is for the Kalman filter and the red one is for the particle.

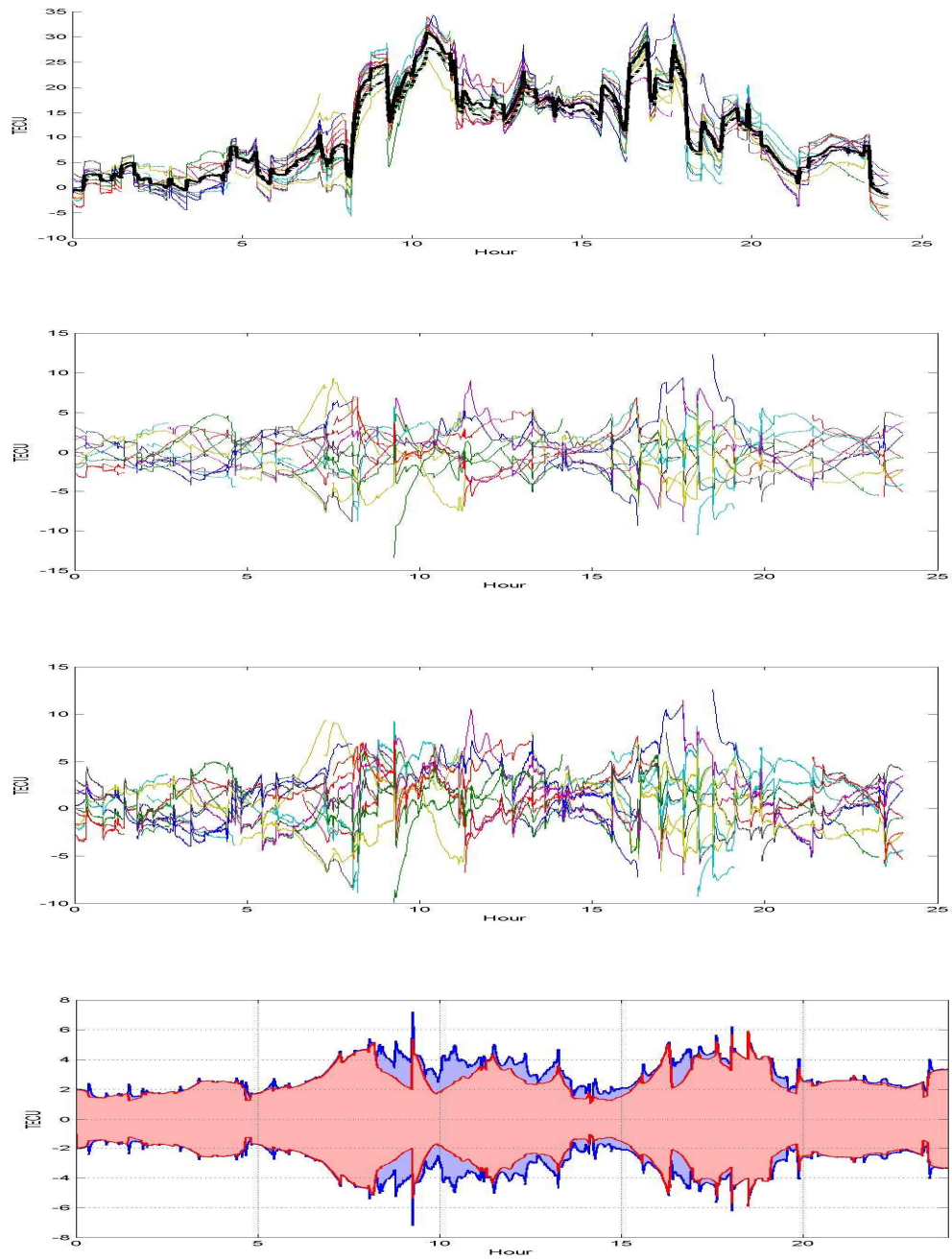


Figure 32 mlvl station results. First panel illustrates observations and the performance of the filters for estimating VTEC. Different satellites observations color coded. Solid thick line is for particle filter and dashed thick line is for Kalman filter. The second and third panels show the post fit residuals of the Particle filter and the Kalman filters estimations, respectively. The fourth panel depicts the post fit standard deviation for each epoch in which the blue one is for the Kalman filter and the red one is for the particle.

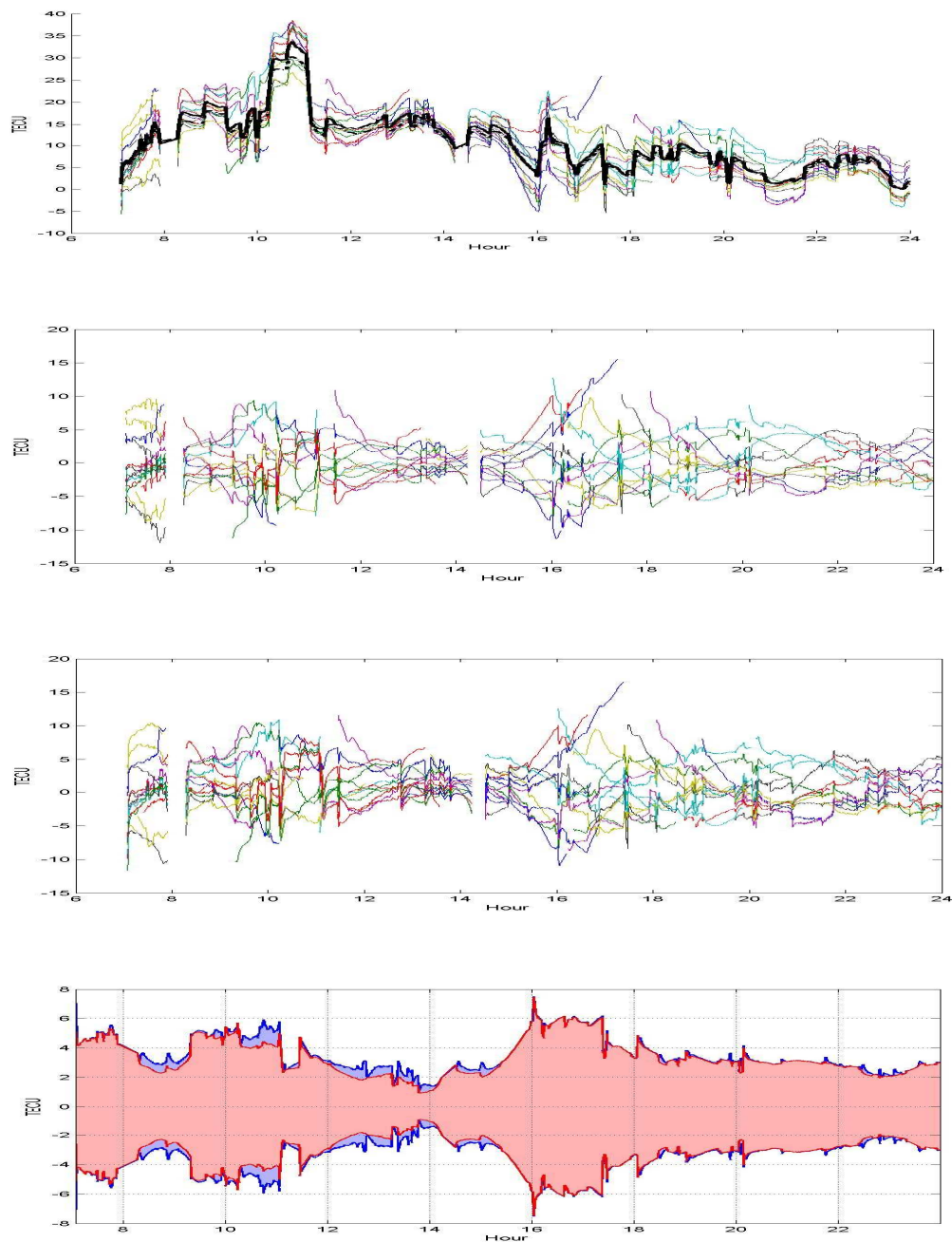


Figure 33 redz station results. First panel illustrates observations and the performance of the filters for estimating VTEC. Different satellites observations color coded. Solid thick line is for particle filter and dashed thick line is for Kalman filter. The second and third panels show the post fit residuals of the Particle filter and the Kalman filters estimations, respectively. The fourth panel depicts the post fit standard deviation for each epoch in which the blue one is for the Kalman filter and the red one is for the particle.

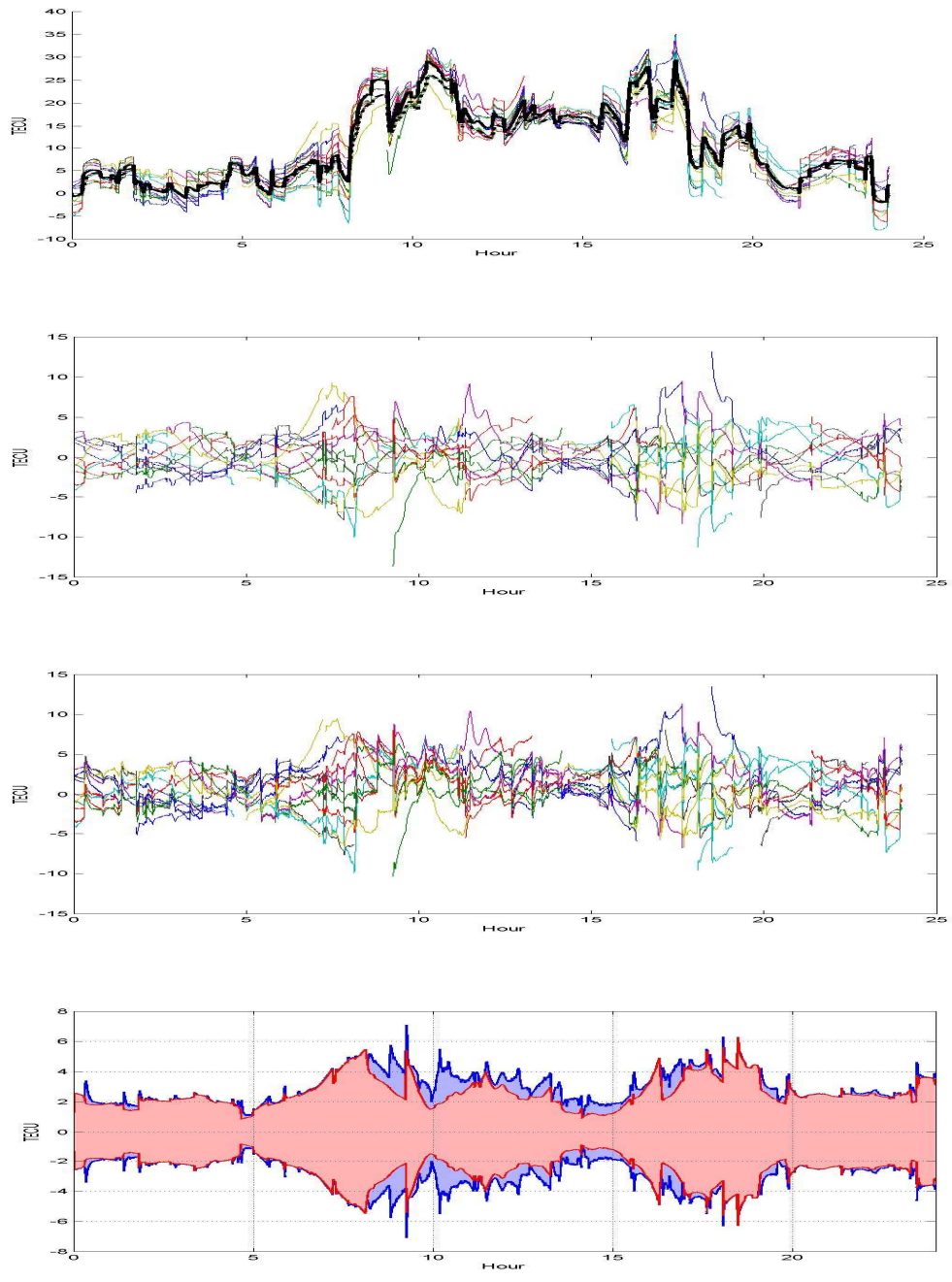


Figure 34 smne station results. First panel illustrates observations and the performance of the filters for estimating VTEC. Different satellites observations color coded. Solid thick line is for particle filter and dashed thick line is for Kalman filter. The second and third panels show the post fit residuals of the Particle filter and the Kalman filters estimations, respectively. The fourth panel depicts the post fit standard deviation for each epoch in which the blue one is for the Kalman filter and the red one is for the particle.

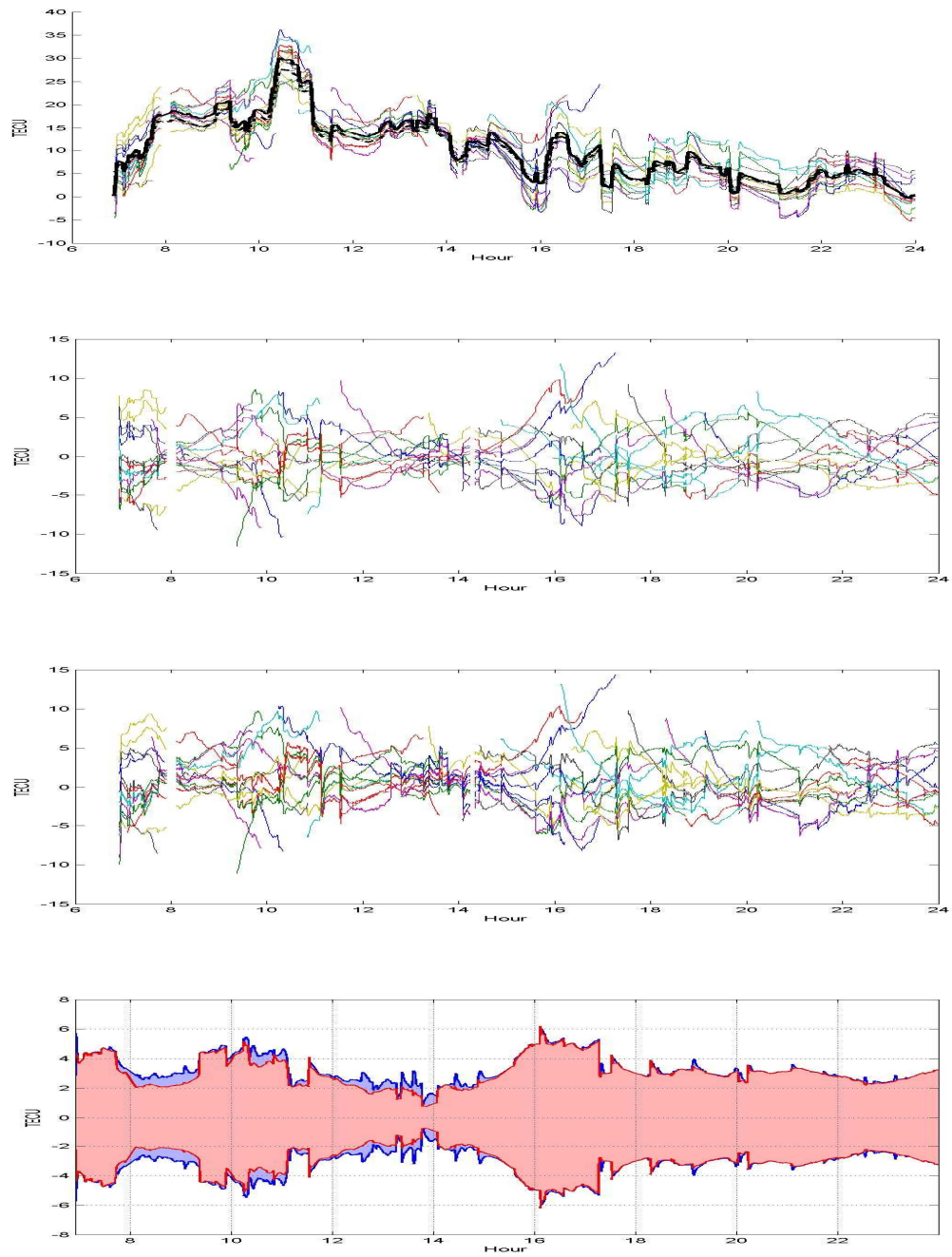


Figure 35 swki station results. First panel illustrates observations and the performance of the filters for estimating VTEC. Different satellites observations color coded. Solid thick line is for particle filter and dashed thick line is for Kalman filter. The second and third panels show the post fit residuals of the Particle filter and the Kalman filters estimations, respectively. The fourth panel depicts the post fit standard deviation for each epoch in which the blue one is for the Kalman filter and the red one is for the particle.

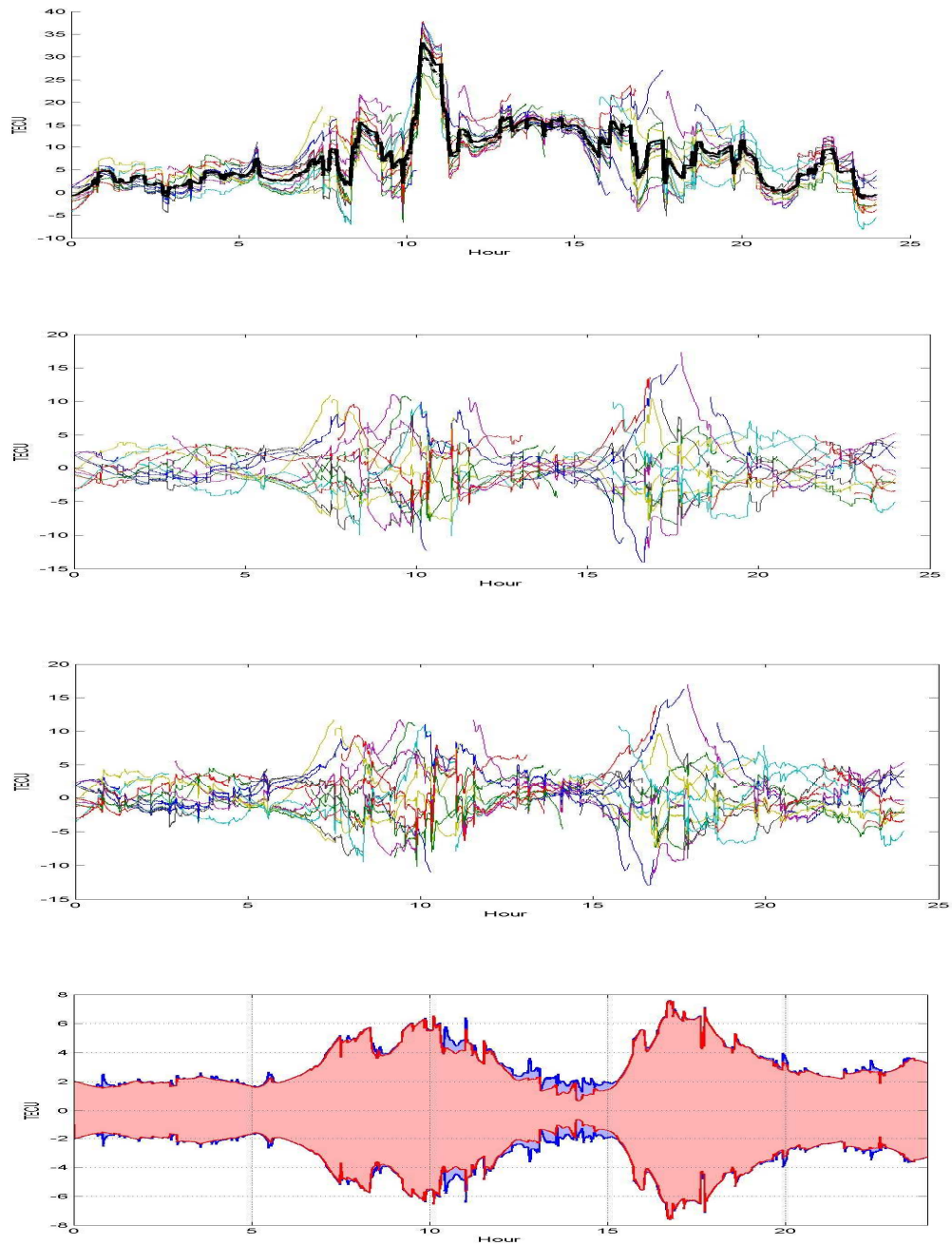


Figure 36 ters station results. First panel illustrates observations and the performance of the filters for estimating VTEC. Different satellites observations color coded. Solid thick line is for particle filter and dashed thick line is for Kalman filter. The second and third panels show the post fit residuals of the Particle filter and the Kalman filters estimations, respectively. The fourth panel depicts the post fit standard deviation for each epoch in which the blue one is for the Kalman filter and the red one is for the particle.

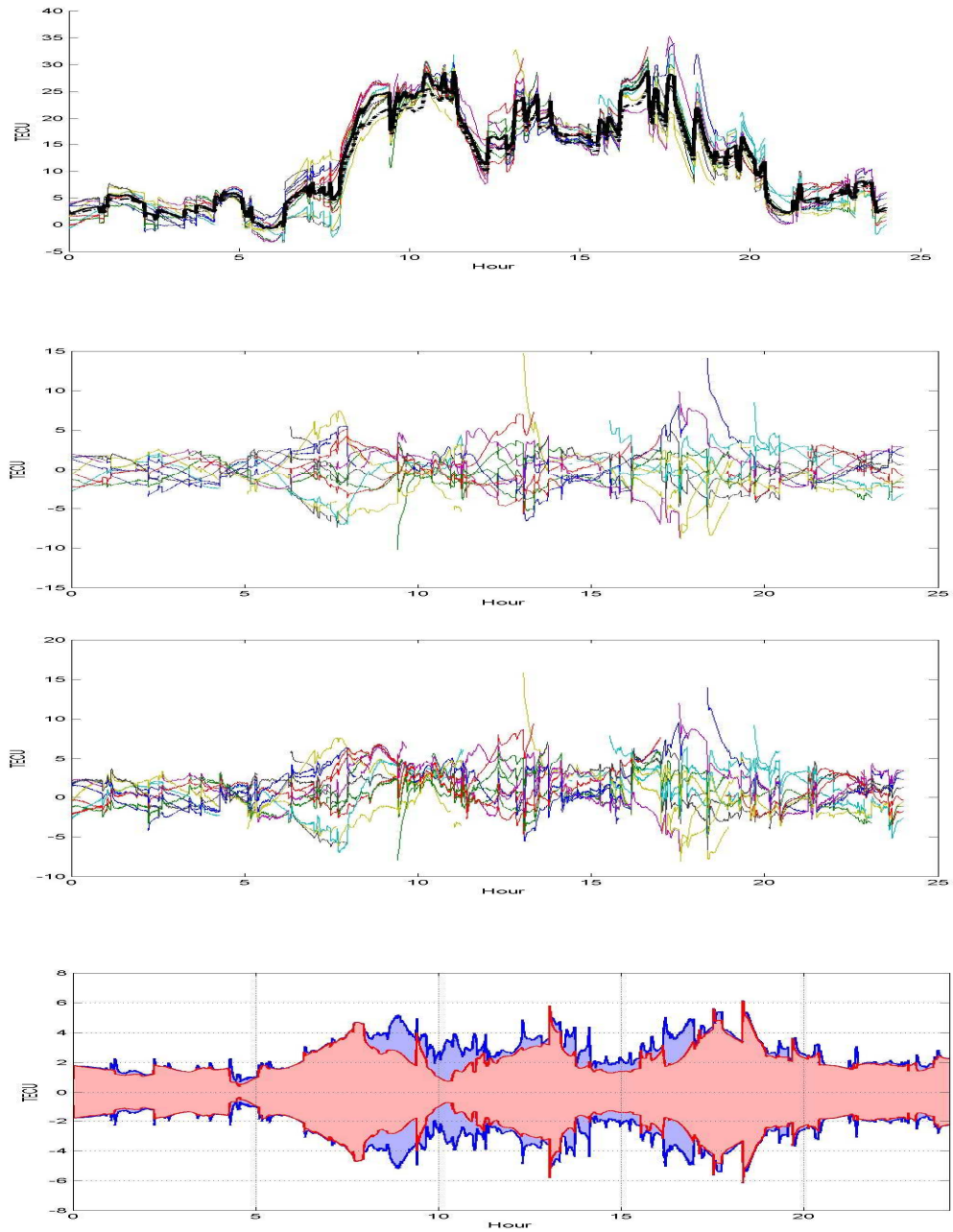


Figure 37 tlmf station results. First panel illustrates observations and the performance of the filters for estimating VTEC. Different satellites observations color coded. Solid thick line is for particle filter and dashed thick line is for Kalman filter. The second and third panels show the post fit residuals of the Particle filter and the Kalman filters estimations, respectively. The fourth panel depicts the post fit standard deviation for each epoch in which the blue one is for the Kalman filter and the red one is for the particle.

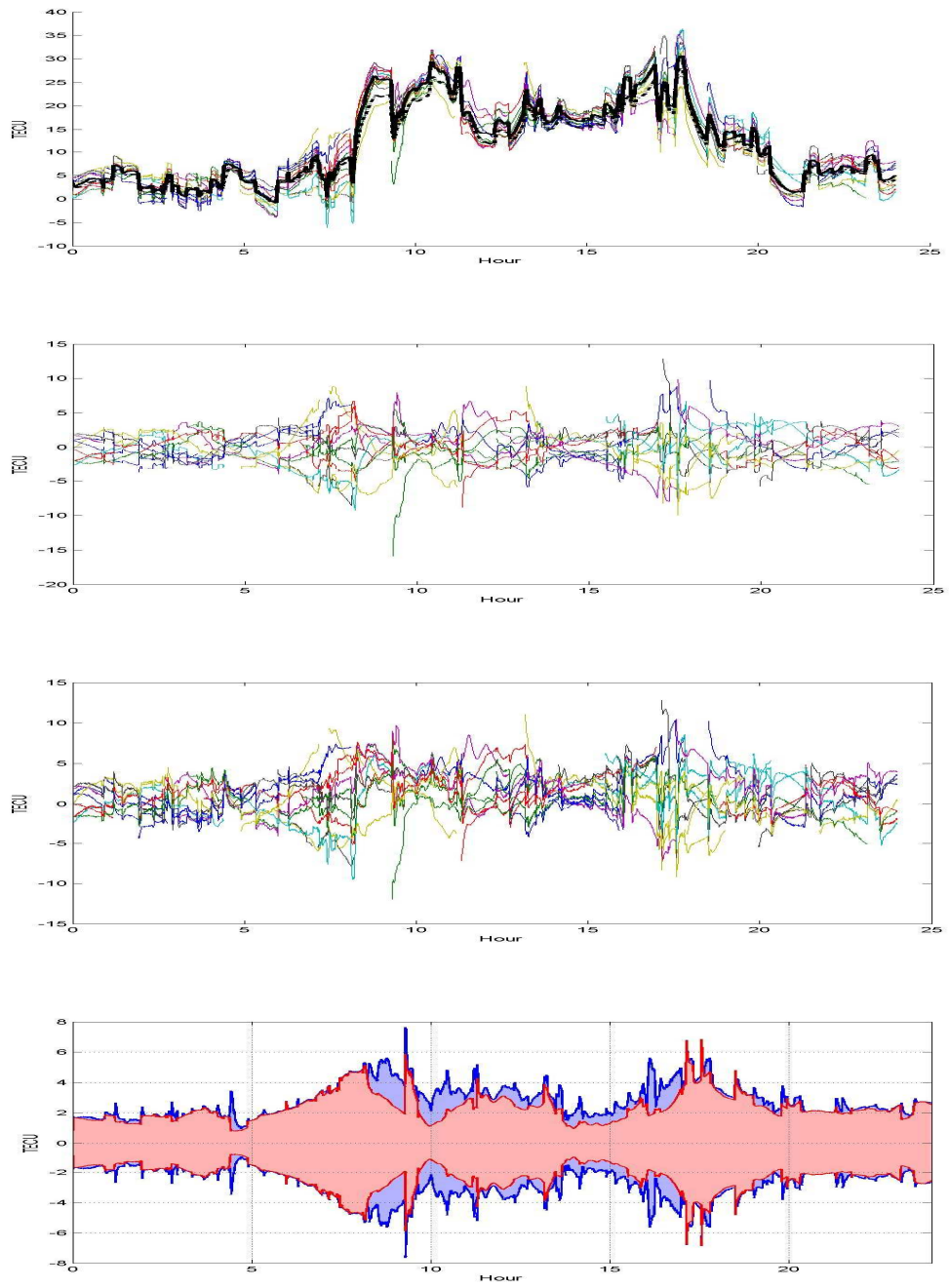


Figure 38 vfc station results. First panel illustrates observations and the performance of the filters for estimating VTEC. Different satellites observations color coded. Solid thick line is for particle filter and dashed thick line is for Kalman filter. The second and third panels show the post fit residuals of the Particle filter and the Kalman filters estimations, respectively. The fourth panel depicts the post fit standard deviation for each epoch in which the blue one is for the Kalman filter and the red one is for the particle.

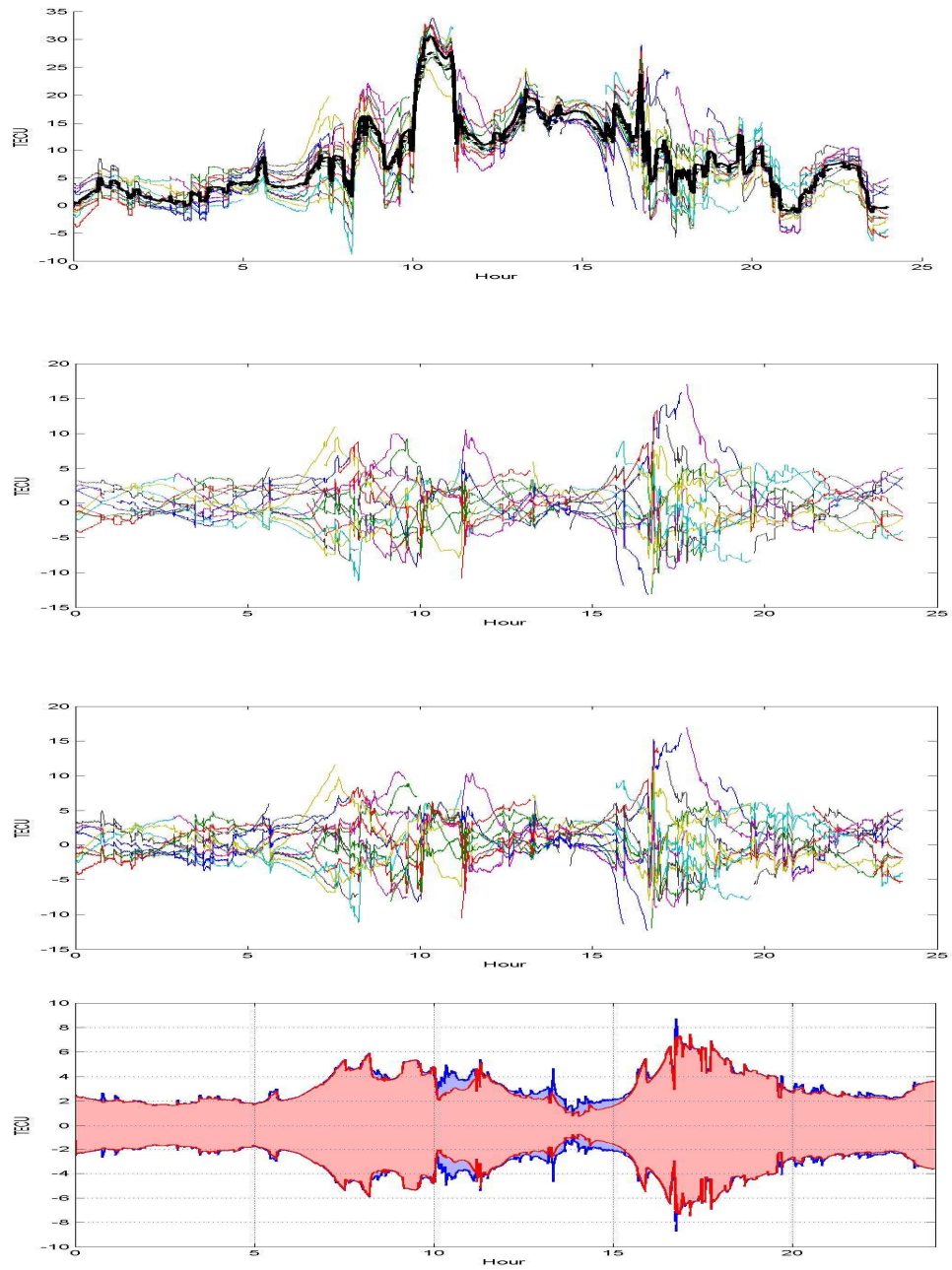


Figure 39 ware station results. First panel illustrates observations and the performance of the filters for estimating VTEC. Different satellites observations color coded. Solid thick line is for particle filter and dashed thick line is for Kalman filter. The second and third panels show the post fit residuals of the Particle filter and the Kalman filters estimations, respectively. The fourth panel depicts the post fit standard deviation for each epoch in which the blue one is for the Kalman filter and the red one is for the particle.

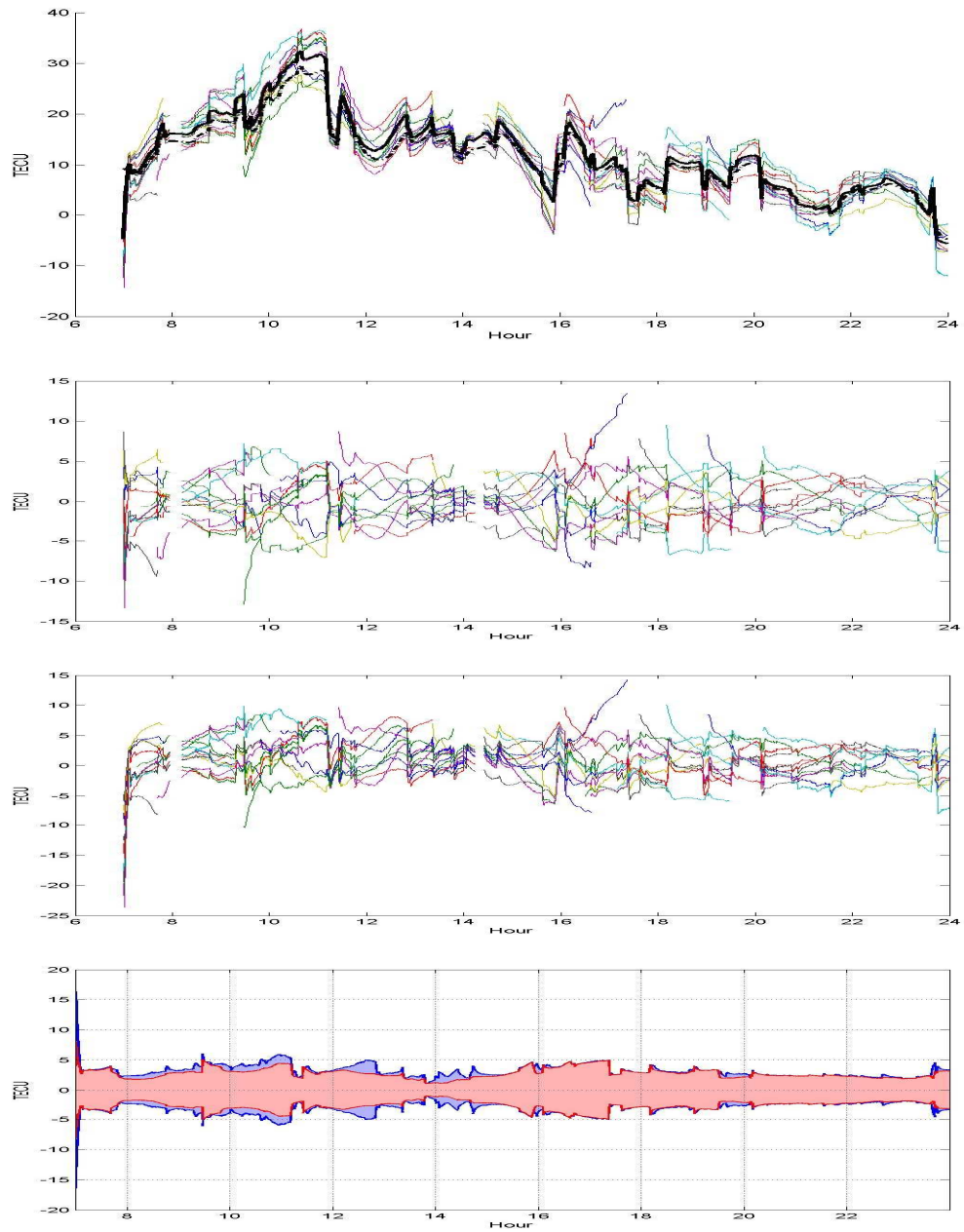


Figure 40 zywi station results. First panel illustrates observations and the performance of the filters for estimating VTEC. Different satellites observations color coded. Solid thick line is for particle filter and dashed thick line is for Kalman filter. The second and third panels show the post fit residuals of the Particle filter and the Kalman filters estimations, respectively. The fourth panel depicts the post fit standard deviation for each epoch in which the blue one is for the Kalman filter and the red one is for the particle.

CHAPTER 5

Conclusion and Future Work

5.1 Conclusion

The ionosphere modeling is a popular topic in the various fields of science and engineering because of its effect on the electromagnetic signals. The data needed for the ionosphere modeling can be obtained by several methods. Among these methods, providing information through GPS is the most preferable one due to its accuracy and widespread ground based stations. Dual frequency GPS receivers are used for extracting the ionospheric TEC information from GPS signals. This method is based on the dispersive characteristic of the ionosphere. In other word, Velocity of the electromagnetic signals depends on their frequency in dispersive mediums. There are many models for the ionosphere in the global, regional and local scales. However, the ionosphere is exposed to many irregularities because of, for example, geomagnetic storms during sun activities. Global and regional models may not be sufficient enough in temporal scale for monitoring such irregularities.

In this study, particle filter, which had not been applied to the local modeling of the ionosphere in the literature until now, was performed for real sets of data. Some parts of which are affected by geomagnetic storm. The data has been gathered from 29 GPS CORS stations located in Europe. Among various kinds of Particle filter, Regularized Particle filter has been preferred in this study to prevent sample impoverishment problem. Before beginning with application of filters preprocessing

step was performed to the data. In a brief description, cycle slip detection, calculating geometry free linear combination of pseudorange data, and leveling pseudorange measurements with carrier phase observations are included in preprocessing step.

Beside the VTEC, the receiver bias was also estimated within the algorithms. For comparison also, standard Kalman filter has been used. In both filters, the first order Gauss Markov process was taken for the dynamic part of the system. For evaluation of the results the post-fit residual for each satellite data in each epoch was computed. Also the Root Mean Square Error (RMSE) was calculated for all stations in order to make the overall comparison of the filters possible.

The results clearly show that the Particle filter provides better results in terms of RMSE in all stations though in few of them the difference is not very tangible. It can be originated from the various effect of magnetic storm in different stations. This can be easily figured out by comparing the post fit residuals standard deviations in each epoch provided in the chapter 4. During the hours that the storm has maximum effect, between 9:00 and 16:00, the efficiency of the particle filter is evident. While in the time of quiet condition both of the filters produce almost the same results. This can be better seen in the stations that VTEC variation is more complex such as the “crei” station or the “ctab” station. Also, the RMSE of the Particle filter and the Kalman filter shown in Table 5 imply the better performance of the Particle filter.

5.2 Future Work

The following items are the potential subjects for local ionospheric VTEC modeling:

- Expand the current codes to become a software with a user interface
- Using other types of Kalman filters for the comparison of this modeling

- Transforming the current codes to C++ or Java programming language for faster computation
- Developing the Particle filter for the near real time ionosphere modeling by expanding the space state model.

REFERENCES

Anghel, A., Astilean, A., Letia, T., & Komjathy, A. (2008). Near real-time monitoring of the ionosphere using dual frequency GPS data in a Kalman filter approach. *IEEE International Conference on Automation, Quality and Testing, Robotics*, (s. 54-58). Cluj-Napoca.

Anghel, A., Carrano, C., Komjathy, A., Astilean, A., & Letia, T. (2009). kalman filter-based algorithms for monitoring the ionosphere and plasmasphere with GPS in near real time. *Journal of Atmospheric and Solar-Terrestrial Physics* , 158-174.

Arikan, F., Arikan, O., & Erol, C. B. (2007). Regularized estimation of TEC from GPS data for certain midlatitude stations and comparison with the IRI model. *Advances in Space Research* , 867–874.

Bilitza, D. (2001). International Reference Ionosphere 2000. *Radio Science* , 36, 261-275.

Brunini, C., Meza, A., Azpilicueta, F., Van Zele, M., Gende, M., & Diaz, A. (2004). A New Ionosphere Monitoring Technology Based on GPS. *Astrophysics and Space Science* , 290, 415-429.

Ciraolo, L., Azpilicueta, F., Brunini, C., Meza, A., & radicella, S. (2007). Calibration Errors on experimental Slant Total Electron Content (TEC) Deteremined with GPS. *Journal of Geodesy* , 81 (2), 111-120.

Datch, R., Hugentobler, U., Fridez, P., & Meindle, M. (2007). *Brenese GPS Software Version 5.0*. Astronomical Institute, University of Bern.

Doherty, P., Decker, D., Sultan, P., Rich, F., & Borer, W. (1999). Validation of Prism:the Climatology. *Proceeding of Ionospheric Effects Symposium* (s. 330-339). Springfield.

El Gizawy, M. (2003). *Development of Ionosphere Monitoring Technique Using GPS Measurements for High Latitude GPS Users*. Thesis Dissertation, University of Calgary, Department of Geomatics Engineering.

Garcia Fenrnandez, M. (2004). *Contribution to the 3D ionospheric sounding with GPS data*. Ph.D. Thesis, Technical University of Catalonia, Spain .

Groves, P. D. (2008). *Principal of GNSS,Intertial, and Multisensor Integrated Navigation Systems*. Artech House.

Gwal, A., & Jain, A. (2011). GPS scinitillation studies in the arctic region during the first winter-phase 2008 Indian Arctic Expedition. *Polar Science* , 4, 574-587.

Hernández-Pajares, M., Hernández-Pajares, J. M., Sans, J., Orus, R., A., G.-R., J., G.-R., et al. (2009). The IGS VTEC maps: a reliable source of ionospheric information since 1998. *Journal of Godesy* , 83, 263–275.

Hofmann-Wellenhof, B., Lichtenegger, H., & Wasle, E. (2008). *GNSS - Global Navigation Satellite Systems - GPS, GLONASS, Galileo & more*. Springer.

Kane, R. (2011). Solar Flare of 15 February 2011 and its Geomagnetic Effects. *Indian Journal of Radio and Space Physics* , 40, 253-256.

Karslioglu, M. O., & Durmaz, M. (2012). Regional spatio-temporal modeling of the ionospheric Vertical Total Electron Content (VTEC) using Multivariate Adaptive Regression B-Splines (BMARS). *Journal of Geodesy and Geoinformation* , 9-16.

- Kasha, M. A. (1969). *The Ionosphere and its Interaction with Satellites*. Gordon and Breach.
- Koch, K.-R. (1997). *Parameter Estimation and Hypothesis Testing in Linear Models*. Springer.
- Komjathy, A. (1997). *Global Ionospheric Total Electron Content Mapping Using Global Positioning System*. New Brunswick: Department of Geodesy and Geomatics Engineering.
- Komjathy, A., B., L. R., & Bilitza, D. (1998). Ingesting GPS-Derived TEC Data into the International Reference Ionosphere for Single Frequency Radar Altimeter Ionospheric Delay Corrections. *Advances in Space Research* , Vol 22. 793–801.
- Kunches, J., & Klobuchar, J. (2001). Eye on the Ionosphere:GPS after SA. *GPS Solutions* , 4, 52.
- Langerly. (1998). *GPS Receivers and the Observables & Propagation of GPS Signals*. *GPS for Geodesy*. Springer.
- Langery, R. B. (2000). GPS, the Ionosphere, and the Solar Maximum. *GPS world* , 44-49.
- Lee, D.-J. (2005). *Nonlinear Bayesian Filtering with Applications to Estimation and Navigation*. Texas A&M University, Graduate Studies.
- Liu, J., & Kuga, Y. (2003). Ionospheric Effects on SAR Imaging: A Numerical Study. *IEEE Transactions on Geoscience and Remote Sensing* , 41, 939-947.
- Liu, Z., & Gao, Y. (2004). Ionospheric TEC predictions over a local area GPS reference network. *GPS Solutions* , 23-29.

Mohinder, S., Lawrence, R., & Angus, P. (2007). *Global Positioning System, Inertial Navigation and Integration*. John Wiley & Song.

Nohutcu, M. (2009). *Development of a MATLAB Based Software Package for Ionosphere Modeling*. Ph.D Thesis, Middle East Technical University, Civil Engineering Department.

Nohutcu, M., Karslioglu, M. O., & Schmidt, M. (2010). B-Spline modeling of VTEC over Turkey using GPS observations. *Journal of Atmospheric and Solar-terrestrial Physics* , 617-624.

Pulinets, S., & Boyarchuk, K. (2004). *Ionospheric Precursors of Earthquake*. Springer.

Ray, J. (2000). *mitigation of GPS code and Carrier Phase Effects using a Multi-Antenna System*. Ph.D Disertation, University of Calgary , Department of Geomatics Engineering.

Rishbeth, H., & Garriot, O. (1969). *introduction to ionospheric physics*. New York: Academic Press.

Ristic, B., Arulampalam, S., & Gordon, N. (2004). *Beyond the Kalman Filter; Particle Filter for Tracking Applications*. DSTO.

Schaer, S. (1999). *Mapping and Predicting the Earth's Ionosphere Using Global positioning System*. University of Berne, Astronomical Institute.

Schaer, S., Beutler, G., & Rothacher, M. (1996). Daily global ionosphere maps based on GPS carrier phase data routinely produced by the CODE Analysis Center. *Proceedings of the IGS* .

Seeber, G. (2003). *Satellite Geodesy*. Walter de Gruyter.

Spilker, J. (1996). Tropospheric Effects on GPS. B. Parkinson, & J. Spilker içinde, *Global positioning Systems: Theory and applications*. American Institute of Aeronautics and Astronautics.